Ice-Pavement Bond Prevention: Fundamental Study

Lynn S. Penn
Allan Meyerson

Chemical Engineering Department
Polytechnic University
Brooklyn, NY

Acknowledgments

Contents

List of Figures

List of Tables

Abstract

This report states the findings of an investigation of the freezing of water on portland
cement concrete and asphalt concrete pavements. Surface analysis and mechanical
testing techniques were used, as well as computer simulation of the crystallization
process. Models and reference substrates were used in addition of actual pavements in
order to isolate and control experimental variables. The ice-pavement system was
studied as an adhesive joint in order to address the factors important to determining the
ice adhesive strength. The research succeeded in identifying approaches for weakening
or preventing the ice-pavement bond.

Executive Summary

The freezing of water on pavement was investigated for the purpose of determining how to prevent the formation of a strong ice-pavement bond. The pavements studied were portland cement concrete and asphalt concrete. Simpler materials were used as model and reference substrates when necessary. The investigation employed surface analysis of substrates, mechanical testing of ice-substrate joints, and computer simulation of the crystallization process under different conditions.

It was found that several fundamental features of both the pavement and the ice lead to excellent bonding between the two, with the result that bond prevention is difficult. Both the small scale roughness and inherent high surface energy of the pavement both enhance strength. Water, whose low viscosity allows good contact, has a relatively large energy of interaction with pavement, leading to formation of a good bond. Furthermore, the pavement nucleates small, bubble-free ice crystals that are strong and difficult to remove mechanically.

In spite of these discouraging features, several avenues for ice-pavement bond prevention or strength reduction were identified. One of these was use of low-energy pavement coating materials to minimize ice-substrate intermolecular interactions and reduce the energy required to separate the ice from the pavement. Another was use of materials of poor thermal conductivity to promote internal stress buildup in and around the ice-substrate joint and cause interfacial separation at a lower value of externally applied load. The third was the use of nucleation-preventing chemicals to prevent the formation of the strong layer of small crystals directly on the pavement surface.

1

Introduction

The consequences of icing of pavement are serious and varied. They include safety risks to humans, impeded vehicular motion, and the deterioration of highways and bridges. The search for better methods of combatting pavement icing has been strictly empirical up to now, and has dwelt mainly on ice removal after it has formed on the pavement. Unfortunately, progress in the control of icing has been held back by lack of a fundamental understanding of the ice-pavement bond.

The objective of our research program was to develop promising ways to prevent or impair bond formation between ice and pavement. This involved identifying the fundamental physical and chemical factors that make important contributions to ice-pavement adhesion, and determining to what extent these factors could be manipulated to prevent or weaken the adhesion.
We felt that the most effective approach was to regard the ice-pavement system as an adhesive joint, and to study it accordingly. This approach covers aspects of the ice-pavement bond at many levels, from the molecular details at the ice-substrate interface, through the microscopic surface topography and crystallization, to the macroscopic joint strength and fracture energy. All levels are important to understanding the practical adhesion between ice and pavement.

To identify the key factors that control the adhesive strength, we needed to be able to isolate and measure key variables. When the complexity of real pavement materials made either the isolation, control, or unobstructed observation of these variables impossible, simpler materials were used as models. Depending on the situation, the appropriate model material would serve to mimic a particular chemical or physical property of pavement, or it would allow better observation and control of a process. In addition, some well-characterized reference materials were used in order to understand where pavement fell relative to other substances in the materials spectrum. Thus, in our work, liberal use was made materials other than actual pavement.

Background

Every adhesive joint problem contains some fundamental ideas that serve as a common basis for discussion. Some of these fundamentals are summarized briefly below.

Molecular Adhesion

The forces of attraction on the atomic and molecular level between two materials

establish the adhesion at the interface. Molecular adhesion refers to the process of bringing two surfaces together in a thermodynamically reversible fashion where the only energy change involved is that due to nonchemically bonded inermolecular interactions.

The interactions between atoms and molecules result in a net attraction and thereby account for the existence of condensed phases. Several specific types are listed below.

1."London" or "dispersion", a nonpolar interaction arising from electron distribution effects around the atomic nuclei in each molecule,

2.Dipole-dipole,

3.Ion-induced dipole,

4.Dipole-induced dipole,

5.Hydrogen bonding, and

6.Acid-base.

These interactions are electrostatic in origin, the first being best explained in terms of quantum mechanics, while the remaining five can be adequately explained classically (1,2). All molecules experience the dispersion interaction with each other. Depending on the chemical structure, the other interactions may contribute to the attraction between molecules (3). For example, the strong attraction of ice molecules for each other is due not only to the dispersion interaction, but also to the large number of dipole-dipole and hydrogen bonding interactions per unit volume.

Other Bonding Mechanisms

Another mechanism is chemical bond formation across the interface. Since a chemical bond requires a great deal of energy to rupture, it has the potential to be very important. However, chemical bonding between a solidifying adhesive and the substrate to which it adheres is rare and can only be made to occur under special circumstances.

On the other hand, a commonly occuring mechanism is the lock and key interaction formed when an adhesive conforms to the topographical details of a solid substrate's surface. This mechanism, strictly mechanical, is the primary means by which a dental amalgam adheres to the tooth.

Adhesive Joint Strength

At the macroscopic level, the quantity of practical concern to those who wish to separate two materials from each other is adhesive joint strength. Unfortunately, joint strength has no consistent definition, independent of geometry, that yields a single numerical value for a given pair of adhering materials.

One of the most common definitions of joint strength is simply the applied load at failure divided by the cross-sectional area of the joint. This definition does not take into account such things as crack path (i.e., along the interface or through only one of the two adhering materials) or true area of the crack face (i.e., equal to a smooth plane or much larger due to severe rugosity). Thus a simple number for joint strength can be misleading unless a great deal is known about details of the failure.

Adhesive Joint Geometry

In actuality, the geometry of the adhesive joint greatly affects measured joint strength. In any adhesive joint, load that is applied uniformly and in a single mode (normal or shear) at the extreme ends of the joint is likely to be converted to a stress that is non-uniformly distributed and bimodal by the time it reaches the interface. The severity of these changes is related to the elastic modulus values of the two adhering phases. Not surprisingly, interfaces subjected to nonuniform stresses and mixed mode loading behave differently than uniformly stressed and simply loaded joints.

For the most part, until recently, adhesive joint performance has been evaluated on specimens chosen for their ease of preparation: specimens that yielded unknown stress distributions and unknown loading mode mixities at the interface. Obviously, data taken on specimens that differ in geometry cannot be compared with any validity. In addition, because of the interplay between joint geometry and material moduli, comparison of joint strength data from one substrate to another is of dubious value.

Traditional adhesive joint strength tests (e.g., butt tensile, lap shear) continue to be used, but more conservatively. Mindful of their drawbacks, experimenters now tend to restrict them to studies of a single adhesive-substrate system using a single specimen size and geometry. With these restrictions, these tests can give valid assessments of the effects of different substrate surface treatments, test rates, and test temperatures on joint strength.

Interfacial Fracture Energy

Fortunately, recent advances in the analysis of various adhesive joint designs have clarified the effects of joint geometry and material elastic moduli on experimental quantities such as failure load. This has led to increased use of interfacial fracture energy as the desired quantity for characterization of the interface. Interfacial fracture energy, which can be computed from quantities measured in an adhesive joint test, is attractive because it is believed to be a materials parameter. As such, it is independent of geometry, and should reflect the inherent character of a given interface. Thus, in any study of interfaces a major goal should be determination of interface fracture energy values.

Organization of the Report

The research work is described in this report as independent tasks, each pertaining to a different aspect of ice adhesion. The tasks are described and discussed in an order that the authors felt gives the reader an appreciation of the interrelation among the aspects of the ice-pavement bond at various levels.

The presentation of each separate task includes its purpose, a brief description of experimental method, the results, and the significance of the results. Overall conclusions and recommendations are presented at the end.

2

Literature Review

A review of the literature on ice adhesion, ice, and adhesion was conducted. Considering the large body of literature describing research on ice itself (sea ice, glacial ice, and freshwater ice) in the past 40 years, the number of articles addressing ice adhesion was surprisingly small. Of these, only a few articles described studies that used well-characterized substrates under a wide range of conditions. Most studies were narrowly focused on only a few substrates, or over a narrow range of temperatures, etc. Because these studies involved different test geometries, as well as different test conditions, comparison of their data to draw conclusions of any generality was not possible.

None of the studies contained values for interfacial fracture energy, the materials parameter truly diagnostic of adhesive performance. In the majority of the studies, the joint failure was cohesive within the ice, rather than at the ice-substrate interface. (Astoundingly, several studies failed to report whether the crack path was at the interface or through the ice itself and therefore had to be regarded as useless.) Cohesive failure of the ice in an ice-substrate joint provides no insight into the ice-substrate bond itself. The main way in which the body of literature was helpful to us was in pointing out technical difficulties associated with specimen preparation and testing of ice and ice joints.

A summary of our literature review is contained in a bibliography that is available from SHRP on request. Bibliographic entries are in a format provided by Pro-Cite™ (Personal Bibliographic Software, Inc., Ann Arbor, Michigan). Each entry also includes mention of the main points of the article and, in some cases, comments on its technical reliability or usefulness.

3

Computer Simulation

Computer simulations are useful in two ways. First, they are excellent tools for the evaluation of the relative importance of different parameters in complex situations. This aids in the effective design of experimental studies. Second, they can test these variables over smaller increments or wider ranges of values than is experimentally accessible. This extends the data base beyond that available in the laboratory and gives predictive value to the simulation.

Our goal was to develop a realistic three dimensional computer model of ice freezing on an irregular surface (pavement), a model that would permit examination of important variables over a wide range of conditions and determine their relative importance and effects. When viewed on a microscopic scale the freezing of ice on pavement surface can be treated mathematically as a moving boundary problem involving interfacial rate processes, heat transfer in two solid phases (ice and pavement) and one liquid phase. The complexity is increased because of the irregular nature of the pavement surface on a microscopic scale. In a situation of this type, when exact analytic solutions to a mathematical model are not possible, a computer simulation is a powerful technique that can provide useful information over a wide range of conditions, as well as guidance for the experimental portion of the work. A computer model, developed previously by Myerson to model solidification in both pure and binary compounds (6-8), was modified for use in this study.

Explanation of Simulation

The simulation considers variations in time and in three spatial dimensions. It consists of a main program and three subroutines: freezing, heat transfer, and melting. The essential structure of the program is given in Figure 3-1. Each phenomenon is treated in turn for a finite time interval. Freezing occurs first, followed by heat transfer, and melting. The main program is used to input necessary physical property data, and to determine the initial and boundary conditions of temperature and surface geometry. In addition, it is necessary to define the scale of the simulation by defining the distance between grid points in the three-dimensional array used to represent the material volume under study.

The freezing subroutine allows liquid to freeze for a finite time interval. Each site is examined, and the driving force for freezing at each is calculated from a relation of the form,

$$V = a(T_E - T)^n,$$
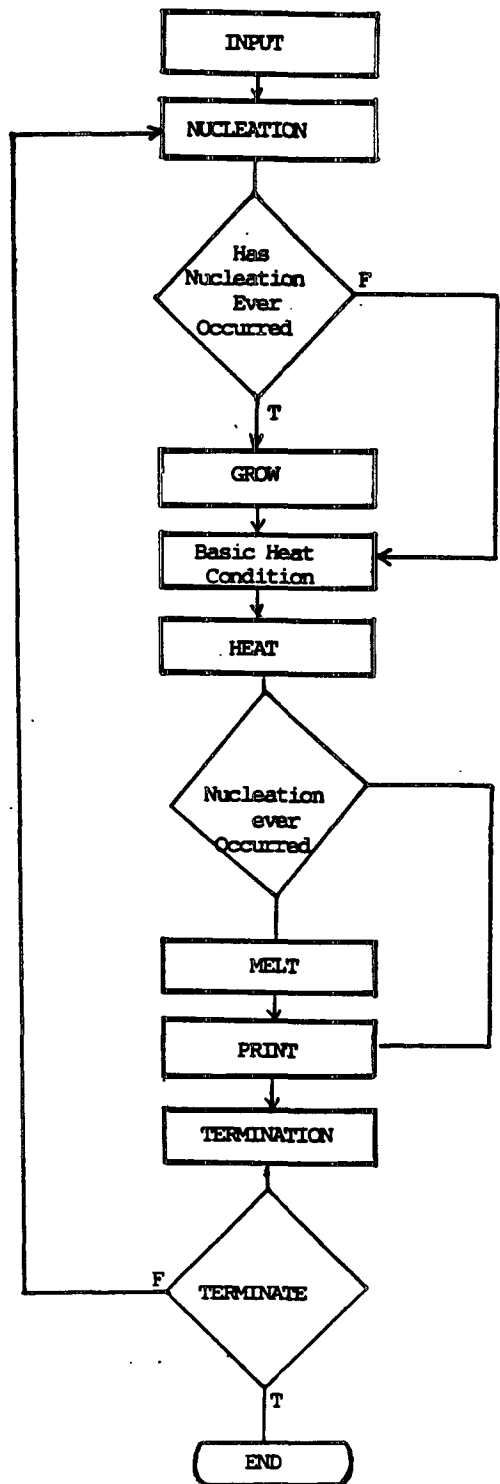
Figure 3-1 Flow Chart of Simulation.

where V = freezing velocity, a and n are constants, T is the actual temperature and T_E is the equilibrium freezing temperature. All crystal growth velocities are then normalized by the maximum velocity calculated, resulting in values between zero and one. The normalized velocities are used as the probability of site growth of one unit in a time period of 1/(maximum velocity).

Since at a given driving force, freezing is energetically favored at sites adjacent to existing ice crystals and to a lesser extent at sites adjacent to a solid surface, these probabilities are modified (increased) based on calculations related to the energetics of ice nucleation. A random number generator is then used to decide if growth will occur at a particular site in that time interval. After all sites have been given a chance to freeze, the latent heat of crystallization is distributed to the nearest neighbors and the density change and subsequent convective effects accounted for.

In other words, nucleation of the ice in the water is determined by applying a probability equation to each of the finite difference cells containing water. The points that nucleate are then treated as point sources of freezing, and the growth velocity of a nucleating point is used in the growth routine to determine if the point does indeed freeze.

Control is then shifted to the heat transfer subroutine. This subroutine makes use of the finite difference approximation to solve the unsteady state heat transfer equations. Heat transfer occurs for a time interval identical to that used in the freezing routine. The melting subroutine, similar in form to the freezing subroutine, follows. This routine allows sites to melt if the temperature conditions calculated in the heat transfer routine warrant it. The melting routine completes the sequence for the time period defined in the freezing routine. This process is continued until termination conditions are met.

Simulation Results

This simulation was used first to model the freezing of "ponded" water in a simple test case of a semi-infinite body of water (x-y direction) freezing on an insulated flat pavement surface. The water and pavement began at 0°C. Cooling was introduced by convection to air at -20°C with a windspeed of 5 mph. These conditions were intended to introduce cold from the air on top of the water, promoting freezing from the top down. Evaporation of the water was not considered in this test case; therefore, humidity was not a factor.

Example results of the computer simulation of the freezing process under these external conditions are given in Figure 3-2. A zero thickness layer of water at a given level in the z-direction is shown as an array of numbers representing the x-y plane. The numbers 5 and 6 are reserved for the surface layer (e.g., z = 1.050) while the numbers 1 and 2 are reserved for interior layers (e.g., z = 0.900). The nucleation of the first crystal did not start until 450 seconds after initial exposure and then freezing proceeded very rapidly. A value of six within the matrix represents surface water while a value of five represents

450.10 Sec

```
x |   Z = 0.900
-------------------------------
8 |   2 2 2 2 2 2 2
7 |   2 2 2 2 2 2 2
6 |   2 2 2 2 2 2 2
5 |   2 2 2 2 2 2 2
4 |   2 2 2 2 2 2 2
3 |   2 2 2 2 2 2 2
2 |   2 2 2 2 2 2 2
1 |   2 2 2 2 2 2 2
-------------------------------
Y |   1 2 3 4 5 6 7
```

453.97 Sec

```
x |   Z = 0.900
-------------------------------
8 |
7 |
6 |
5 |
4 |
3 |
2 |
1 |
-------------------------------
Y |   1 2 3 4 5 6 7
```

450.00 Sec

```
x |   Z = 1.050
-------------------------------
8 |   6 6 6 6 6 6 6
7 |   6 6 6 6 6 6 6
6 |   6 6 6 6 6 6 6
5 |   6 6 6 6 6 6 6
4 |   6 6 6 6 6 6 6
3 |   6 6 6 6 6 6 6
2 |   6 6 6 6 6 6 6
1 |   6 6 6 6 6 6 6
-------------------------------
Y |   1 2 3 4 5 6 7
```

450.05 Sec

```
x |   Z = 1.050
-------------------------------
8 |   6 6 6 5 6 6 6
7 |   6 6 6 6 6 6 6
6 |   6 5 5 6 5 5 6
5 |   6 6 6 6 6 6 6
4 |   6 6 6 6 6 6 6
3 |   6 6 6 6 6 6 6
2 |   6 6 6 6 6 6 6
1 |   6 6 6 5 6 6 6
-------------------------------
Y |   1 2 3 4 5 6 7
```

450.10 Sec

```
x |   Z = 1.050
-------------------------------
8 |   6 5 6 5 5 5
7 |   6 6 5 6 6 6
6 |   5 5 6 6 6
5 |   6 6 6 6 6 6
4 |   6 6 6 6 6
3 |   6 6 6 5 6 6
2 |   5 5 5 5 5 5
1 |   6 6 6 6 6 6 6
-------------------------------
Y |   1 2 3 4 5 6 7
```

450.01 Sec

```
x |   Z = 1.050
-------------------------------
8 |   6 6 6 6 6 6
7 |   6 6 6 6 6 6
6 |   6 6 5 5 6 6 6
5 |   6 6 6 5 6 6 6
4 |   6 6 6 6 6 6 6
3 |   6 6 6 6 6 6 6
2 |   6 6 6 6 6 6 6
1 |   6 6 6 6 6 6 6
-------------------------------
Y |   1 2 3 4 5 6 7
```

453.97 Sec

```
x |   Z = 1.050
-------------------------------
8 |   2 2 2 2 2 2
7 |   2 2 2 2 2 2
6 |   2 2 2 2 2 2 2
5 |   2 2 2 2 2 2 2
4 |   2 2 2 2 2 2 2
3 |   2 2 2 2 2 2 2
2 |   2 2 2 2 2 2 2
1 |   2 2 2 2 2 2 2
-------------------------------
Y |   1 2 3 4 5 6 7
```

Figure 3-2 Material Profiles from Computer Simulation of The Freezing Process. Initial conditions: water, 0°C; pavement,0°C; air, -20°C; wind speed, 5 mph. Nucleation occurs at 450.000°C. Each grid division is 0.150 cm.

surface ice. A _two_ represents interior water, and a _one_ represents ice.

Consideration of the examples in Figure 3-2 reveals that the layer of water at the surface (z = 1.050) froze earlier than the layer in the interior (z = 0.900), as expected intuitively for the given boundary conditions. However, the freezing in the surface layer did not progress simply and uniformly. Figure 3-2 shows that some local melting took place after initial freezing even though the external temperature had not increased.
Apparently the latent heat of crystallization could not be conducted away fast enough, ultimately slowing the freezing, and also causing local melting.

Next, a series of computer runs simulating nonsimple cases of ice freezing on actual pavement for a variety of conditions was made. The conditions that were varied were: average stone size and spacing, vertical roughness, initial pavement temperature, wind speed, and air temperature. The stone size was expressed as the horizontal cross sectional area of the stones and the spacing was expressed as the average center-to-center distance. The vertical roughness (pavement surface thickness) was defined as shown in Figure 3-3.

Values for stone size, stone spacing, and vertical roughness were set together as trios:

0.15 cm^2, 0.40 cm, 0.4 cm;
1.0 cm^2, 1.2 cm, 0.4 cm;
0.15 cm^2, 0.40 cm, 0.2 cm;
1.0 cm^2, 1.2 cm, 0.2 cm.

Values for initial pavement temperature were set as individuals:
$0°C$,
$10°C$,
$20°C$.

Values for wind speed and air temperature were set as pairs:
5 mph, -20°C;
5 mph, -30°C;
10 mph, -20°C.

Taking all combinations of the variables corresponds to 36 simulation runs. We ran 26 simulations and evaluated the results. The nucleation times and temperatures for different conditions were extracted from the simulation output. The data generally showed a nucleation temperature closer to zero (less supersaturation) for large stones than for the smaller stones. Average nucleation temperature for large stones was -0.35°C, while for small stones it was -0.43°C. Correspondingly, the average time for nucleation was shorter for large stones than for sma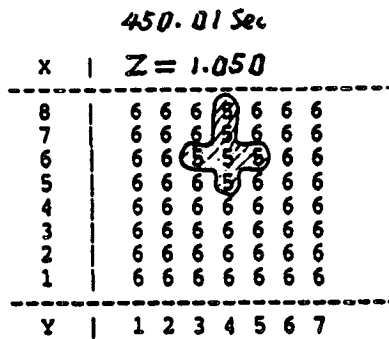ll stones. Large stones nucleated ice within 120 seconds, while small stones nucleated ice at about 180 seconds and longer.

Figure 3-4 shows the data identified by vertical roughness. A smaller vertical roughness

Figure 3-3 Vertical Roughness Used in Computer Simulation. The numerical value used is the vertical distance from minimum to maximum.

Figure 3-4 Nucleation Time Versus Temperature for Ice Freezing on Pavement. Each point represents a complete computer run with different initial conditions. On average, greater vertical roughness causes nucleation at slightly higher temperatures and shorter times.

17

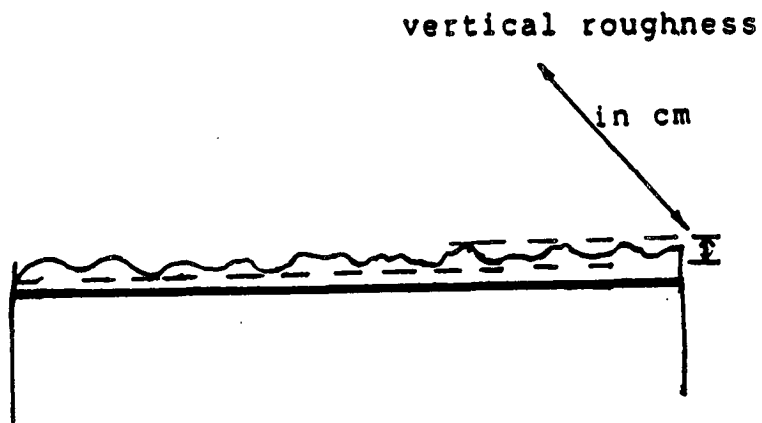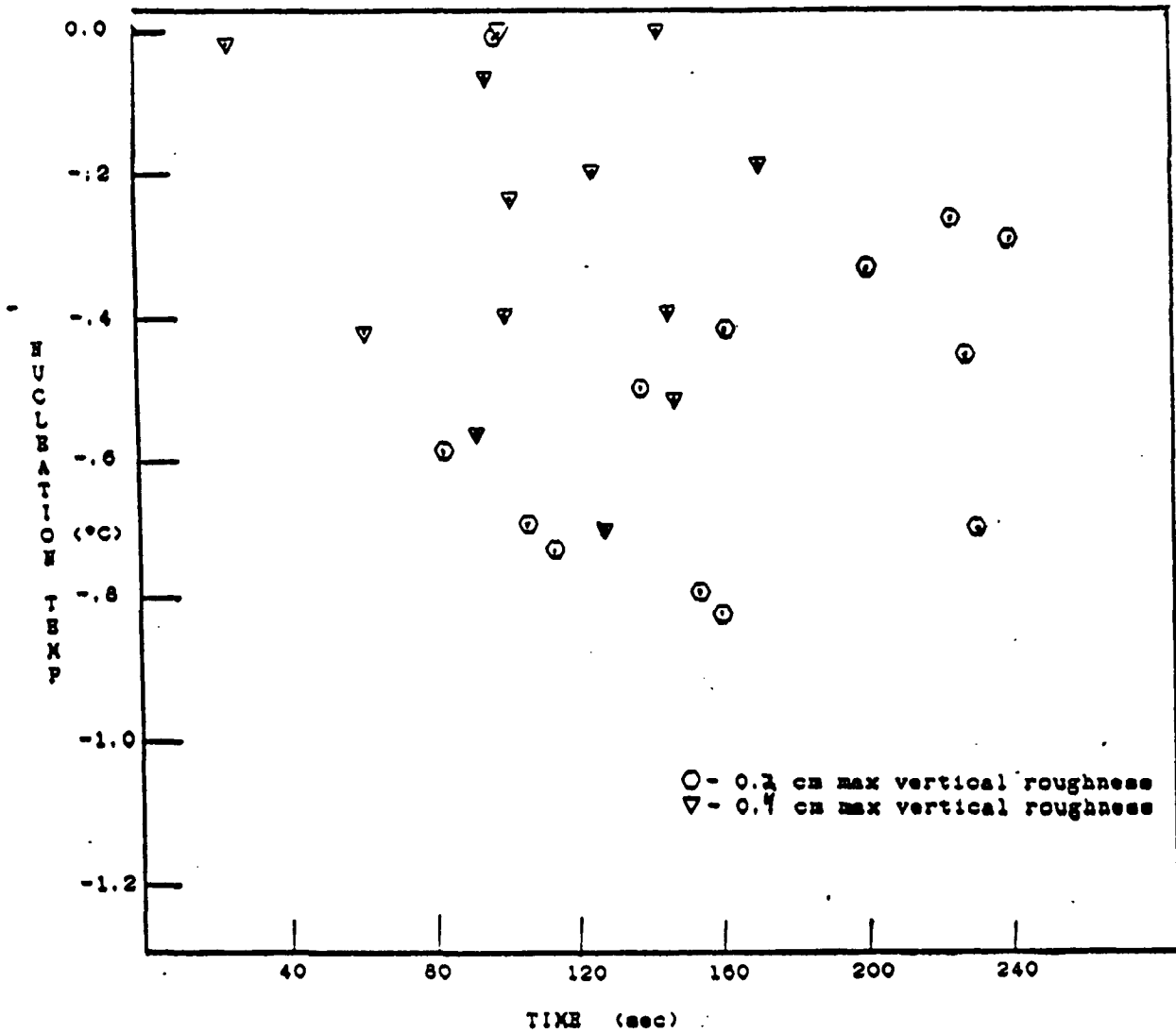in general had a longer nucleation time and/or a colder nucleation temperature. (Points for 0.2-cm vertical roughness are more toward the lower right of Figure 3-4, whereas points for 0.4-cm vertical roughness are more toward the upper left.) These results can be rationalized by considering that smaller vertical roughness traps a smaller volume of water, which necessarily has a smaller nucleation probability. On practical grounds, however, the differences in nucleation times or temperatures may be regarded as too small to warrant further study.

A more interesting result noted for the conditions studied is that the pavement temperature had little effect on the freezing of water at a distance of 2 mm or more from the pavement surface. That is, in this simulation, a cold pavement initially froze a very thin layer of ice, but after this the conditions in the bulk water predominated, in turn determined by the atmospheric conditions. What this means is that a thin layer of ice formed directly on the pavement and did not grow upward; meanwhile another layer of ice formed at the water-air interface and proceeds downward. The result is a junction of the two freezing fronts a few millimeters from the pavement surface. This simulated behavior occurred over the full range of variables studied, and can be interpreted in the following way:

1. Nucleation is more likely at the solid surface because of its roughness (hence more nucleation sites).
2. The heat released by crystallization at the pavement surface layer is conducted away slowly because of the low thermal conductivity of the pavement, thus preventing the newly formed ice layer from cooling to temperatures below 0°C. This in turn slows further crystal growth near the pavement surface compared to crystal growth elsewhere in the system.
3. During this period nucleation and growth at the air-water interface begins and is rapid.

The predicted junction of two freezing fronts near the substrate surface was found later in experimental observations made on small specimens prepared in the cold room.

Figure 3-5 shows the calculated average water surface and pavement surface temperatures as a function of time after 0°C-water was contacted to 0°C-pavement. In the first few minutes both temperatures dropped dramatically until nucleation occurred. Then both temperatures rose to very close to 0°C and remained at this temperature while freezing took place. For the particular case shown in the Figure 3-5, the downward moving freezing front reached the pavement surface between 140 and 160 minutes after the freezing starts. (This is in good agreement with the experimentally observed 120- to 180-minute freezing time for a specimen in the cold room with ambient temperature at -20°C.) The computed temperature of the pavement surface dropped quickly once the freezing front reached it and all the water was frozen. This is also in good agreement with experimental observation.

Figure 3-6 shows the simulation results for water surface temperature and the average temperature of the entire water volume at nucleation time for several cases. The water

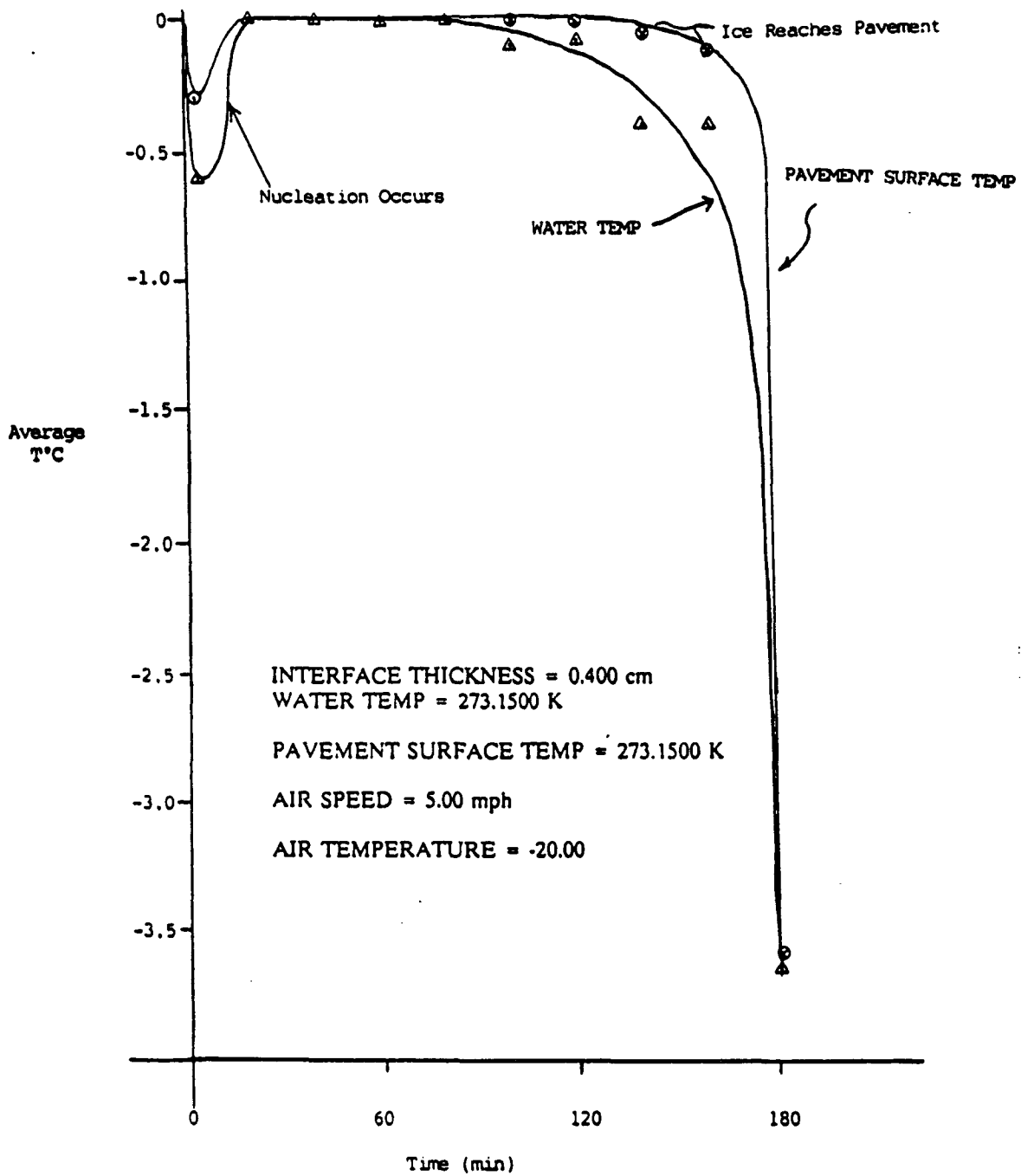Figure 3-5 Pavement Surface Temperature (⊘) and Water Temperature (▲) as a Function of Time. Each point represents an average over several computer runs under different conditions.

19
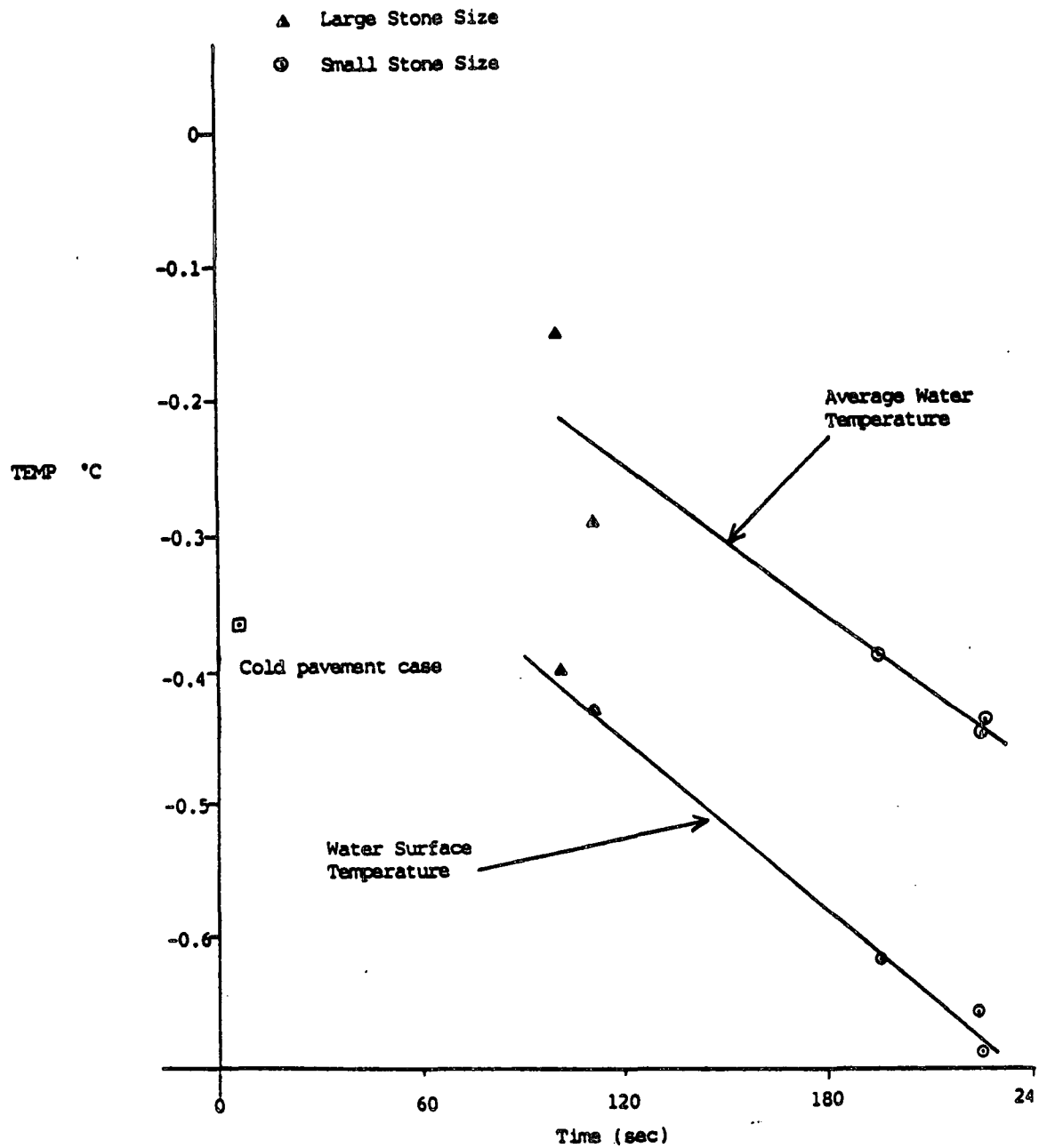
Figure 3-6 Computer Estimation of Time and Temperature of First Nucleation.

20

temperature was lower at the surface than in the bulk when nucleation first occurred. Also, in the presence of larger stones, the ice nucleated a little earlier and at slightly higher water temperature.

In sum, the results of the simulation point out that ice nucleation occurred below but very close to 0°C under a wide variety of atmospheric conditions, the nucleation temperatures being between 0° and -1°C. Also, nucleation occurred within 1 to 4 minutes (60 to 240 seconds) after the water temperature fell below zero.

In laboratory experiments, nucleation and crystal growth were seen to occur within a minute of the start of cooling. This is slightly faster than the 1 to 4 minutes predicted by the simulation. There could be several explanations for the discrepancy between simulation and reality. First, the nucleation probability calculated in the simulation is the probability that a nucleation occurs at a site within a one by one-half centimeter area of the entire specimen surface. This fact means that although the nucleation in the particular area modelled by the simulation may not occur in the given time interval, it may occur in another area of the specimen surface during this time.

Second, the simulation by its very nature cannot differentially determine the temperature gradient; therefore, the actual supercooling in a very thin layer may be greater than that calculated by the simulation, thus explaining why the actual nucleation time is shorter than the predicted nucleation time.

The third possible cause of nucleation time discrepancy is one of experimental procedure. It is possible that the near zero degree water in the actual experiment contains previously nucleated microscopic ice crystals which then grow visible in the short period of time observed. The simulation, of course, assumes no ice crystals at the start.

In addition to being used as described above to simulate the freezing of ponded water, the computer simulation was used to examine the freezing of water in an enclosed space, e.g., cavities in the pavement. In this case, the simulation proceeded as follows:

1. Calculation of new expected volume of ice and water,
2. Calculation of pressure change to return volumes to total,
3. Calculation of new masses of ice and water,
4. Calculation of new specific volumes,
5. Calculation of new equilibrium temperature,
6. Repeat above until entire new mass is frozen or triple point is reached.

Table 3-1 shows the results of the simulation for the constant volume freezing of ice using available thermodynamic data. Of particular note is the large pressure increase upon freezing of even 1% of the water present. For example, at -0.1°C pressure will have reached 36 atm. This points out the potential importance of ice freezing in cavities during the formation of an ice-pavement bond, a feature that was exploited later in our research program.

Table 3-1 Pressure rise during freezing as a function of initial volume of water trapped in an enclosed space.

Per Cent Frozen	Pressure, atm.	Temperature, °C
0.00	1.000	273.150
2.00	36.224	272.997
4.00	72.658	272.758
6.00	110.357	272.490
8.00	149.447	272.194
10.00	190.016	271.869
12.00	232.198	271.514
14.00	276.108	271.131
16.00	321.893	270.718
18.00	369.705	270.275
20.00	419.658	269.802
22.00	471.917	269.300
24.00	526.661	268.768
26.00	584.048	268.205
28.00	644.308	267.612
30.00	707.538	266.987
32.00	773.984	266.329
34.00	843.760	265.636
36.00	917.035	264.905
38.00	993.970	264.132
40.00	1074.655	263.312
42.00	1159.150	262.438
44.00	1247.502	261.500
46.00	1339.756	260.489
48.01	1435.823	259.392
50.01	1535.531	258.198
52.01	1638.906	256.896
54.01	1745.774	255.476
56.01	1855.988	253.936
58.01	1969.555	252.278

Triple point reached at 59.31%
    Pressure = 2045.096 atm
    Temperature = 251.145 K
    Volumes = 0.6263078 cm^3 ice I,
            0.3737055 cm^3 water.

In summary, the computer simulation mirrored results seen in the cold room. Neither the time to nucleation nor the exact nucleation temperature (which was always close to 0°C) was found to be strongly affected by variables such as pavement stone size, pavement surface layer thickness and thermal conductivity, pavement depth, wind speed, or pavement temperature (as long as it was below 0°C). Once crystals had nucleated, however, the freezing rate was found to be a strong function of the ambient temperature, wind speed, and thermal conductivity.

Probably the most interesting feature shown by the simulation is the formation of a distinct ice-ice junction just above the pavement surface when the air temperature and the pavement surface temperature both started below 0°C. This developed because the freezing from the pavement surface up halted shortly after it began, while the freezing front originating at the air-water interface proceeded all the way down through the water until it met the thin layer of crystals on the bottom.

4

Pavement Pore Freezing

The surface of pavement has numerous pockets, pores, and crevices into which water can penetrate and later freeze. Because of the unique expansion of ice at the freezing point, ice formed in blind pores would push tight against the walls, making strong mechanical interlocking. Also, prior to complete freezing, the water in the blind pore would experience higher and higher pressure with increasing volume of ice.

A pavement pore filled with water and covered on top with an ice cap is somewhat analogous to the above-described closed container. However, the pavement pore would be disrupted at some point by excessive build-up of internal pressure. For blind pores, fracture of the ice or the pavement and debonding at the ice-pavement interface might be expected. For pavement pores that are part of a network of pores and fissures, unfrozen water - trapped and pressurized - could be forced further into the network. Any of these events would relieve pressure.

Experimental verification of the predicted pressure build-up and changes in the ice-pavement system was undertaken. Continuous monitoring of temperature and pressure within the pavement pores was carried out during the freezing process. Because the naturally occurring pores at the surface of the pavement were too small to accommodate pressure and temperature sensors, larger pores were drilled in the surface. It was felt that expanding the scale of the experimental specimen in this way could be done with no loss of meaning and that experimental findings made on a series of large-scale cavities could be extrapolated with validity to the smaller scale of the actual process.

The pavement specimen was set up and instrumented as shown in Figure 4-1. It was approximately 100 mm in diameter and 75 mm thick, with a vertical hole of the selected diameter drilled in the center to a depth of 31 mm. Near the bottom of the specimen, a horizontal hole was drilled from the side of the pavement specimen to meet the base of the central vertical hole. The horizontal hole was filled completely with pressure transmitting fluid (silicone oil), and its walls were fully sealed with a coating of epoxy sealant to prevent escape of any of the oil into fissures in the surrounding pavement. A fitting was then glued into the horizontal hole where it emerged from the side of the pavement specimen.

A pressure gauge and valve assembly, already filled with oil, was attached to the fitting at the time of experiment. A pressure gauge with a range of 0-30 psi, marked in 1 psi increments, was found to be sufficiently sensitive for these experiments. The pressure changes experienced by the freezing water in the pore were transmitted by the oil to the gauge. The temperature of the gauge and valve assembly was itself monitored and controlled during the course of the experiments.
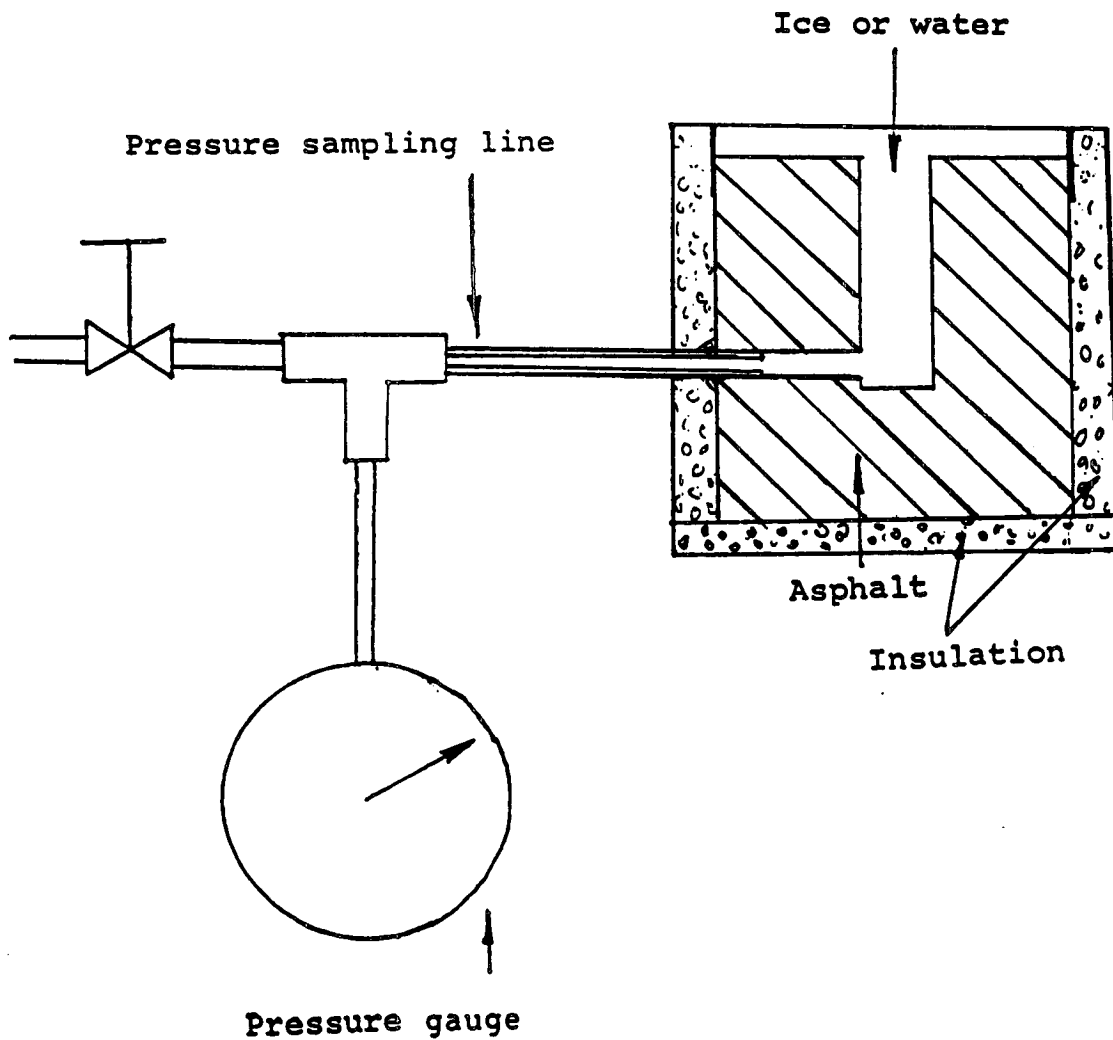
Figure 4-1 Experimental Apparatus for Pavement Pore Freezing Studies. Water is poured into the vertical hole and is ponded on the pavement surface for top-down freezing. The horizontal hole and line contain silicone fluid for transmission of pressure from vertical hole (pore) to pressure gauge. Thus pressure changes are monitored continuously during and after the freezing process.

A barrier extending approximately 25 mm above the pavement surface was constructed by wrapping common duct tape around the specimen. The purpose of this barrier was to prevent water poured on top of the specimen from running off. A thermocouple attached to the bottom surface of the pavement specimen monitored the vertical heat flow through this surface. Another thermocouple was affixed to the top surface of the pavement, near the pore. Finally, the sides and bottom of the specimen were insulated to retard heat loss through these surfaces.

Successful experiments could be conducted for the top-down freezing condition only, where the last water to freeze was that in contact with the oil of the transmission fluid line. Bottom up freezing experiments could not be done because the ice formed at the pore bottom immediately cut off the gauge from the pore, preventing collection of meaningful data.

The ambient environment was set to -20°C. Then water, cooled to near 0°C, was poured onto the specimen to fill the cavity completely and "pond" on the pavement surface to a depth of 10 mm. The clock was then started and readings of temperature and pressure were recorded at 20- or 30-minute intervals. During this time freezing was observed to start at the surface of the ponded water and proceed downward. When the freezing front had reached the pavement surface, readings were taken more frequently (five minute intervals) until a pressure rise was recorded. When the pressure started to rise, readings were taken at shorter intervals, e.g., one minute or so, depending on the rate of rise. These measurements were continued until the conclusion of the experiment, when the pavement surface temperature was less than -15°C or until the pressure had spontaneously dropped to zero and failed to rise again.

Typical experimental runs are graphed in Figure 4-2 (large central pore) and Figure 4-3 (small central pore). The pressure built up rapidly once the downward-moving freezing front reached the pavement surface (after about 120 minutes) and freezing within the pore started. As shown in Figures 4-2 and 4-3, after reaching a maximum, the pressure declined relatively slowly. The pressure maxima shown for the two runs are only about 5 and 13 psi above atmospheric, far less than the 36 atm (500 psi) predicted for freezing in a closed container at -0.1°C. This suggests that escape of the pressurized water from the pore has occurred, relieving pressure. After each experiment, the specimen was removed from the insulation and examined visually for evidence of cracking or pavement-ice separation. For several specimens, it was noted that there was ice in the insulation under the pavement specimen. Since no water had overflowed or leaked through the duct tape barrier around the top edge of the pavement, it was concluded that it came through the pavement's network of fissures.

Separate experiments on sealed-wall pores indicated that an internal pressure of 20 or more atmospheres of pressure (300 psi) was required to crack a 10-mm thick layer of ice frozen to the pavement surface. Such pressures do not separate the ice-pavement interface, but crack the ice itself. Clearly, it is easier for the system to relieve pressure by migration of water than by gross fracture of the pavement or ice cap.

Figure 4-2 Pressure and Temperature Changes Occurring in a Pore at the Pavement Surface as the Freezing of Ponded Water Proceeds. Note the rapid decrease in pavement surface temperature after 120 minutes; this signals that the downward freezing front has reached the pavement surface. The pressure rise marks the beginning of freezing within the pore.
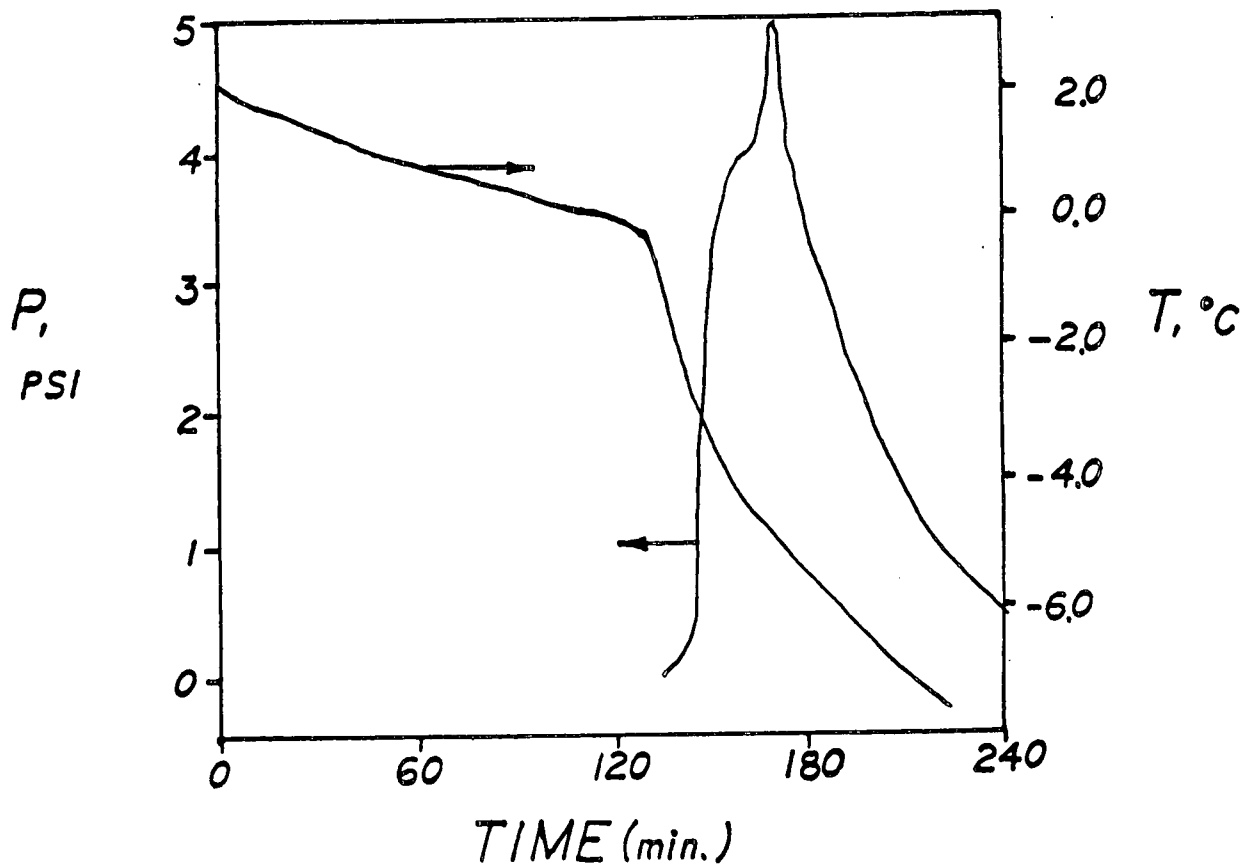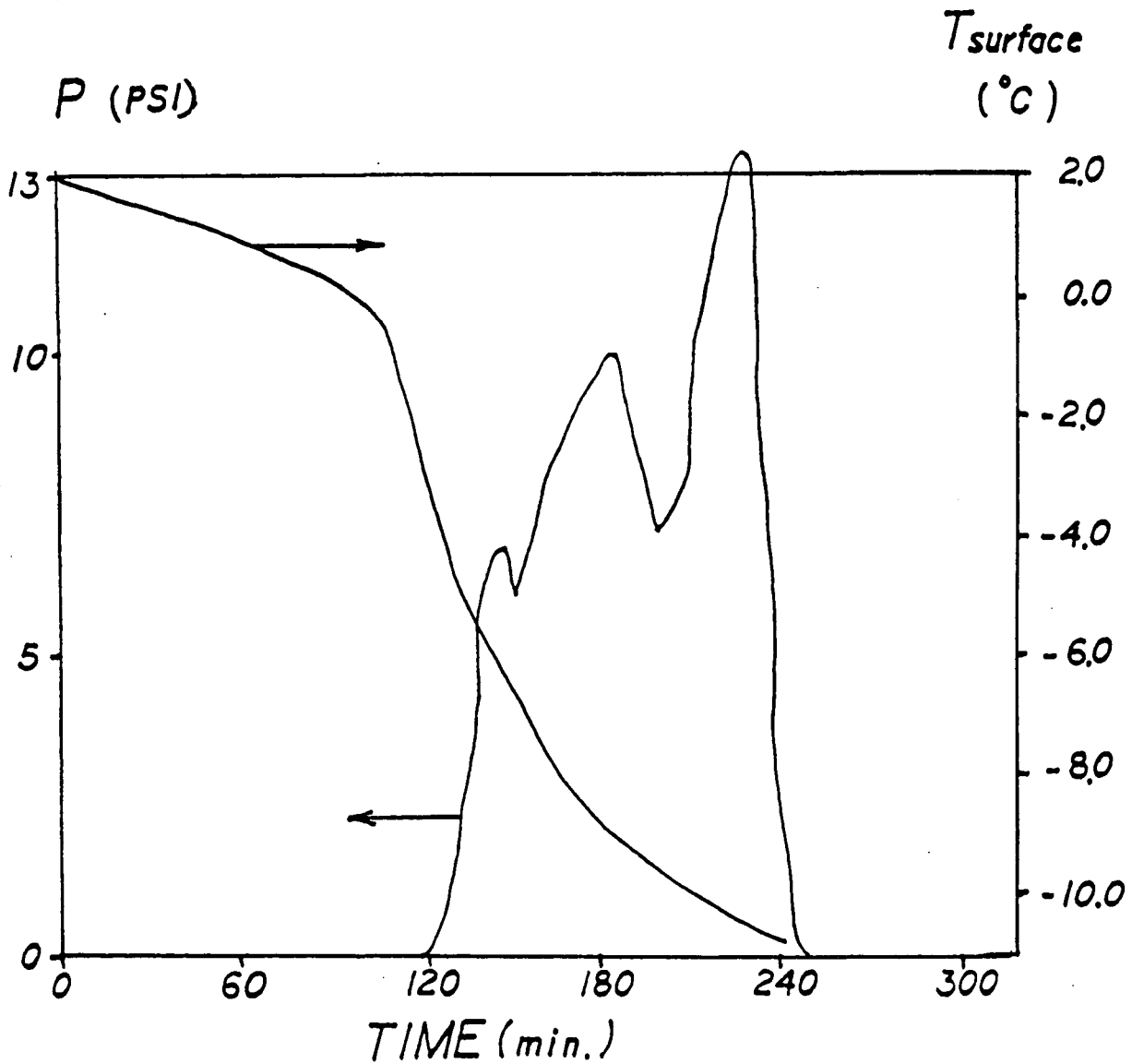
28

Figure 4-3 Pressure and Temperature Changes occurring in a Pore at the Pavement surface as the Freezing of Ponded Water Proceeds. The rapid temperature decrease at about 110 minutes indicates that the freezing front has reached the pavement surface. The pressure rise at the same time indicates that freezing of the water within the pore has started.

There was wide scatter in pressure data among pavement specimens, consistent with variability in the pore network details. On the other hand, a repeat experiment on the same specimen after drying gave a second pressure profile identical to the first. This reproducibility within a specimen and variability from specimen to specimen showed that the details of pressure build-up are dependent on the details of the fissure network within the pavement.

The maximum value of pore pressure is plotted against pore diameter in Figure 4-4. Because of the large scatter for specimens of the same diameter, no correlation between pore diameter and pore pressure is evident. (Values within 0.5 psi of each other are repeat runs on the same specimen.) All the pavement specimens are from a single road surface; therefore the scatter reflects the variability in pore network from spot to spot over the pavement.

A comparison was also made of pressure build-up inside the pore for sealed versus unsealed pore walls. First the pressure experiment was conducted for a pore with normal, uncoated walls. Then the walls of that same pore were coated with an asphalt sealer, and the pressure experiment was conducted again. Results for two different cavities, before and after coating, are shown in Figure 4-5. For both cavities, coating allowed a higher pressure to be reached. The effect was especially noticable for the 1.59-mm pore, which, when unsealed, showed no pressure build-up at all. These results confirm a pore network exists in the pavement, and that pressure in a given pore can be relieved by the migration of water further into the network.

Unfortunately, the opaque pavement specimens did not readily yield further information. We could not see what was happening within the block of pavement to coordinate details of the freezing process to the pressure changes experienced by the system. Also the large scatter in pressure maxima among pavement specimens was troublesome. These factors made it impossible to assess the relation between pore size and internal pressure in a meaningful way. However, the phenomenon of ice formation and presssure build-up in pavement pores is a very important one. Such pressures, if understood, could be used to weaken or break the ice-pavement bond.

To get a better understanding of the process of trapped water freezing in a pore, we decided to use transparent material instead of pavement. By using clear plastic in place of the opaque pavement, we were able to monitor the pressure and watch for cracking, debonding or system leaks simultaneously. Specimens of transparent polymethyl methacrylate were made, with smooth walled pores of various sizes drilled in them.

Figure 4-6 shows the experimental configuration. The "pore" was a small cylindrical hole drilled in the surface of the specimen. This pore could be filled partially, completely, or overflowing with water. In subsequent experiments it was drilled to larger diameters. The pore was connected at the bottom to an oil reservoir which in turn was connected directly by a brass fitting to the pressure gauge in the bottom of the clear plastic cylindrical specimen.
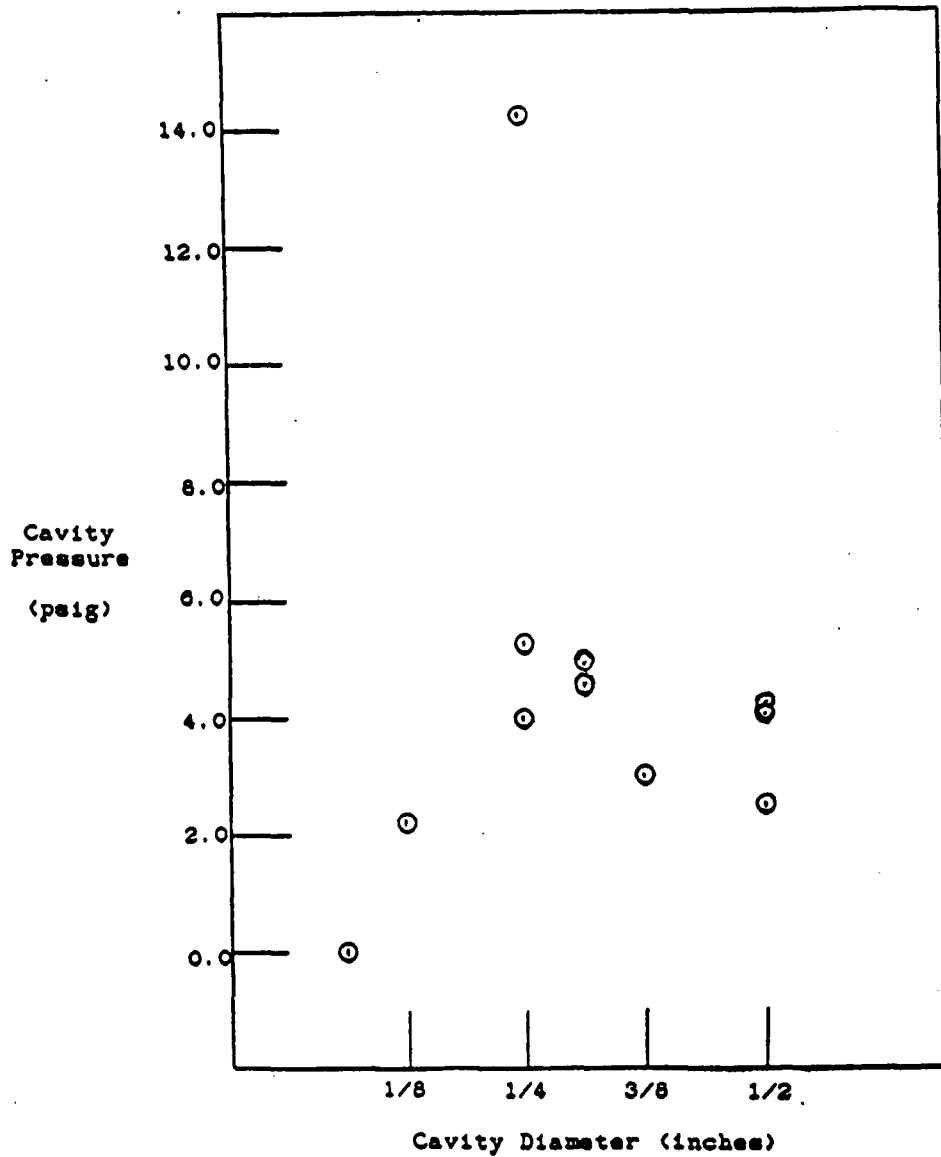
Figure 4-4 Maximum Pore Pressure Versus Pore Diameter. There is large variation and no correlation, undoubtedly due to inherent differences in pavement specimens. Repeat runs on a specimen were reproducible and are shown by pairs of values within 0.50 psi of each other.

31
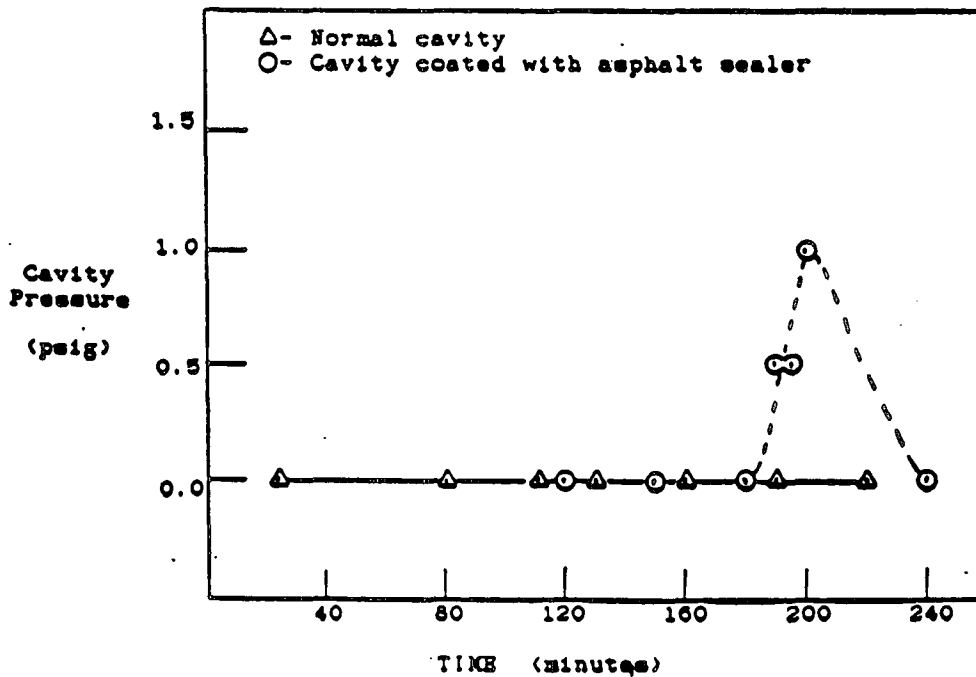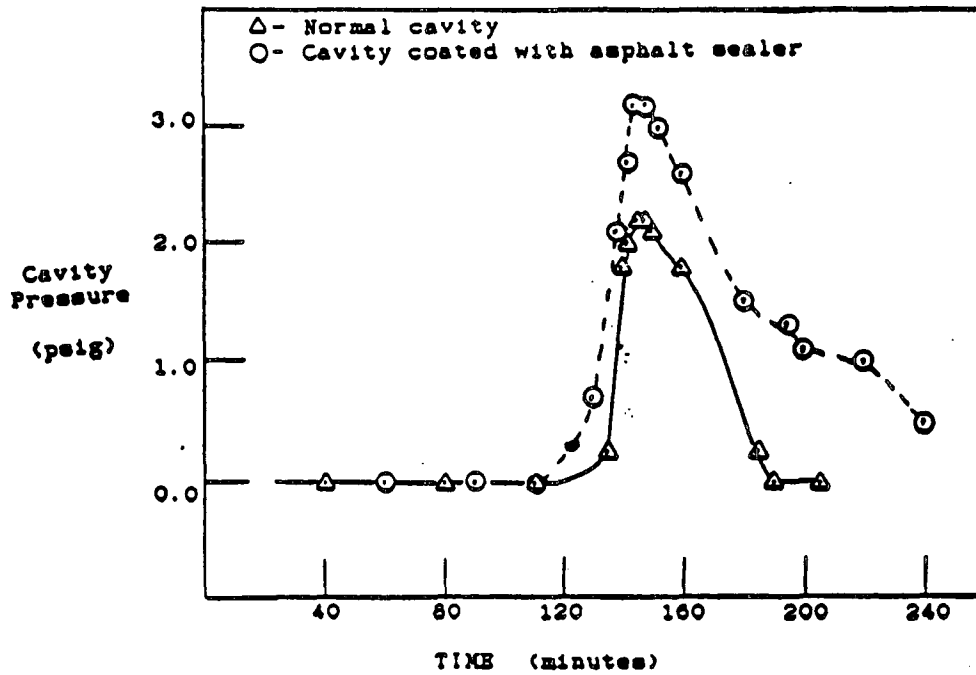
Figure 4-5 Pressure Profiles in Pores with and Without Sealed Walls. Sealing the walls causes higher pressure maximum in 1.41-mm pore (top) and 1.59-mm pore (bottom).

32
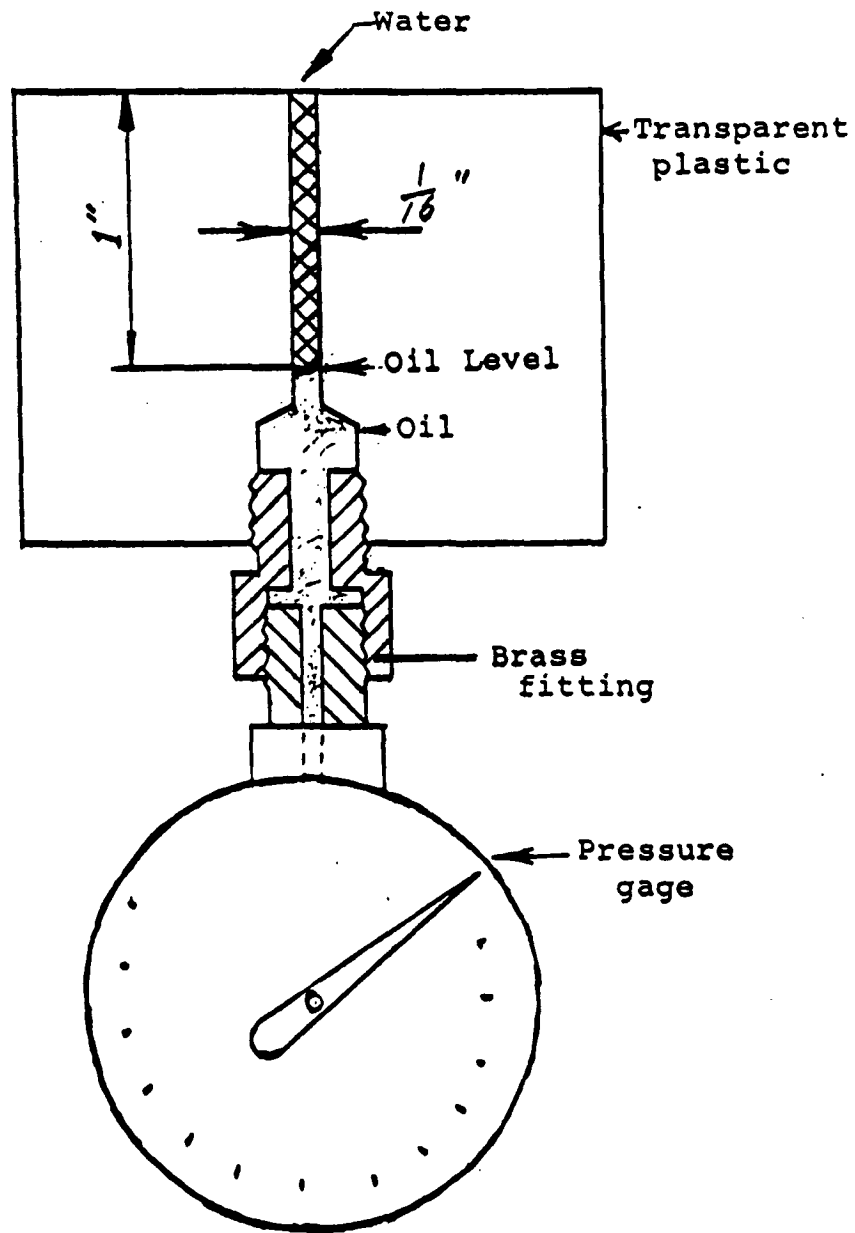
Figure 4-6 Pore Freezing Experiment Geometry. The central pore in the transparent plastic is filled fully or partially with water. Oil transmits the pressure in the freezing water directly to the gauge at bottom.

A thermocouple (not shown in Figure 4-6) was placed in the oil reservoir so that temperature changes therein could be evaluated. At the beginning of the experiment the oil temperature had to be above 0°C in order that it not nucleate crystallization of the water in contact with it. Unwanted occurrence of crystallization at the water-oil interface would seal the pore at the bottom and terminate the experiment before the start. Another thermocouple was placed in the water, near the water surface. The two thermocouples indicated that, as soon as the water was placed in the pore, both water temperature and oil temperature began to drop. The total oil volume in the system was 5 ml, which gave a contraction of 0.006 ml for every 1°C drop. Visual evidence of the oil's thermal contraction was provided by the slow downward movement of the oil-water interface as the oil temperature dropped.

Pressure profiles were similar in their general features to those obtained on pavement. When the air temperature was cold enough to give top down freezing, an ice cap formed that sealed the pore from the atmosphere, and a rapid pressure rise occurred. The gauge measured the net pressure, which was the sum of the pressure rise due to expansion of ice at freezing and the pressure decrease due to thermal contraction of the oil. At first, the ice expansion dominated the overall pressure, which exhibited a steady increase. The pressure maximum occurred just as the water freezing in the pore reached completion and expansion of the ice ceased. Then the pressure began to drop as the temperatures of both the ice and the oil decreased with that of the surroundings.

Interestingly, the temperature of the oil in contact with the brass fitting responded quickly to imposed changes in air temperature and also showed quick corresponding pressure changes on the gauge as it expanded and contracted in response to external increases and decreases in temperature made by the experimenter. The temperature of the ice in the pore, insulated by the surrounding plastic, responded sluggishly to ambient temperature changes. These differences in response speed reflect the different thermal conductivities of separate parts of the system.

The observations made in this ideal system dramatized the pre-sence of temperature gradients in any system where the external temperature is different from the freezing temperature of water. The thermocouples showed temperature gradients to be present during the freezing process and also after completion of freezing whenever changes in ambient temperature occur. The pressure gauges showed that internal pressure changes occur not only during freezing, but also after completion of freezing. It is these pressure changes that although complicated, should be viewed as a possible tool for attacking the problem of ice adhesion.

The pressure generated within the specimen is actually internal or residual stress, a condition well known to structural engineers. To use the pressure, or residual stress, to our advantage, we had to learn how to manipulate it. For this, the experiments described below were conducted.

The relation between water volume and pore pressure was evaluated using transparent specimens with different pore diameters. The results are tabulated in Table 4-1, and are

Table 4-1 Initial water volume in pore versus pressure maximum in pore freezing experiments.

Pore Diam., mm	Water Volume, ml	Max. Pressure, psi
1.587	0.0504	0*
3.175	0.201	0.7
6.350	0.804	21.5
7.938	1.26	30
9.525	1.81	95**
9.525	1.81	112**

* Oil contraction completely counteracted the small pressure build-up in this small volume of water.
** Ice plug emerged from pore at completion of freezing.

shown graphically in Figure 4-7. As was expected for top down freezing of completely filled pores, a larger initial volume of water meant more water trapped during freezing and a correspondingly higher maximum pressure. Note that the relation between volume and pressure is not linear. Analogous experiments run on a pore of a fixed diameter filled to different levels also gave a similar nonlinear relation between volume and maximum pressure.

A most interesting phenomenon occurred in the pore with the largest water volume. When the maximum pressure was reached, the whole ice plug within the pore pushed upward a distance of about 2 mm. Obviously, the ice plug had to experience debonding from the pore wall in order for this displacement to occur. Repetition of this experiment gave the same result. This was definitive evidence that the internal pressure build-up generated enough residual stress to cause debonding of the ice.

Freezing patterns other than top down could be obtained by changing the ambient conditions. Freezing could be made to proceed from the pore wall inward, from the bottom up, or in some combination. Whenever the freezing pattern was such that it diminished the volume of "trapped" water early in the experiment, maximum pressure was diminished. The extreme case was bottom up freezing which cut off the oil line immediately and resulted in zero gauge reading throughout the freezing process.

Analogous phenomena would be expected in pavement. True top down freezing of water on pavement would be expected to generate the maximum pressure within pavement pores. This pressure would act either to drive water further into the pore network of the pavement or to debond the ice from the pavement in the case of blind pores. Bottom up freezing would be expected to isolate the bulk pavement from further water penetration (and associated damage) and would not offer any force for debonding.

To exploit these findings, we conducted experiments on a clear plastic specimen with a larger top surface, used to represent the pavement surface. A shallow cylindrical hole was drilled in the center, as shown in Figure 4-8. The top drawing shows the early stages of top down freezing, which is easy to achieve in a material of low thermal conductivity. The bottom drawing shows the completely frozen ice plug debonded and displaced upward from the "pavement." Note that debonding occurred from the pavement's horizontal surface as well as from the pore walls. The debonding shown in Figure 4-7 occurred without any externally applied load.

Obviously the internal stress generated within the ice-substrate bonded joint can be considerable under the right conditions. The unique expansion of ice as it freezes is the apparent source of the stress. If the water that is last to freeze is trapped within the system, even a small amount of it can rupture the system upon freezing.

This experiment was extended to a larger surface with cylindrical pores distributed around the surface, as illustrated in Figure 4-9. Again, complete and spontaneous debonding was achieved.
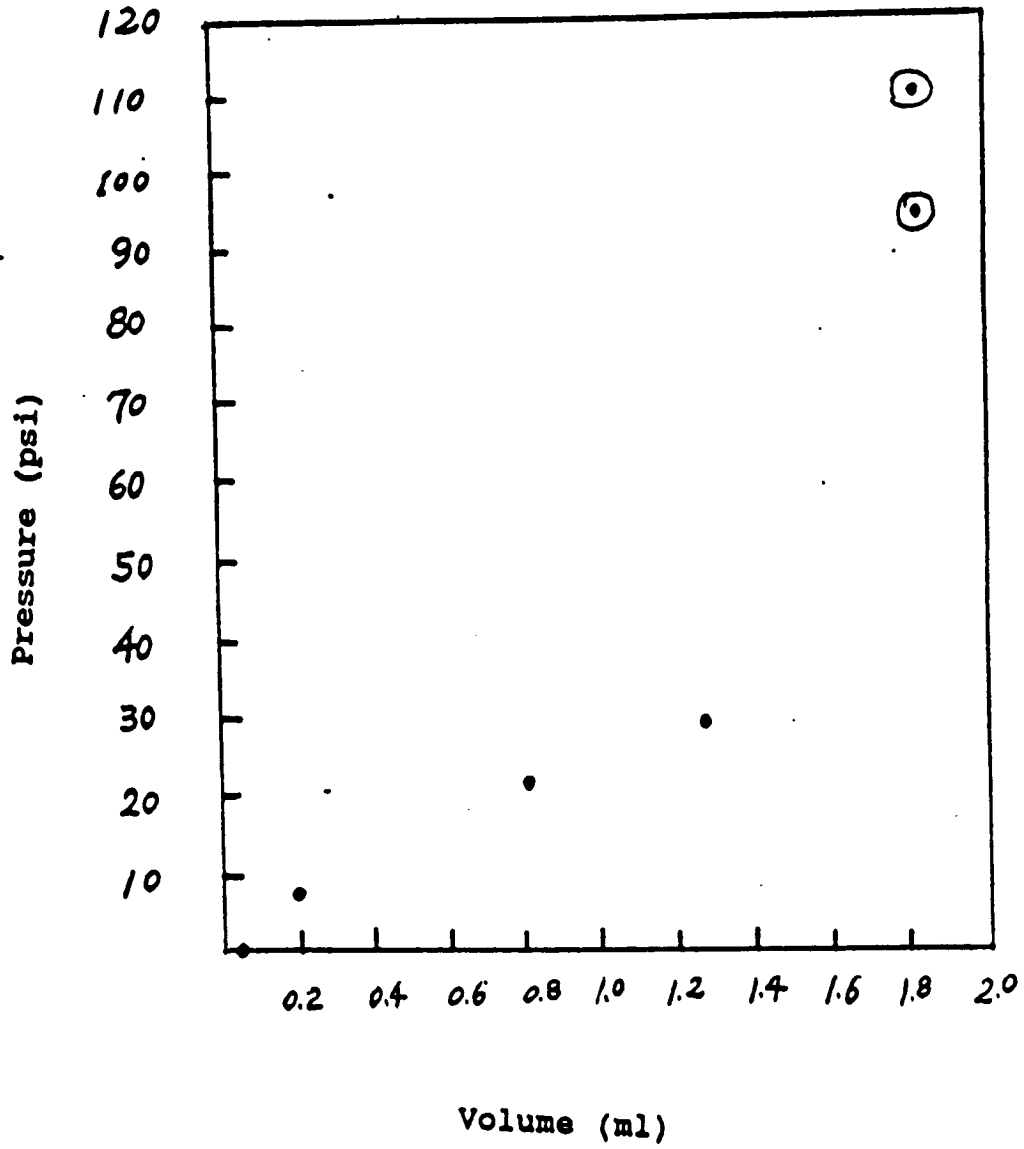
Figure 4-7 Pressure Maximum Versus Initial Water Volume in Pore Freezing
Experiment. Circled points exhibited ice plug debonding.
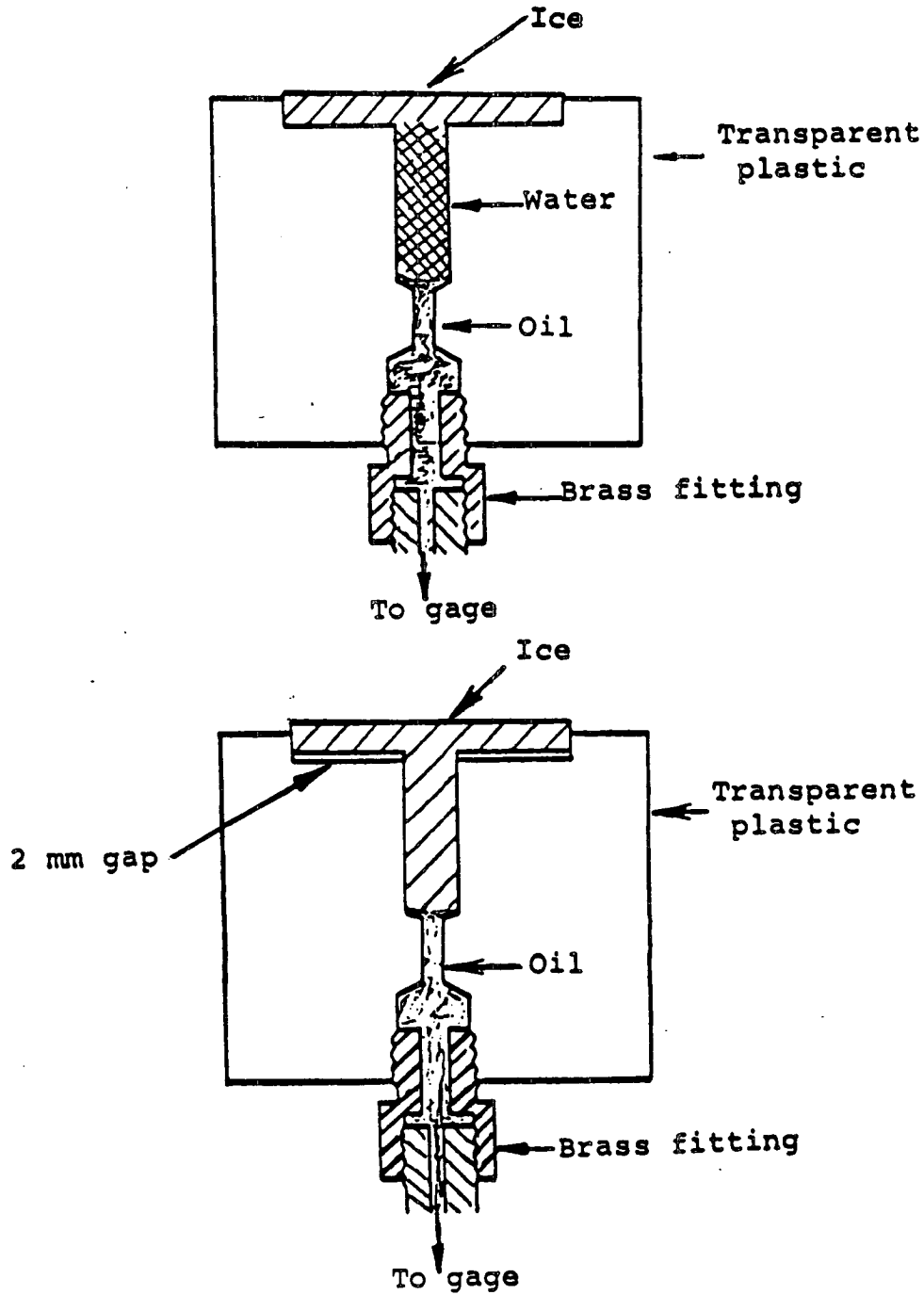
Figure 4-8 Spontaneous Debonding of Ice from Substrate of Intermediate Surface Energy. Top drawing shows freezing process with water at bottom of pore not yet frozen. Bottom drawing shows the ice plug, debonded and displaced upward, upon completion of freezing.
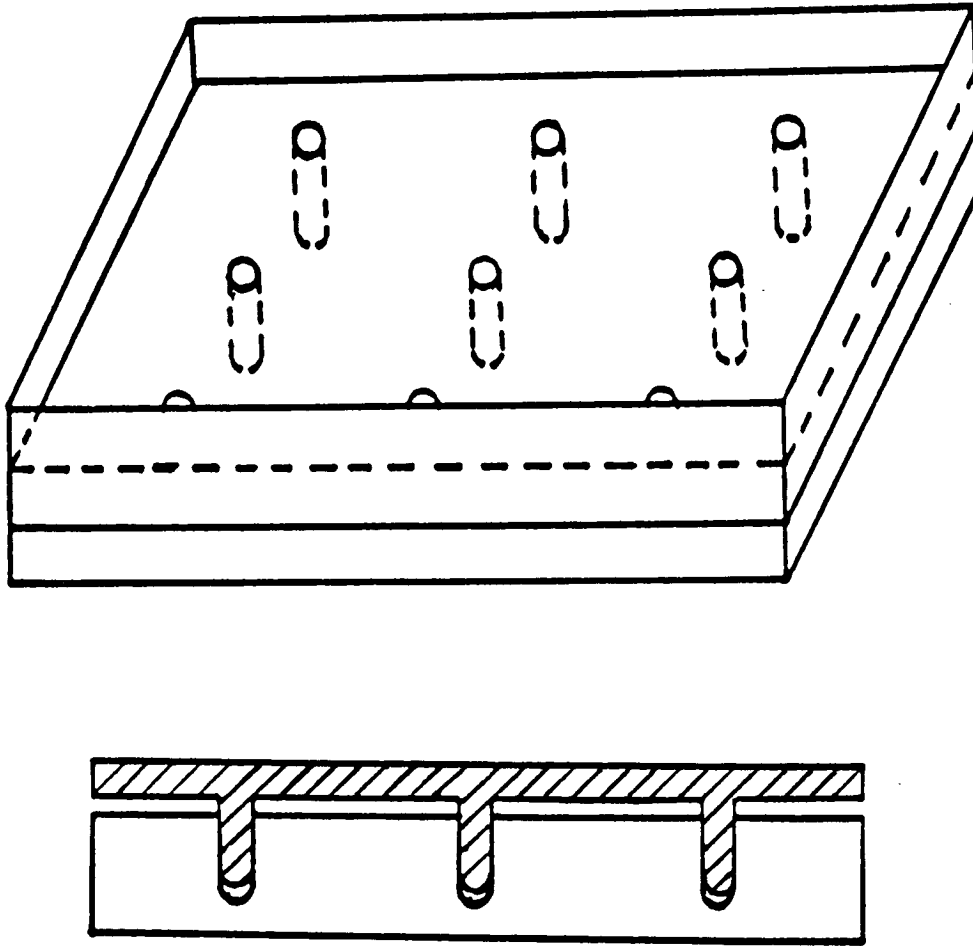
Figure 4-9 Water Freezing on Flat Plastic Surface with Pores. Upon completion of freezing, the internal pressure build-up is sufficient to debond the whole interface.

The experiment was attempted on an asphalt pavement into which 6.35-mm diameter holes had been drilled. In this case spontaneous debonding did not occur. We attributed the lack of debonding to the water's migration under pressure into the network of fissures in the pavement bulk. The relief of internal pressure in the pavement pores by this means, as demonstrated earlier, overrode debonding.

To overcome the pressure relieving mechanism in natural pavement, small nonporous rubber cups, open end up, were fitted into the drilled cylindrical pores to serve as a nonporous lining. This pavement surface, when covered with water and subsequently frozen, exhibited spontaneous debonding of the ice immediately adjacent to each up. However, regions of ice, centered between pores, still remained unbonded.

Several conclusions stand out from the work described in this section. Pressure builds up in pavement pores due to the expansion of ice in the freezing process. This pressure can be relieved by migration of water further into the network of pores and fissures. However, if the walls of the surface pores are sealed, cutting the pore off from the network, the pressure cannot be relieved. Unrelieved pressure in a blind pore can be used to cause debonding of the ice cap from the pavement surface.

5

Infrared Spectroscopy

Knowledge of the chemical structure and chemical functional groups in the surface layer of a substrate can contribute to understanding the causes of adhesion. For example, it is well established that polar groups or hydrogen bonding groups in a substrate surface promote adhesion to polar or hydrogen bonding adhesives.

Analysis of the functional groups present in asphalt concrete was carried out by infrared spectroscopy. This technique is suitable primarily to organic functionalities, so only the asphalt concrete was subjected to analysis. A Shimadzu Model 435 (Columbia, Maryland) automated infrared spectrophotometer was used. A thin layer of asphalt material, 1.0 micron thick, was mechanically removed from aged pavement surface, dissolved in dioxane and deposited on a transparent salt disc for transmission spectroscopy. Similar specimens were prepared from unexposed (unaged) asphalt by taking material from well below the surface of the pavement slab.

The two spectra are shown in Figure 5-1. Both exposed (aged) and unexposed asphalt exhibit the peaks for C-H stretch at 2800 cm^{-1} and for -CH_2- bend at 1470 cm^{-1}. These are characteristic of aliphatic hydrocarbons (7) as would be found in asphalt. Both materials also show a weak but broad peak at around 3400 cm^{-1}, not given an assignment.

The exposed asphalt (top) exhibits peaks not found in the unexposed asphalt (bottom). These can be assigned with confi-dence to the carbonyl group (C=O stretch at 1720 cm^{-1}) and the hydroxyl group (O-H bend and C-O stretch at 1000 cm^{-1} and 1360 cm^{-1}, respectively). The peak at about 3400 cm^{-1} that should also be displayed by -OH is apparently masked by the existing broad peak at 3400 cm^{-1} present in both asphalts. These species found in the surface of the exposed asphalt are typical of oxidation products of carbon such as ketones, aldehydes, or carboxylic acids.

The infrared spectra clearly reveal that asphalt pavement, upon exposure to the environment, ages by oxidizing. The oxidation products are present in large enough amount to be clearly detectable by infrared spectroscopy. The significance of these oxidation products is that they have the potential for strong polar interactions and hydrogen bonding with water or ice, thereby increasing the magnitude of interaction across the ice-pavement interface and enhancing adhesive bonding. In sum, the infrared data alone predict higher ice adhesion for the exposed asphalt than for the unexposed.
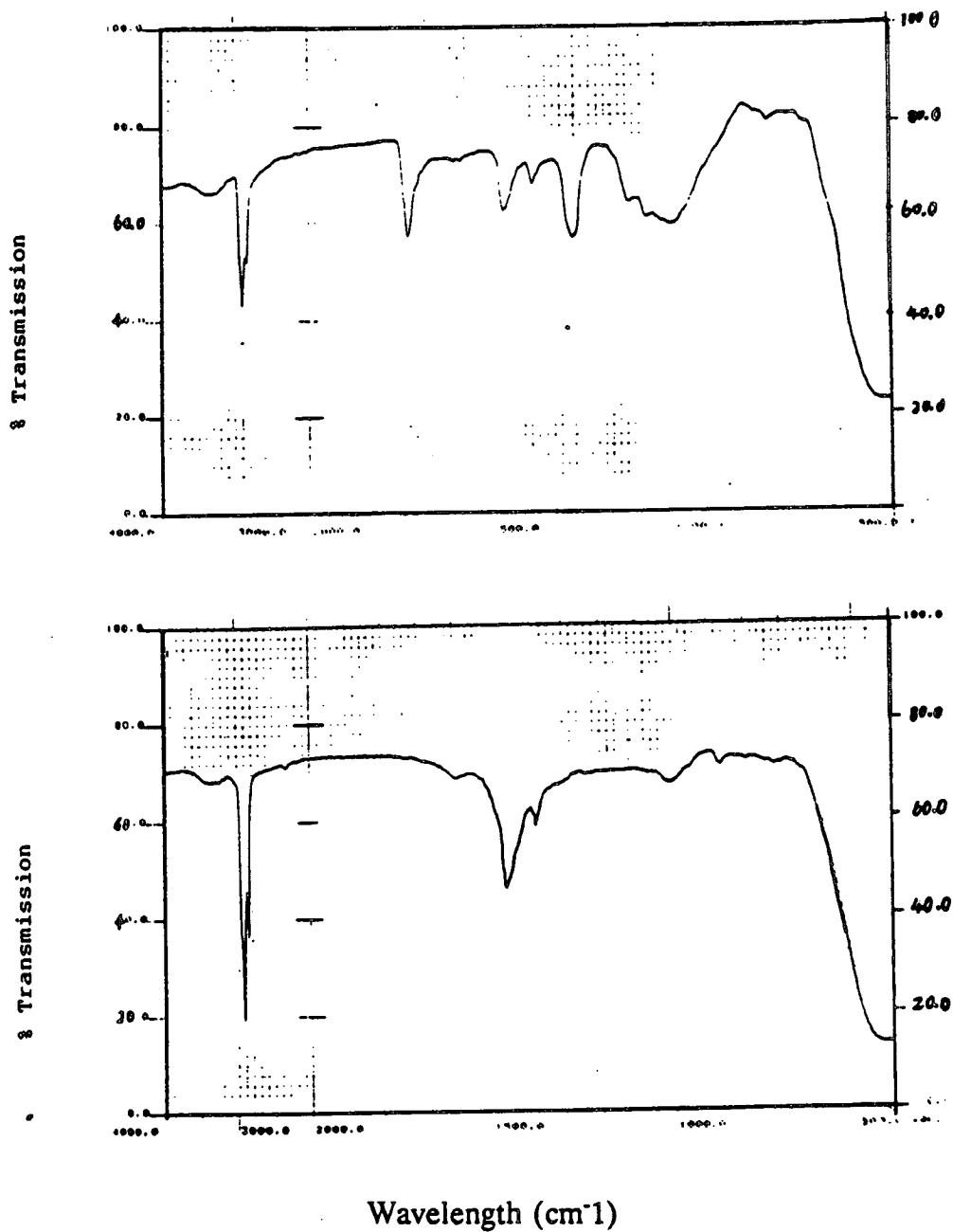
Figure 5-1 Infrared Spectra of Exposed (aged) and Unexposed (Unaged) Asphalt from Pavement. The aged asphalt from the pavement surface (top) shows carbonyl (1720 cm^{-1} and hydroxyl (1360 and 1000 cm^{-1}) peaks due to oxidative aging, in addition to the expected aliphatic hydrocarbon peaks (2800 and 1470 cm^{-1}) of unaged asphalt.

6

Surface Energy and Work of Adhesion

Two of the energy quantities important to adhesion are surface free energy and work of adhesion. The surface free energy of a condensed phase (liquid or solid) is related ultimately to the nature and arrangement of the atoms and molecules the surface comprises. It arises from the imbalance between the interior (bulk) of a material, where mutual interactions among neighboring molecules are balanced, and the exterior, where lack of neighbors on one side leaves the surface atoms or molecules with "free" energy. Unfortunately, the surface energy of a solid cannot be measured directly; the required reversible deformation of the surface alone is impossible in practice, as all experimental methods involve irreversible deformation of the solid adjacent to the surface. Thus, solid surface energy must be determined indirectly using empirical methods.

The work of adhesion is intimately dependent upon the surface energies of the two substances meeting to form the interface. It is defined as the amount of energy involved in separating or creating a unit area of interface in a reversible process, i.e., assuming a flat cleavage plane and no involvement of remote molecules in the separation process (8). Similar to the surface energy, the work of adhesion between two solids cannot be measured directly, as the separation of the adherents involves energy dissipation that renders the process irreversible.

The methods used to compute work of adhesion and surface energy involve contact angles made by well characterized probe liquids on the solid surface of interest. Contact angles provide a measure of the interaction between a solid and a liquid. The exact value of the contact angle made by a probe liquid on the surface of a solid is a direct result of intermolecular interaction between them. (A given liquid will make a low contact angle on a high energy solid surface and will make a high contact angle on a low energy surface.)

The Wilhelmy wetting force method (9) was used in this research to determine contact angles of liquids on solid surfaces. This method involves use of a torsion balance to continuously measure the wetting force exerted by a probe liquid on a solid as the solid is slowly immersed in a liquid reservoir (Figure 6-1). The vertical component of the measured wetting force is the cosine of the contact angle. This method is more reliable than the frequently-used sessile drop method because it allows the experimenter to sample a considerable length of specimen surface rather than a single spot. Contact angles were determined on several substrates using two different probe liquids. These liquids were water and methylene iodide, selected to exploit the polar and nonpolar intermolecular interactions, respectively.

Since contact angles are valid only on smooth substrates that undergo no dissolution or
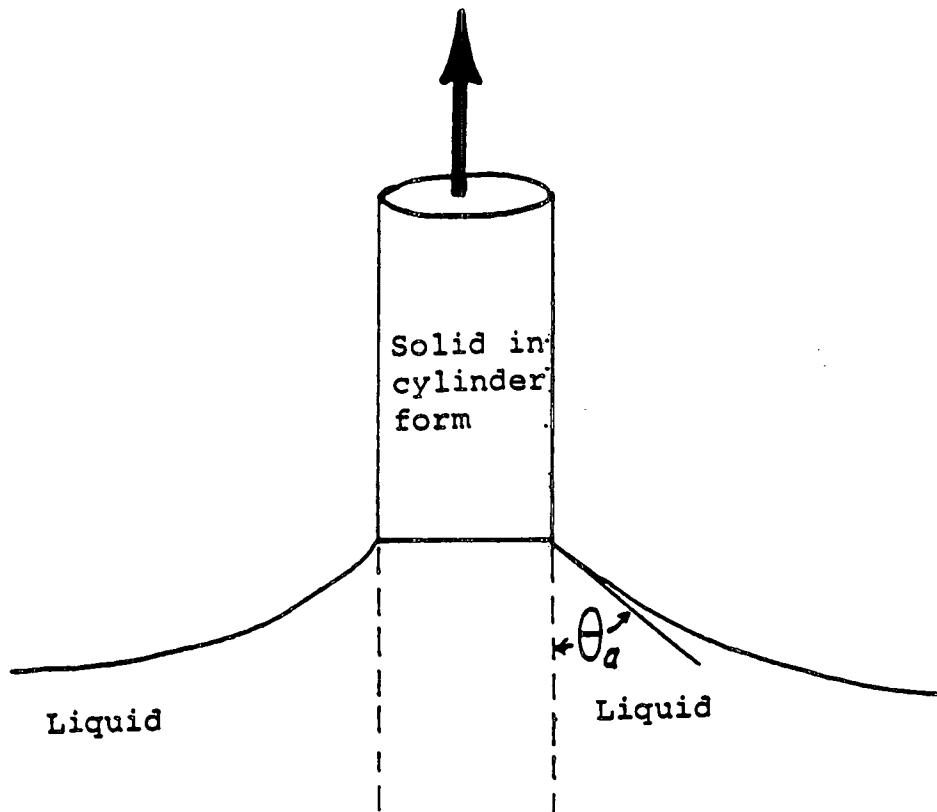
$$F = \gamma_L \, P \cos \theta_a$$

F = Wetting force measured directly from electro balance

γ_L = Surface tension of liquid

P = Perimeter of solid specimen

θ_a = Advancing contact angle

Figure 6-1 Wilhemy Method for Measuring Contact Angles. The liquid is advanced slowly upward along the specimen to obtain an average advancing wetting force. The advancing contact angle is computed from the wetting force.

penetration by contacting liquid, the actual pavement surfaces could not be used directly. Not only do both types of pavement have complicated surface roughness, but asphalt is dissolved by methylene iodide, and the pores of portland cement concrete are penetrated by both probe liquids. Thus, model substrates had to be used in the contact angle studies.

Polypropylene, insoluble in methylene iodide, was used as a model for unaged asphalt because the similarity of its surface atom content (C and H only). Polycarbonate, also insoluble in methylene iodide, was used as a model for aged asphalt because of the similarity of its surface atom content (C,H, and O). Glass, smooth and nonporous, was used as a model for portland cement concrete because of the similarity of its surface atom content to that of both the silicate aggregate and the sand comprising portland cement concrete. Finally, steel, polystyrene, and teflon were used as reference substrates.

The contact angle cosines for water and methylene iodide on all substrates examined are shown in Table 6-1. The importance of these values is that they can be used to compute work of adhesion, W_A, and solid surface energy, γ_S.

The work of adhesion is given by the equation,

$$W_A = \gamma_L (1 + \cos\theta_a),$$

where γ_L is the surface tension of the contacting liquid and θ_a is the advancing contact angle made by the liquid on the solid.

Table 6-2 presents the W_A values, computed from the contact angle cosines, for water and methylene iodide on the model and reference substrates. W_A values for pavement and other substrates are also listed. Strictly speaking, these values are for the solid-liquid interface; however, the physicochemical interactions across the interface change little upon solidification of the liquid, allowing the values to be taken as the reversible work to separate the analogous solid-solid interface. (The irreversible work will be discussed in a later section.)

Of particular interest to ice adhesion is the W_A for water on the model substrates. Water interacts strongly with glass (representing portland cement concrete). This leads to the prediction, based only on intermolecular interactions, that the adhesive bond between ice and portland cement concrete should be a strong one. Based on the water-polycarbonate and water-polypropylene works of adhesion, the ice-to-aged asphalt and the ice-to-unaged asphalt adhesive bonds would be expected to be less strong, respectively. Not surprisingly, the lowest interaction is provided by teflon. In fact, as we shall see later, a teflon coating on actual pavement materials reduces the interaction enough to substantially weaken the ice-pavement joint.

In addition to W_A, the surface energy of the substrate alone should also be considered.

Table 6-1 Contact angle cosines on model and reference substrates.

| Substrate | Cosine θ_a* | |
	Water**	Methylene Iodide***
Teflon	-0.38	-0.22
Polypropylene	-0.25	0.44
Polystyrene	-0.03	0.70
Polycarbonate	0.41	0.71
E-glass	0.82	0.50
Steel	0.99	0.95

* Std. devs. are 1-5 % of average values, depending on specimen size.
** Water surface tension = 72.8 dynes/cm.
***Methylene iodide surface tension = 50.8 dynes/cm.

Table 6-2 Work of adhesion values (mJ/m^2) for water and methylene iodide on model and reference substrates.

Substrate	Water	Methylene Iodide
Teflon	45.2	39.6
Silicone*	52.4	66.0
Frekote	(52.4)**	(66.0)
Polypropylene	54.9	72.9
Unaged asphalt	(54.9)	(72.9)
Polystyrene	70.6	86.6
Polycarbonate	103	86.8
Aged asphalt	(103)	(86.8)
E-glass	133	76.2
Portland cement concrete	(133)	(76.2)
Stainless steel	144	99.2

* Computed from contact angle data in ref. 11.
** All values in parentheses are by analogy to values directly above.

One useful empirical method for computing solid surface energy is the liquid pair method (10), based on contact angle values obtained with two different contacting liquids. The equations are,

contacting liquid #1: $W_A/2 = \sqrt{\gamma_L^d \gamma_S^d} + \sqrt{\gamma_L^P \gamma_S^P}$,

contacting liquid #2: $W_A/2 = \sqrt{\gamma_L^d \gamma_S^d} + \sqrt{\gamma_L^P \gamma_S^P}$,

where γ_L^d and γ_L^P are the dispersion (nonpolar) and polar portions of the contacting liquid. The two portions are known and published for a large number of pure liquids (12). Solution of the equations gives the dispersion and polar portions of the solid surface energy, γ_S^d and γ_S^P.

Table 6-3 shows the computed surface energies for the various reference and model substrates, with water and methylene iodide as the contacting liquids. Surface energies of pavement, by analogy to their corresponding model substrates, and of some release coatings, from literature values, are also shown in the table.

Table 6-3 is most useful because it gives an indication of which surfaces are polar and which are not. Thus, the increase in surface energy on going from polypropylene to polycarbonate is due almost entirely to an increase in polarity. By analogy, the same trend should be the case in going from unaged asphalt to aged asphalt. In addition, a large portion of the surface energy of glass is due to polarity. By analogy, the same should be true for portland cement concrete.

The values in Table 6-3 for total surface energy lead to the same predictions for ice-pavement adhesion as did the work of adhesion values. First, the low surface energy of teflon, silicone, and Frekote 33 suggest that coating the pavement with these would promote easy ice removal. Second, the nearly two-fold increase in surface energy from polypropylene to polycarbonate suggests that ice adhesion should increase greatly from unaged asphalt to aged asphalt. Finally, comparison of polycarbonate and E-glass indicates that the adhesion of ice to aged asphalt would be exceeded by that to portland cement concrete.

Table 6-3 Surface energies of solid substrates (mJ/m^2).

Substrate	γ_S^d	γ_S^p	γ_S^{total}
Teflon	6.32	2.32	8.65
Silicone*	19.2	0.65	19.9
Frekote 33	(19.2)	(0.65)	(19.9)
Polypropylene	26.3	0.24	26.5
Unaged asphalt	(26.3)	(0.24)	(26.5)
Polystyrene	35.9	1.05	37.5
Polycarbonate	29.7	13.1	42.8
Aged asphalt	(29.7)	(13.1)	(42.8)
E-glass	16.2	44.3	60.5
Port. cem. conc.	(16.2)	(44.3)	(60.5)
Stainless steel	-	-	-

* Computed from contact angle data in ref. 11.
** All values in parentheses are by analogy to values directly above.

7

X-Ray Photo-Electron Spectroscopy

Analysis of the atom content of pavement surfaces was carried out by Structure Probe, Inc. of Metuchen, New Jersey, on a Perkin-Elmer Model 549-XPS/AES.SAM. Spectra were obtained from four types of surfaces: asphalt region of asphalt concrete, aggregate region of asphalt concrete, sandy mortar region of portland cement concrete, and aggregate region of portland cement concrete. All were from exposed (aged), well-traveled roadways.

The specimens were in the form of small cubes, cut directly from the pavement surface and mounted on specimen holders so that the aged surface was presented to the beam. The specimens were placed in the sample chamber, which was evacuated to 10^{-7} torr prior to obtaining spectra. (Under these high vacuum conditions, the measured atom content is that of a dry surface.) Areas 2 mm in diameter were sampled to a depth of approximately 20 A. A consequence of the non-negligible sampling depth is that the measured atom content includes some subsurface material.

Experimentally measured spectra were compared to standard spectra for the pertinent elements from the Handbook of X-Ray Photoelectron Spectroscopy (13). Empirically derived atomic sensitivity factors from the same handbook were used in atom content determinations. Because atom percents are computed only on the basis of analyzed elements and XPS does not analyze for hydrogen, atom contents cannot be taken as absolute when hydrogen is present in the specimen surface, as it is for asphalt concrete.

The results for atomic composition (atom %) of the surfaces examined are presented in Table 7-1. The aggregate regions for both pavement materials are similar. They both contain silicon and oxygen, as expected for a silicate aggregate. However, they also both show more carbon than expected for a silicate aggregate, carbon that we speculate is due to a hydrocarbon film left by tires.

The sandy mortar region of the portland cement concrete pavement also shows more carbon than would be expected from its bulk composition; this too can be explained by vehicle tire residue. The asphalt region of the asphalt concrete is mainly carbon, as expected from its chemical nature. Rubber tire residue is also undoubtedly present. The surface also shows oxygen, consistent with the infrared data revealing surface oxidation of exposed (aged) asphalt.

When the atom percent values are converted to weight percents, the numerical values for carbon diminish and the mineral character of the aggregate and mortar surfaces is easier to see. The carbon content aside, the mineral character of the aggregate and mortar is similar to that of E-glass (14), the material model for portland cement concrete.

Table 7-1 Atomic compositions of pavement surfaces, atom %.

Atom	Portland Cement Concrete		Asphalt Concrete	
	Mortar	Aggreg.	Asphalt	Aggreg.
C	44.6	56.5	84.0	75.6
N	-	7.4	-	-
O	41.2	23.6	12.9	16.7
Na	1.7	0.8	-	1.7
Mg	-	2.6	-	-
Al	2.6	1.9	-	1.9
Si	8.3	2.5	3.1	2.6
P	-	0.5	-	-
S	-	0.7	-	-
Cl	-	0.3	-	-
Ca	1.6	2.2	-	1.6
Mn	-	1.1	-	-

8

Surface Topography

A rough surface topography is often assumed to be an important element in adhesive bonding. In adhesion, the term "roughness" denotes surface geometry variations on a millimeter and micron scale or smaller. This is the scale of interest to the surface scientist or physicist, and is much smaller than the meter scale of roughness that is often of concern to highway engineers studying vehicle vibration.

It is obvious from a visual inspection of a pavement surface that the true surface area is larger than the projected area of the surface. Consequently there is more ice-pavement interface that must be separated in ice removal than depicted by simple geometry. Furthermore, the special features of the macrotexture and the microtexture may permit types of mechanical interlocking between the ice and the pavement that affect the ease of separation during ice removal.

Surface topography was studied by two methods, profilometry and scanning electron microscopy.These techniques and the results obtained with them are described below.

Profilometry

A profilometer provides a rapid evaluation of surface roughness. As a stylus is moved across the surface, a trace of vertical displacement versus horizontal displacement is produced that represents the surface topography. Since stylus displacement is calibrated in both vertical and horizontal directions, the trace can be used to determine the exact height and distance apart of the various peaks and valleys. From this, some degree of quantification of the roughness can be achieved.

Profilometry traces were obtained for the portland cement concrete surface. The trace in Figure 8-1 is from a slab of portland cement concrete trowelled as flat as possible during fabrication. The height of the irregularities exceeds the 0.05- mm maximum range of the profilometer. It is also clear from Figure 8-1 that the concrete has small scale roughness superimposed on larger scale roughness, i.e., a sort of compound roughness. As a result, the true surface area for this surface sould be expected to be quite a bit higher than the projected surface area.

Profilometry traces could not be obtained for the asphalt concrete because the pressure concentration produced by the stylus as it traversed the surface deformed the asphalt and dislocated small aggregate particles. However, it is probably reasonable to assume that the surface topography of the asphalt concrete is similar in complexity to the portland cement concrete.
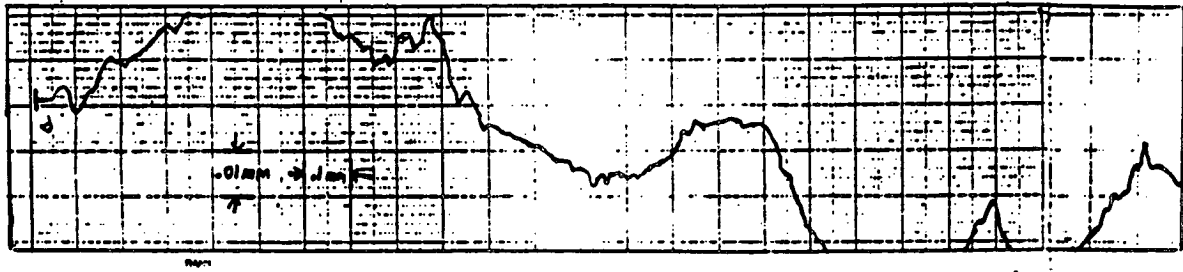
Figure 8-1 Profilometer trace of hand-trowelled sample of portland cement concrete. The large scale roughness varies quite a bit but the small scale roughness superimposed on the longer-range peaks and valley falls within a narrower range, 0.001 to 0.01 mm.

To study the effect of surface roughness on bond formation and adhesive performance, we created well-controlled surface roughness patterns by machining. Since the actual pavement materials did not machine well on a small scale, we used machinable reference materials (steel and polystyrene). For the "zero" level of roughness, we polished the surfaces of the reference materials to a mirror finish. The other levels of roughness were achieved by adjusting the turning speed and cutting depth of a lathe. Figure 8-2 shows the profilometer traces for four different levels of controlled roughness.

Aside from the polished surface, the rough surfaces have a sawtooth pattern, differing only in amplitude and frequency. With simple patterns like these, roughness can be described numerically in terms of amplitude and frequency of the repeating shape. In addition, surface areas can be computed easily, showing that the surface areas of the rough specimens are only up to 15% higher than the area of the smooth, polished surface. This result points out that surface roughness needs to be very complex to provide a substantial increase in surface (or interface) area.

Scanning Electron Microscopy

Scanning electron microscopy, which provides the depth of field necessary to examine a rough surface, was used on both portland cement concrete and asphalt concrete pavement. Fragments of each were mounted on aluminum stubs and vapor-coated with gold to make the surface conductive, thus preventing electron beam charging effects. An AMR-1200 scanning electron microscope was used to scan specimens, which were oriented in the sample chamber so that their edges could be viewed. Each specimen was examined at a series of magnifications from 20X to 5000X. The latter was the highest that the microscope could go and still stay in focus.

Representative micrographs of both asphalt concrete and portland cement concrete pavements at selected magnifications are shown in Figures 8-3 and 8-4. The appearance of the profiles progressing from low to high magnification suggested that the natural pavement surface is a "fractal" surface. That is, the measured profile length becomes longer as the scale used to measure it becomes smaller. This is unlike Euclidean geometries which are "scale invariant." A proof of fractal behavior and determination of the fractal dimension was beyond the scope of this program. However, the possibility that pavement surfaces are fractal surfaces has interesting implications.

Mecholsky et al at Penn State (15,16) found that fracture resistance of certain monolithic materials increases with fractal dimension of the fracture surface. By analogy, the fracture resistance of a joint between ice and a substrate whose surface has a fractal geometry would be higher than between ice and a smooth substrate, provided the locus of failure follows the interface. Thus we would expect it to be harder to remove the ice from rough pavement than from a smooth substrate of the same surface energy as pavement.
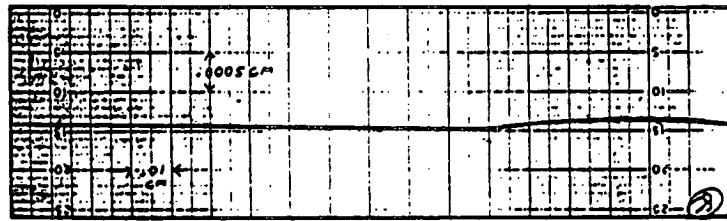
Stainless steel: mirror finish
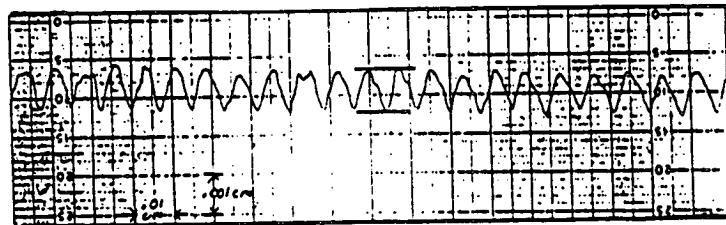
Stainless steel: freq. = 124/cm
ampl. = 0.0010 cm
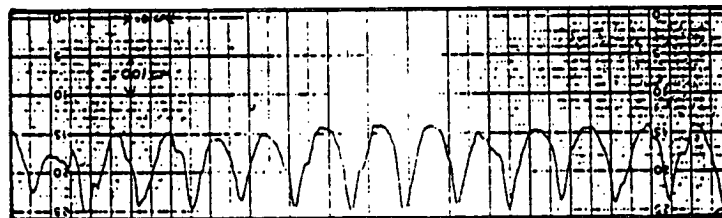
Stainless steel: freq. = 77/cm
ampl. = 0.0020 cm
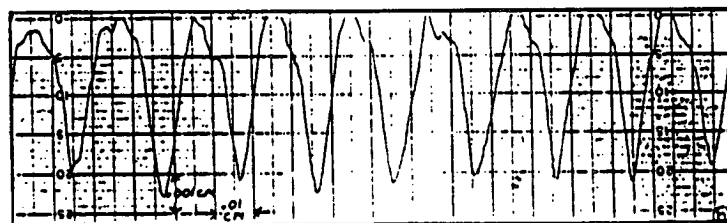
Stainless steel: freq. = 50/cm
ampl. = 0.0044 cm

Figure 8-2 Profilometer Traces of Four Machined Surfaces of varying roughness. Interestingly, the computed surfaces areas of all four are within 15% of each other. This points out that simple roughness does not increase the surface area significantly.
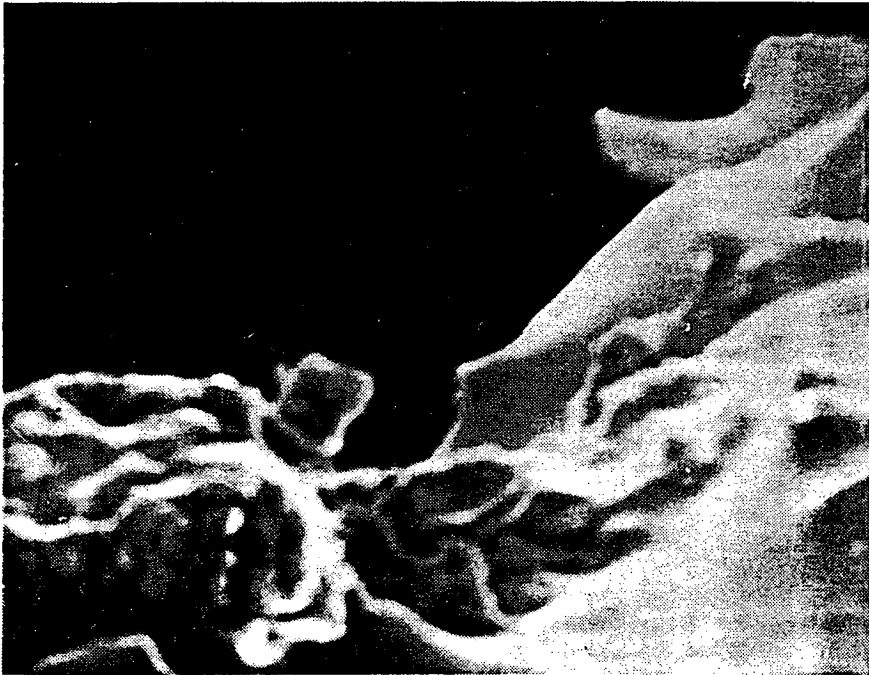
Figure 8-3 Scanning Electron Micrographs of Surface Topography of Asphalt Concrete.
Magnifications are 200X (top) and 1000X (bottom).

Figure 8-4 Scanning Electron Micrographs of Surface Topography of Portland Cement Concrete. Magnifications are 200X (top) and 1000X (bottom).

9

Ice Crystal Characterization

The crystallite size and the presence of flaws or impurities greatly influence the strength of crystalline solids. In ice, such things as bubbles, particulate impurities and crystal boundaries themselves can serve as critical flaws, large enough to cause failure (17-19). It is known that dissolved air leads to the formation of bubbles in ice. If freezing is done slowly, the freezing front will advance slowly, expelling the air ahead of it (19). If the freezing front advances too fast, air expelled from the water as the crystal structure develops will be trapped as bubbles.

The prevalence of flaws in ice is a drawback to the study of ice adhesion, causing the adhesive joint to fail cohesively within the ice rather than adhesively, at the interface. When this happens, the ice-substrate interface is not tested. To gain insight into the cause of cohesive failure, we examined the ice attached directly to the substrate and compared it with the ice farther away.

Experimentally isolating and observing the ice-pavement interface is very difficult when concrete pavement is the substrate. In the vertical direction, the aggregate (stones) distributed throughout the pavement makes it impossible to prepare thin sections perpendicular to the plane of the ice-pavement interface without disrupting the interface itself. In the horizontal direction, the rough surface of pavement makes it impossible to detach in one piece the thin layer of ice immediately adjacent to the pavement surface. Because of these difficulties, special ice-pavement specimens were made where the pavement constituents without the aggregate were used as the substrates. Specimens were also made using reference substrate materials. Examination of ice freezing on reference materials as well as on pavement constituents led to a better understanding of the full range of freezing behavior, and of the position the ice-pavement bond within this range.

Two different specimen configurations were used for the study of ice crystal formation. These were the vertical thin specimen and the horizontal disc specimen. These are both described in detail below, along with results. The vertical thin specimen is shown in Figure 9-1. A 1-2 mm gap between two parallel glass plates defined the specimen thickness. A rubber gasket kept the water contained between the glass plates and in contact with the substrate prior to freezing. Simple asphalt was used to represent asphalt concrete; sandy portland cement mortar was used to represent portland cement concrete; and steel, glass, and polystyrene were used as reference substrates.

These thin specimens provided excellent cross-sectional views of the ice-substrate interface, especially with the aid of a stereo microscope and polarized light. The polarized light delineated individual ice crystals, by virtue of the different color exhibited by each different crystal orientation.

PE release film

Glass plate

Ice
or freezing water

Substrate

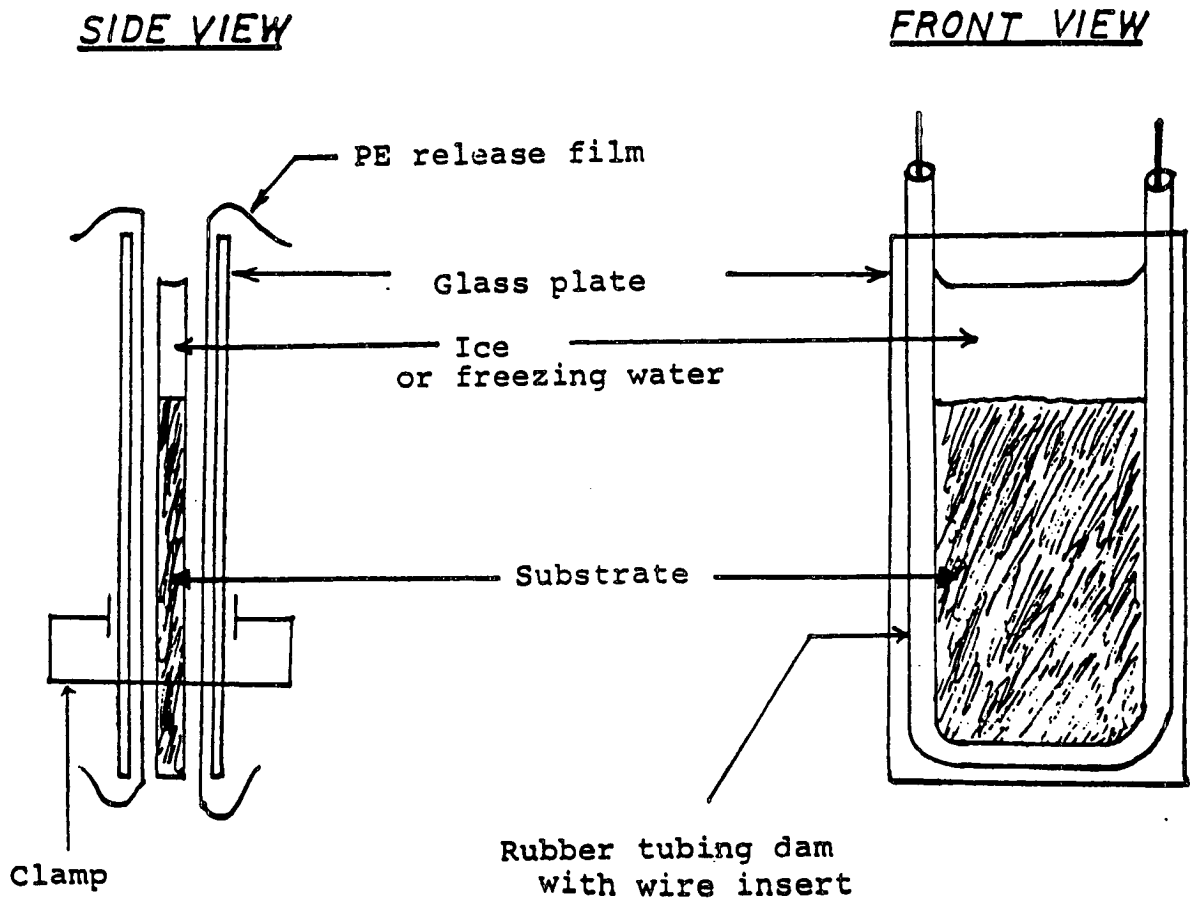Clamp

Rubber tubing dam
with wire insert

Figure 9-1 Vertical Thin Specimen for Observation of Ice Formation. Water is poured on top of the substrate between the two glass plates. Freezing can be observed between crossed polarizers under a microscope with optics tilted upright.

Bottom-up freezing was achieved by adding room temperature tap water to the chilled substrate (temperatures of -10, -20, and -30°C were all used). Top-down freezing was achieved by adding room temperature tap water to the room temperature substrate and them together in surroundings of either -10, -20-, or -30°C to bring on freezing. Formation of ice by accumulation of freezing rain could not be achieved with the vertical thin specimens.

Bottom-up freezing started, as intended, at the substrate surface, by forming a layer of very small, bubble-free crystals. Freezing then proceeded upward, producing large crystals and trapping bubbles throughout. Otherwise, bubbles were well distributed throughout the ice. These crystals were randomly oriented polygons, with "diameters" ranging from approximately 0.5 to 1.0 cm. The small crystals adjacent to the substrate also appeared to be polygonal with two exceptions. These were steel, where the crystals were needles rather than polygons, and polystyrene, where individual crystals couldn't be distinguished due to intense interference fringes that obscured all crystal boundaries. Figure 9-2 shows typical results.

Top-down freezing started, as intended, at the water surface in contact with air and moved downward toward the substrate surface, trapping air bubbles on its way. However, well before the freezing front arrived at the substrate surface, a layer of small bubble-free ice crystals had formed there. (Recall that early nucleation on a substrate surface, before the water remote to the substrate has reached crystallization conditions, was predicted by the computer simulation.) This layer of small crystals remained with no further growth until the top-down freezing front reached it. The result was a junction of two freezing fronts located a few millimeters from the substrate surface. This was observed for all cold room temperatures and for all substrates except polystyrene, where the intense interference fringes obscured the crystal boundaries.

In all other respects, the features of the ice formed in top-down freezing were the same as in the bottom-up freezing (Figure 9-2); the ice crystals not directly attached to the substrates were randomly oriented polygons of typical "diameter" 0.5 to 1.0 cm, and the crystals directly attached to the substrate surfaces were much smaller polygons (or needles, in the case of steel).

The presence of the small, bubble-free crystals attached to the substrate is a significant finding. The layer formed by these crystals can be assumed stronger than the bulk ice, strength being derived from the small size of the crystals and the absence of visible flaws. The presence of such a layer would explain the difficulty in achieving an interfacial locus of failure in studies of ice adhesion. It would also suggest that the adhesion of ice to any substrate is a severe problem, and that ice removal procedures are likely to leave a thin layer of adhered ice behind.

The interference fringes found in the ice surmounting polystyrene are also significant. Interference fringes are an indication of mechanical stress within the ice crystals themselves. We postulate that this stress is based on some kind of thermal mismatch between ice and polystyrene, the last of which has a low thermal conductivity and a high
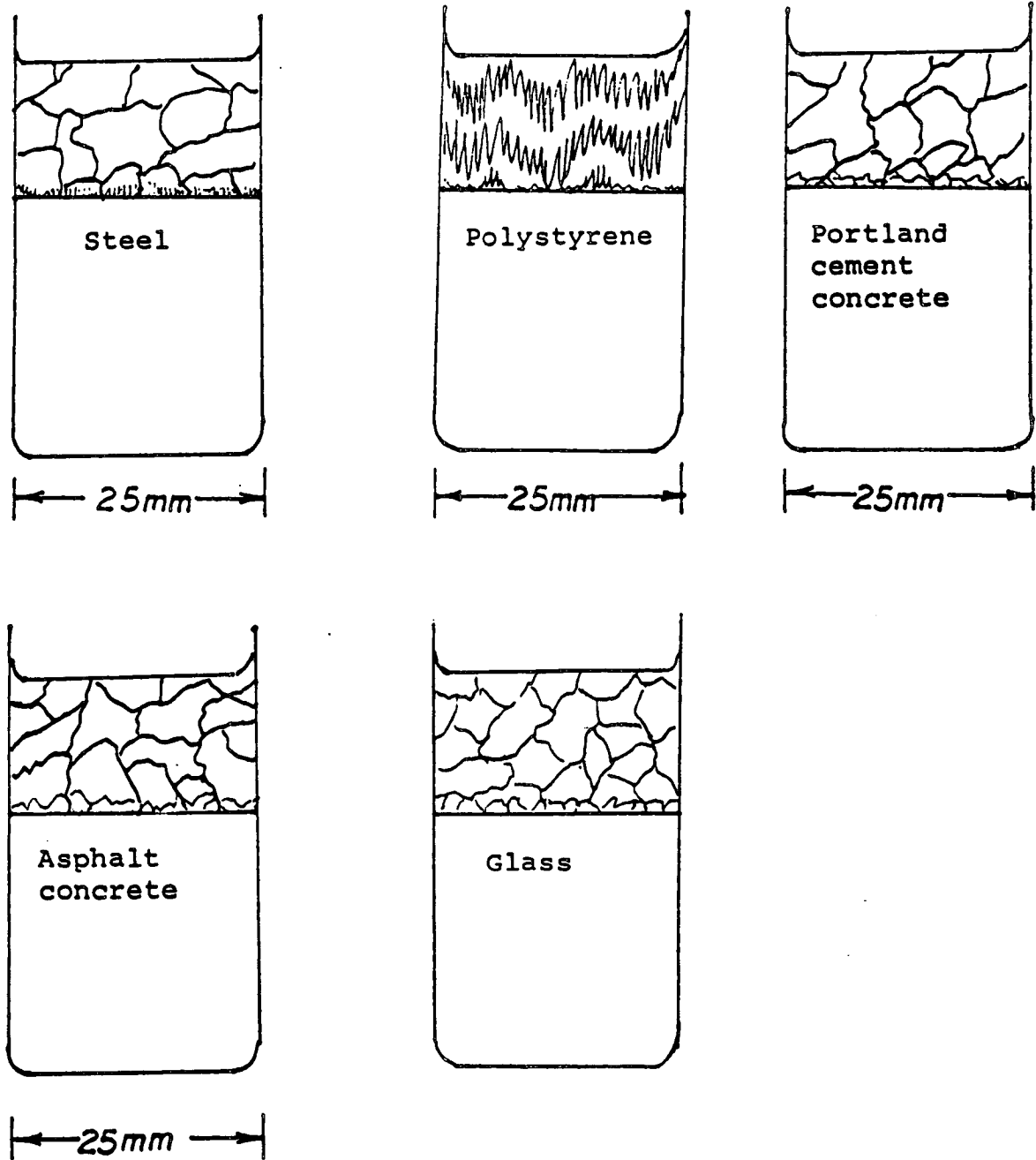
Figure 9-2 Typical Appearance of Ice Crystals Formed on Substrates in Vertical Thin Specimens. Bottom-up freezing gives the above most of the times. Occasionally other behavior is exhibited. The ice pictured is polycrystalline, except for polystyrene, where only interference fringes of stress were seen, perhaps masking crystal boundaries. Small air bubbles, present throughout the ice except adjacent to the substrate and rubber gasket, are not shown in the drawing.

coefficient of thermal expansion. The discovery that a substrate like polystyrene can generate internal stress in ice attached to it is of particular interest because it suggests a means for the reduction of ice-pavement bonding; purposely caused pre-existing internal stress could make it possible to detach ice at lower than usual external load.

The second configuration used to study ice at an interface was the horizontal disc specimen. The ice was present as a thin disc, 1 to 2 mm thick, serving as an adhesive layer to join the butt ends of two right cylinders, as shown in Figure 9-3. Actual pavement could not be machined successfully, and so was not used for this specimen.

Because of their ability to be machined easily, steel and polystyrene were the only substrates used for this part of the research. Their surface energies, though not exact, are not far off from those of portland cement concrete and asphalt concrete, respectively. The butt ends of some cylinders were polished to mirror finishes while others were machined with fine grooves. Water was placed between two matching cylinders and was allowed to freeze (details of procedure are given in the section on strength tests below).

The thin ice discs were detached from the substrates and examined in transmission by polarized light, using a microscope. Detachment was accomplished by thumbnail pressure from the side as the cylinders were slowly warmed by contact heat. Any melting that might have taken place during this process was not perceptible to the naked eye and did not disrupt topographical features that replicated those of the substrate surface. The detachment procedure is interesting in itself for the low amount of mechanical and thermal energy required to achieve separation. The surfaces of the detached discs exactly replicated the substrate surfaces from which they had come. For example, the fine grooves in discs detached from grooved substrates could be clearly seen under the stereo microscope and could also be felt with a delicate pointed probe.

An interesting feature exhibited by all ice discs on both substrates, no matter what the formation conditions, was the presence of a circular plane located approximately midway between each ice-substrate interface. The plane appeared to be flat like a mathematical surface. We concluded from this that the freezing started at each substrate surface and proceeded toward the middle to form a planar junction. There was one layer of crystals above the midplane and one below, their crystal boundaries not in registry (Fig. 9-3).

Steel specimens produced two distinct types of crystals: polygonal and needle-like. Crystals within a given disc were either all polygonal or all needle-like, and never appeared together. Crystal size was extremely uniform within a specimen, but varied widely from specimen to specimen. The "diameters" of the polygonal crystals ranged from 2 to 6 mm from one specimen to the next, and crystal size could not be correlated to ambient freezing temperature or any other specimen preparation condition.
The needle-like crystals were much smaller than the polygonal crystals (Figure 9-4), and were more likely to occur when specimen preparation and freezing was done at higher ambient temperatures. Furthermore, on some specimens the needles appeared to be completely randomly oriented, while on others there were clusters of mutually parallel needles surrounded by randomly oriented needles. On still others the needles were

Visible plane
in ice

TOP VIEW

SIDE VIEW
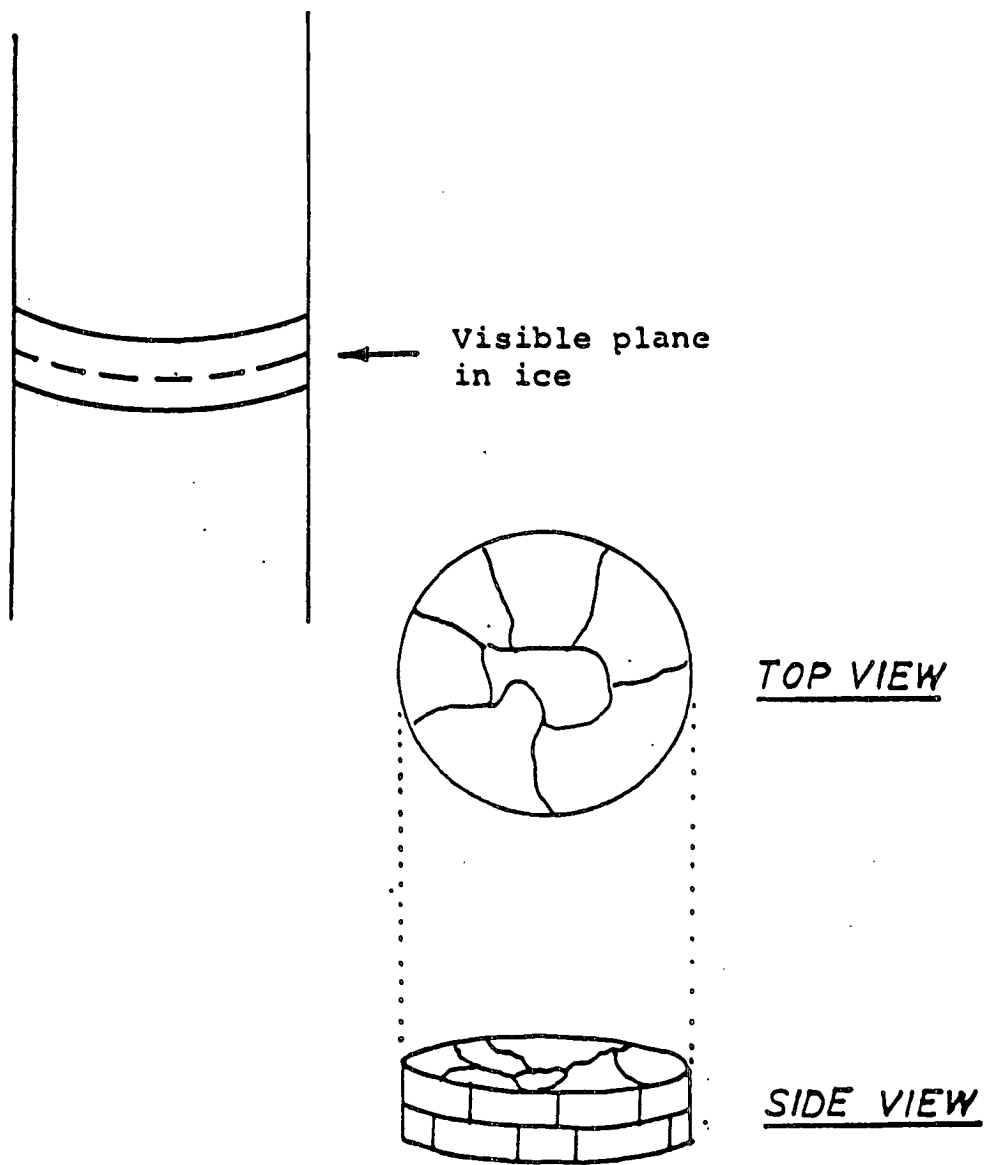
Figure 9-3 Multicrystalline Form of Ice Observed on Steel and on Polystyrene. The disc, which appears clear and transparent, contains two layers of crystals, not in registry with each other. Lateral dimensions of crystals are in the range 2-6 mm.

TOP VIEW

Visible plane
in ice
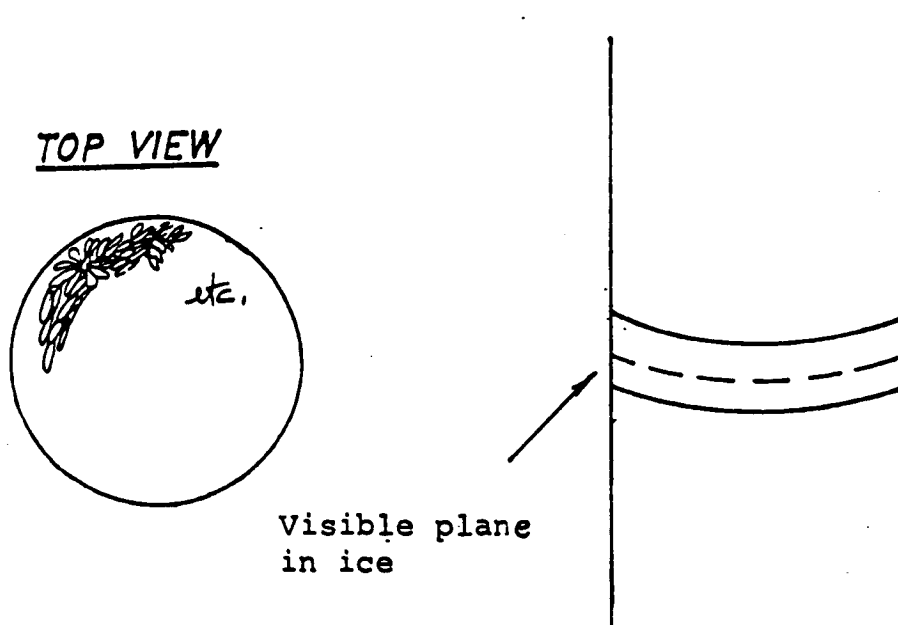
Figure 9-4 Needle-like Crystalline Form of Ice Observed on Steel Substrate. Needle dimensions averaged 0.5 mm by 0.1 mm. The disc, which appears cloudy to the naked eye, contains two layers of needles, one above the dividing plane, and one below. Needles from different discs have varying amounts of mutual parallelism.

overwhelmingly oriented parallel to the machined grooves in the substrate. Needle dimensions were 0.33 to 0.66 mm long by 0.066 to 0.13 mm wide. Unlike the discs composed of polygonal crystals, discs composed of needles appeared cloudy. However, the midplane was clearly visible in these cloudy specimens, with huge numbers of crystals below and above. According to theory, needle formation means that the rate of nucleation was higher than the rate of crystal growth. On the other hand, polygon formation means that growth was faster than crystal nucleation.

Ice discs removed from polystyrene substrate exhibited polygonal crystals only, each disc having an extremely nonuniform crystal size distribution. The boundaries of the polygonal crystals were difficult but not impossible to see under polarized light due to intense interference fringes throughout the whole disc. Apparently, the internal stress did not relax after the discs were detached from the substrate.

The horizontal disc specimens could be mechanically tested prior to detachment of the ice disc from the cylindrical substrates. Measuring the load required to break the assembled specimen into two pieces provided additional information about the role of crystal structure at the interface and beyond. In tensile tests, steel specimens always gave cohesive failure within the ice. Also because the ice crystal size was uniform within a given disc, it was possible to examine the effect of crystal size on failure stress. Specimens with large crystals failed at low stresses, while specimens with small crystals failed at high loads. Figure 9-5 shows this in graphical form, and depicts the crystal size uniformity within a specimen.

Polystyrene specimens gave various loci of failure, including 100% adhesive, 100% cohesive, and combinations of the two (designated "mixed"). Failure stresses tended to be wide ranging, but on the whole much lower than for steel specimens, many specimens failing during gentle handling prior to test. Figure 9-6 illustrates the nonuniform crystal size distribution and the resulting variation in failure loci and failure stress levels. These non-uniform crystal sizes within a specimen precluded examination of a size-to-strength relation.

In sum, there are five important conclusions from the ice disc specimens. First, the nature of the substrate itself determines the size and shape of the crystals that nucleate and grow directly on it; the temperature of the surroundings appears to have relatively little influence by comparison. Second, a junction of freezing fronts remote from the ice-substrate interface will be both a plane of discontinuity and the locus of failure. Third, when crystal size is uniform within a specimen, the mechanical load required for cohesive failure (in the ice) is inversely related to crystal size. Fourth, when the ice is composed of nonuniformly sized crystals, both the failure locus and the failure load will be unpredictable. Fifth and finally, is the observed detachment of ice from a substrate by small pressure and small but controlled heat. This is of the greatest practical importance because it demonstrates that only small amounts of thermal and mechanical energy, when combined and focused properly, are necessary to debond ice.

66
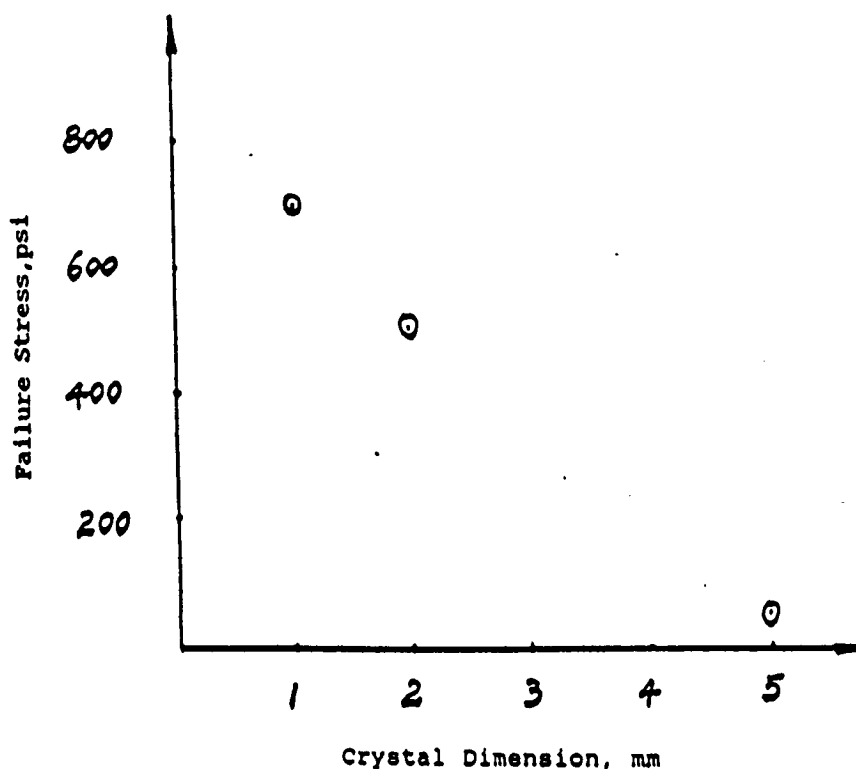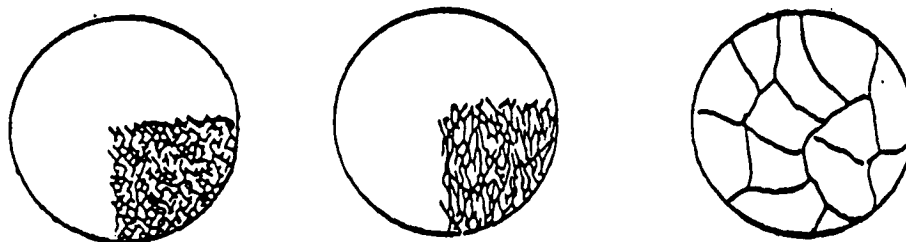
Figure 9-5 Relation of Cohesive Failure Stress in Ice to Crystal Dimension. For ice-steel butt tensile specimens, which always failed cohesively in the ice, failure stress was inversely correlated to the characteristic dimension of the polygonal ice crystals. AT top are line drawings of ice discs removed from tested specimens, showing crystal size variation from disc to disc, but uniformity within the disc.

281.7 psi
100% Cohesive
Failure
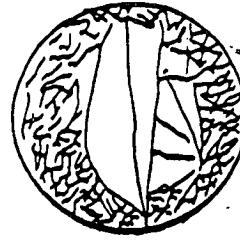
5.1 psi
100% Cohesive
Failure
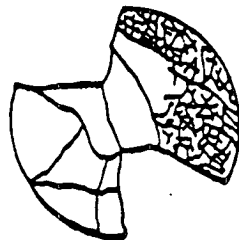
3.20 psi
95% Adhesive
Failure

1.9 psi
100% Cohesive
Failure
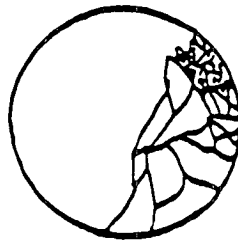
0.00 psi
100% Adhesive
Failure
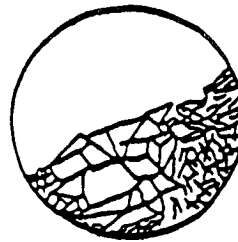
0.0 psi
100% Adhesive
Failure

Diameter = 1 in.

Figure 9-6 Drawings of Ice Discs from Tested Ice-Polystyrene Butt Tensile Specimens. Discs or fragments thereof were difficult to remove from the substrate for examination and often fragmented during removal. Note that all discs contain both small and large crystals.

10

Fracture Energy

There are two key goals to meet when mechanical tests are used to study the adhesion between two dissimilar materials. The first is to extract a materials parameter value, independent of geometry, from the mechanical test results. The second is to achieve failure at the interface between the two materials so that conclusions can be drawn about adhesion rather than cohesion.

The first requirement can usually be met by choosing the appropriate test, that is, one designed especially for determination of a materials parameter. As discussed in the background section of this paper, many of the longstanding joint strength tests (butt tensile, lap shear, etc.) do not yield a materials parameter. Fortunately, in tests that are interpreted by fracture mechanics analysis, the details of the specimen geometry, the stress distribution in the specimen, and the elastic properties of the two adhering materials are taken into account explicitly. Therefore the desired materials system parameter, one that pertains to the interfacial adhesion alone, can be extracted from the test results. The materials parameter is designated interfacial fracture energy, and is defined as the energy required to separate unit area of interface. Tests developed for the determination of interfacial fracture energy values in bimaterials systems include the double cantilever beam test (20) and the blister test (21-23).

The second requirement in studying adhesion, that of achieving failure strictly at the interface, can be extremely difficult to meet with some adhesive systems. This difficulty often arises when a substance adheres well, but has flaws in its own bulk or has a relatively low bulk strength. As we have already seen, ice adheres well to most surfaces, but is brittle and fragile itself due to flaws and bubbles generated during freezing. Attempts to separate ice from a substrate result in cohesive fracture of the ice itself, making a meaningful study of ice adhesion very difficult.

As mentioned earlier, many of the studies on ice adhesion reported in the literature involved cohesive failure within the ice. No studies at all determined a materials parameter, independently indicative of ice's adhesion to a substrate. To achieve the two goals of obtaining a materials parameter and achieving interfacial failure, we selected the blister test. Besides lending itself to fracture mechanics analysis, the blister test appeared to offer specimen preparation advantages. Water, as a low viscosity adhesive, could be applied directly to a pavement substrate with no elaborate molding, cutting or gripping required.

The blister test configuration originally tried in our work is shown in Figure 10-1. In this configuration, a circular nonbonded area is present in the central region of the adhesive-substrate interface. Pressurization of the inside of the specimen deflects the nonbonded portion of the adhesive layer vertically like a blister. (The deflection is exaggerated for
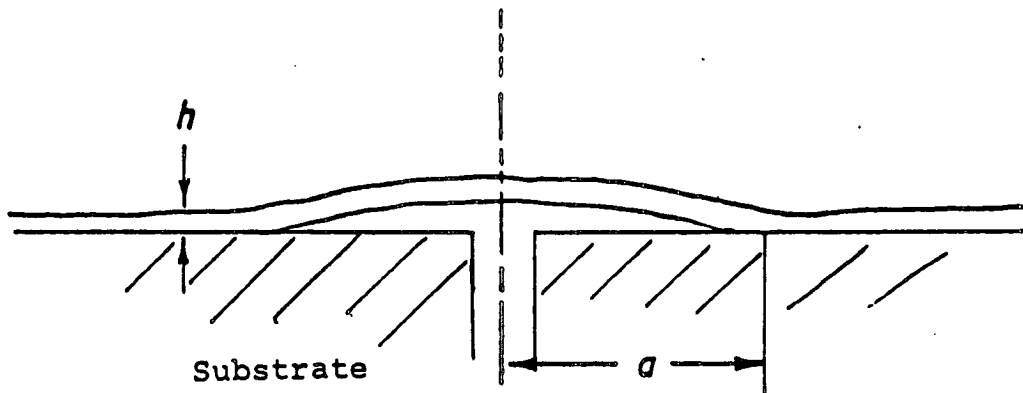
Figure 10-1 Blister Test Specimen Configuration. The ice layer of thickness h, is bonded to the substrate except for circular crack at center of radius in the center of the specimen. Actually ice lies flat, but is shown lifted here for clarity. The initial crack, a, propagates at the interface when interior of blister is pressurized with inert gas.

70

emphasis in Figure 10-1). When the applied pressure becomes high enough, the pre-existing nonbonded area enlarges radially. The radial enlargement is intended to be accomplished by crack propagation at the interface. Because of the particular geometry of the blister test, unstable rather than stable crack propagation occurs, so that failure is catastrophic and only one failure pressure measurement can be made per specimen.

The interfacial fracture energy, F, is computed from an energy balance equation that explicitly contains the measured failure pressure P_c, details of specimen geometry, and the elastic properties of the deforming material in the specimen. The high thickness of the substrate precludes its deformation during the pressurization process; thus it is not part of the energy storage and release process and its elastic properties do not affect the values obtained for P_c. However, the adhesive layer on top deforms and stores energy during pressurization, and knowledge of its elastic properties is needed for the analysis.

Clearly, the ability to compute a materials parameter value that is not only independent of geometry and elastic properties, but also pertains only to the interface, means that a valid comparison of ice adhesion to a variety of substrates can be made.

Fracture Testing on Pavement

An important strategy in our study of ice-pavement adhesion was to preserve the pavement's complex surface topography while varying the surface energy. To do this, we applied different thin coatings to the pavement surface. The reason for such a stategy relates to the fact that in practice, coatings could be applied to pavement to reduce ice adhesion.

Blister test experiments were conducted using both asphalt and portland cement concrete pavement slabs as substrates. The coatings were spray-applied to give full coverage of the surface while not obscuring or modifying the detailed topography of the pavement. The asphalt concrete was obtained from pavement slabs in the New York City area while the portland cement concrete was in the form of slabs made in our laboratory.

Because the means by which ice is formed on the pavement may be an important factor, our study included three different freezing modes: bottom-up, top-down, and freezing rain. The first two were achieved by the freezing of pooled water where the freezing direction was controlled by the relative temperature of the air and the pavement surface. The freezing rain was achieved by spraying droplets of cold water onto the cold substrate until the droplets accumulated to the desired depth. Auxiliary tests indicated that there was no detectable difference in the bond strength when distilled water was used instead of tap water; therefore tap water was used.

Work was done at an ambient temperature of -20°C (i.e., initial pavement surface temperature and surrounding air temperature were -20°C, and testing was carried out at -20°C). Three types of failure were observed while conducting the blister test:

completely adhesive, completely cohesive, and a mixture of adhesive and cohesive. A simplifying rule was used to assign the mixed failures to either the adhesive or the cohesive category. If the failure was adhesive in the 6.35-mm region immediately adjacent to the central debond radius, the failure was defined as adhesive.

The relative numbers of adhesive and cohesive failures for the three freezing modes (top-down, bottom-up, and freezing rain) were noted. Figure 10-2 summarizes these observations in bar graph form. The surface coatings are arranged in order of increasing surface energy from left to right. The only observation that applied to both pavement substrates was that coatings with very low surface energies, such as teflon and silicone, gave overwhelmingly adhesive failures for all freezing modes. Obviously, these very low energy nonstick agents such as teflon and silicone did indeed weaken the ice-pavement bonding sufficiently to allow an interfacial separation. Other than this, neither surface energy nor freezing mode seemed to make a great deal of difference.
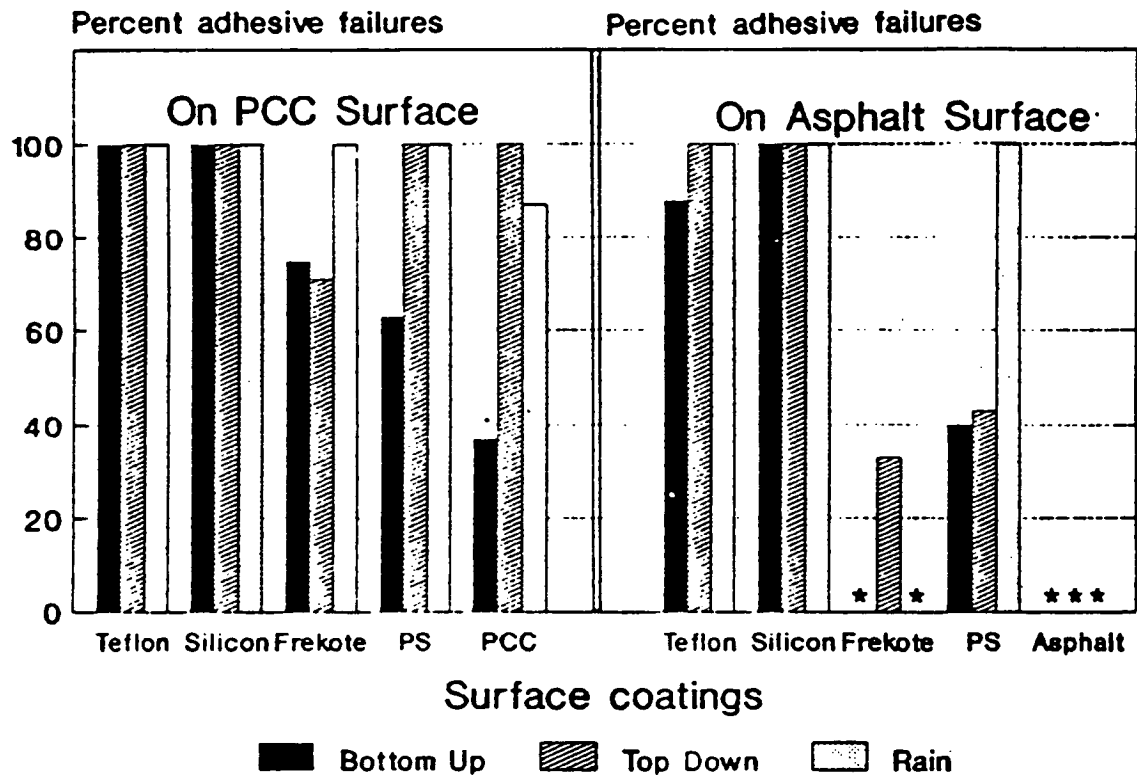
Figures 10-3 and 10-4 show average failure pressure values for those failures that were adhesive (at the interface). The main observation was that the asphalt and portland cement concrete performed differently in ice adhesion even when coated with the same material. For all freezing modes on asphalt concrete, failure pressure showed no clear sensitivity to surface energy. The failure pressures were converted to fracture energy (F) values using the following equation (23):

$$ P_c = \frac{\sqrt{2\pi}}{3} \cdot \frac{\sqrt{EF}}{c} , $$

where E = elastic modulus of the ice, "c" is the initial debond radius, and P_c is the specimen failure pressure. The equation applies to a thick incompressible adhesive (ice) bonded to a rigid substrate (pavement).

The computed interfacial fracture energies are shown in Table 10-1. Also shown for comparison are the work of adhesion (W_A) values for water contacting the smooth analogues of each surface coating used. These values, obtained from contact angle measurements, give a measure of the intermolecular attraction between the water and the surface it contacts. The work of adhesion is the work to separate two materials in a thermodynamically reversible process. Interfacial fracture energy is comprised of both reversible and irreversible contributions. The reversible contribution is equivalent to the work of adhesion and the irreversible contribution includes all irreversible processes such as microcracking, sound emission, creep of the materials near the interface (24, 25).

Because of the energy dissipation involved in the irreversible processes, we would expect the interfacial fracture energy for a given interface to be larger than the reversible contribution (W_A) alone. Because not all the experimental data in Table 10-1 followed this principle, we suspected that the blister test conducted as described was not valid. A number of factors may have interfered with the ability of this test configuration give a reasonable value of interfacial fracture energy. First, the failures we designated adhesive

Figure 10-2 Percentage of Adhesive Failures Achieved for PCC and Asphalt Specimens. Surface coatings are positioned on graph in order of increasing surface energy.

Top-Down Mode
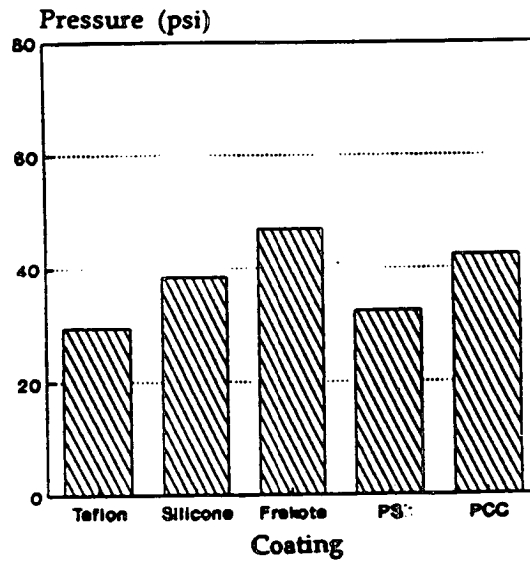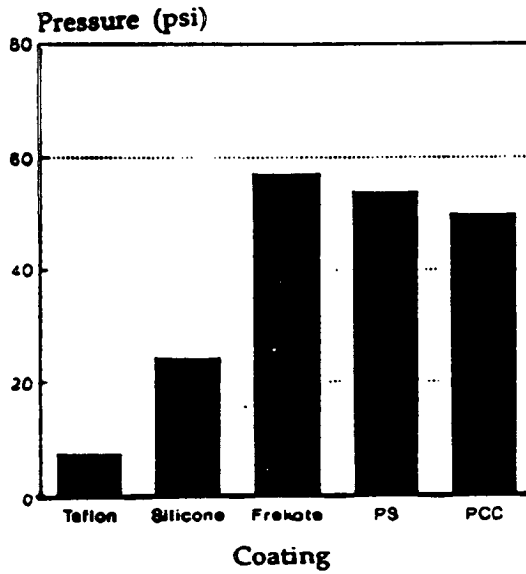
Bottom-Up Mode　　　　　　　　　　　　　**Rain Mode**
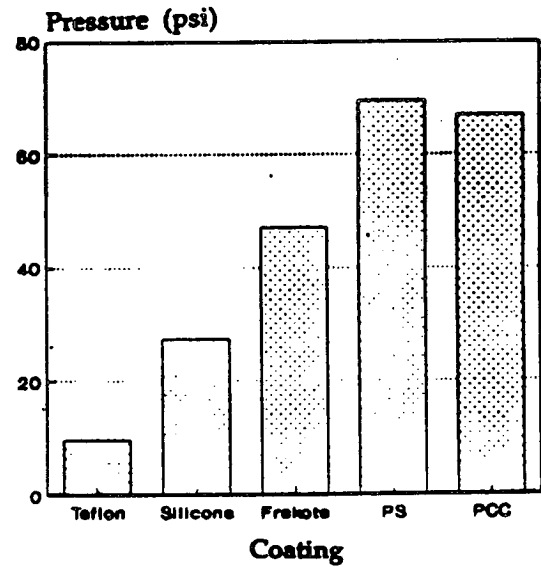
Figure 10-3 Relationships Between Mean Adhesive Failure Pressure and Coatings on PCC specimens for Three Freezing Modes. Coatings increase in surface energy left to right.

Pressure (psi)
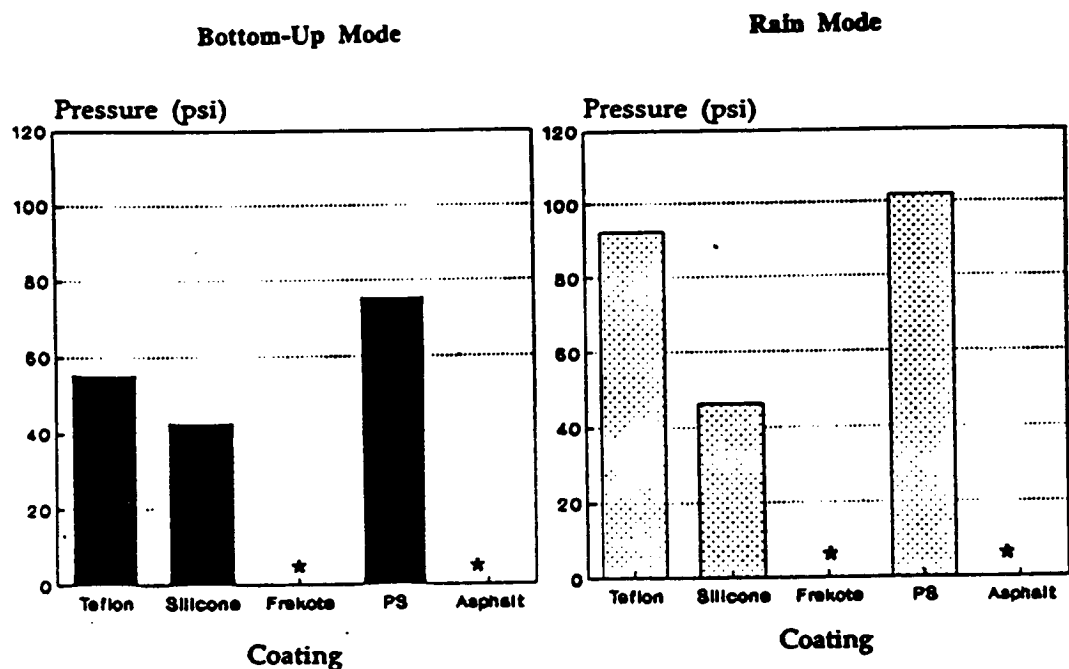
Pressure (psi)

* No adhesive failures (all cohesive)

Top-Down Mode
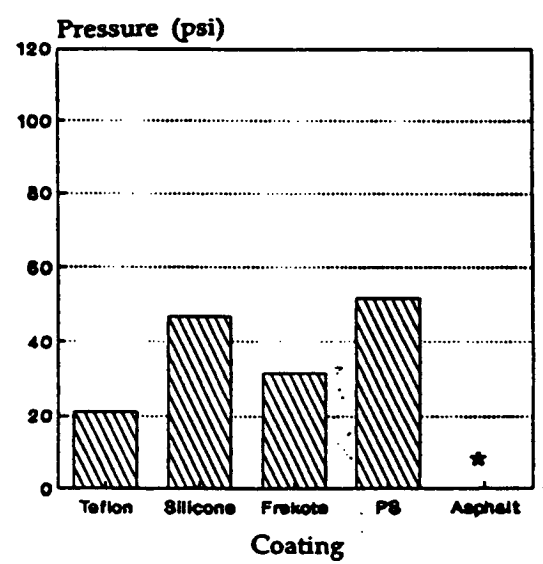
Pressure (psi)

Figure 10-4 Relationship Between Mean Adhesive Failure Pressure and Surface
Coatings on Asphalt Concrete Specimens for Three Freezing Modes. Coatings increase
in surface energy left to right.

Table 10-1 "Interfacial" fracture energies for ice on coated pavement, mJ/m^2 (ave. ± std. error mean).

Portland Cement Concrete

Coating (W$_A$)	Top-down	Bottom-up	Freezing Rain
Teflon (45.2)	47.1 ± 28.9	3.6 ± 0.8	5.2 ± 1.4
Silicone (52.4)	80.7 ± 24.7	33.0 ± 11.5	41.2 ± 19.2
Frekote (52.4)	121 ± 12.3	179 ± 27.5	121 ± 3.1
Polystyrene (70.6)	57.5 ± 12.0	160 ± 26.0	263 ± 40.1
None (133)	97.5 ± 18.4	136 ± 15.8	245 ± 29.2

Asphalt Concrete

Coating (W$_A$)	Top-down	Bottom-up	Freezing Rain
Teflon (45.2)	4.2 ± 10.1	167 ± 70.6	463 ± 112
Silicone (52.4)	120 ± 44.0	99.3 ± 30.2	117 ± 23.7
Frekote (52.4)	54.4 ± 9.6	All cohesive	All cohesive
Polystyrene (70.6)	147 ± 40.8	311 ± 73.2	567 ± 83.3
None (103)	All cohesive	All cohesive	All cohesive

may not have been. Second, the interface may have been flawed by air bubbles trapped in topographical features of the rough surface. Third, the coatings applied to the rough pavement surfaces may not have been as coherent as assumed. Any of these factors could have allowed low failure pressures values into consideration that should have been discarded.

Fracture Testing on Model and Reference Substrates

The fact that some of the interfacial fracture energies were physically unreasonable, plus the fact that no trend as a function of surface energy was observed, led us to design a more controlled fracture test for the unambiguous evaluation of ice adhesion.

In essence, we turned the test geometry upside-down and substituted model and reference materials for pavement slabs. Figure 10-5 shows the inverted configuration. A thick aluminum base served as a supporting structure; its properties did not enter into the computation of interfacial fracture energy. Covering the base was a thin layer of ice serving as the adhesive. The ice was surmounted by a thin layer of the "substrate" of interest. A cylindrical, centrally located hole passed through the base and the ice (but not the substrate) for pressurization of the specimen. In preparing the specimen, water was simply poured onto the base, the substrate was placed on top of this, and the whole assembly was put in the cold room for freezing. Smooth sheets of substrate materials having works of adhesion with water ranging from 45 to 144 mJ/m^2 were used as substrate layers.

Figure 10-6 compares results obtained from the standard blister test with those obtained from the inverted blister test. As hoped, the scatter was much reduced in the inverted blister test data. This is because the ice thickness could be controlled to uniform selected values and flaws in the form of bubbles in the ice could be eliminated. Close examination of the crack tip in the inverted configuration showed that it was clean, sharp, and reproducible, unlike the earlier version. The equation (26, 27) that applies to the inverted geometry expresses failure pressure P_c in terms of elastic properties and geometry:

$$P_c = \sqrt{\frac{2EF}{c(1-v^2)} \left\{ \frac{3}{32} \left[\left(\frac{c}{h}\right)^3 + \left(\frac{c}{h}\right) \frac{4}{1-v} \right] \frac{2}{\pi} \right\}^{-1}},$$

where E = Young's modulus of substrate,
        c = radius of initial crack
        v = Poisson's ratio of substrate,
        h = thickness of substrate, and
        F = interfacial fracture energy.

Note that properties of the ice layer are not included in this equation since the ice is
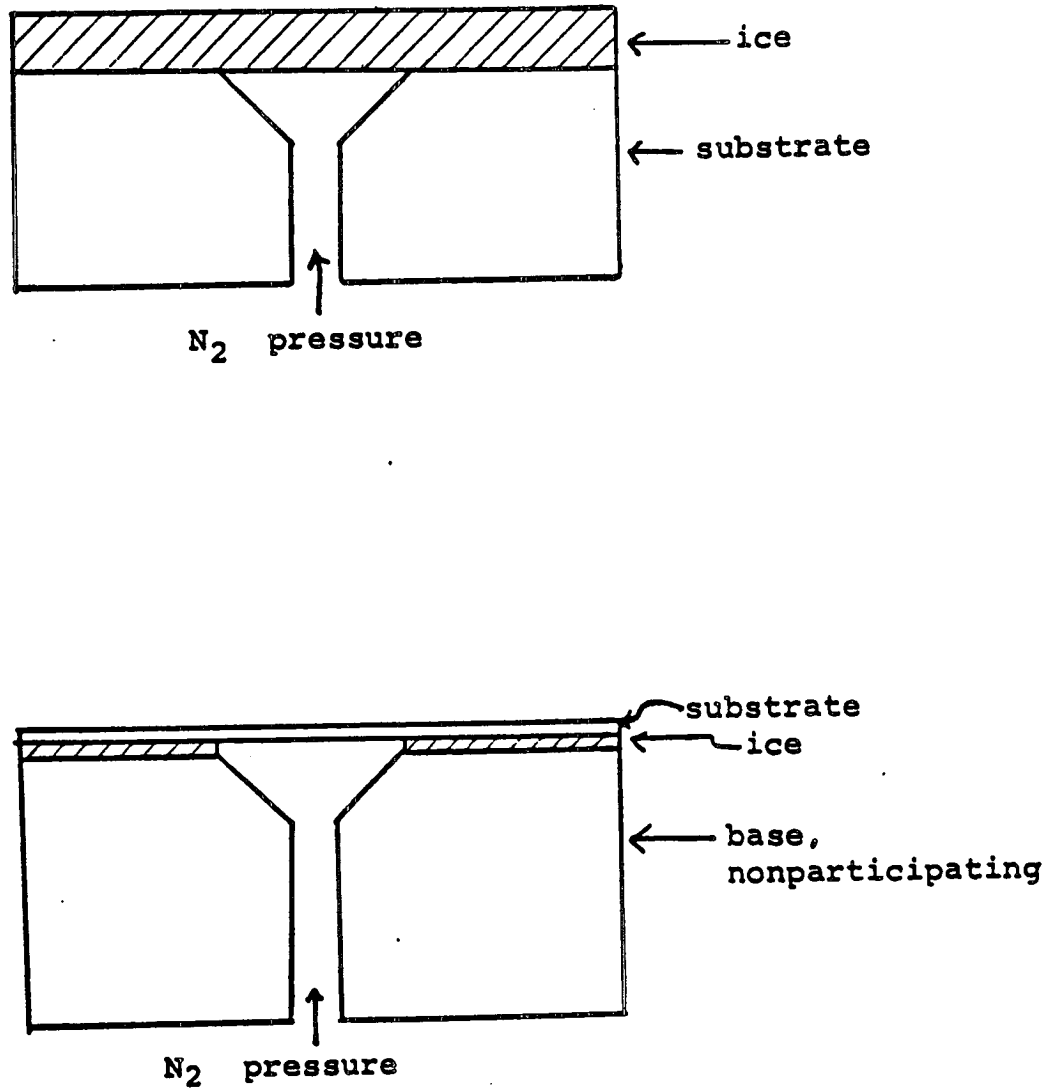
Figure 10-5 Standard versus Inverted Blister Test. In the inverted configuration (bottom) the details of the crack tip, the ice thickness, and the flaws in the ice are controllable and reproducible, reducing the scatter caused by these factors in the standard configuration (top).
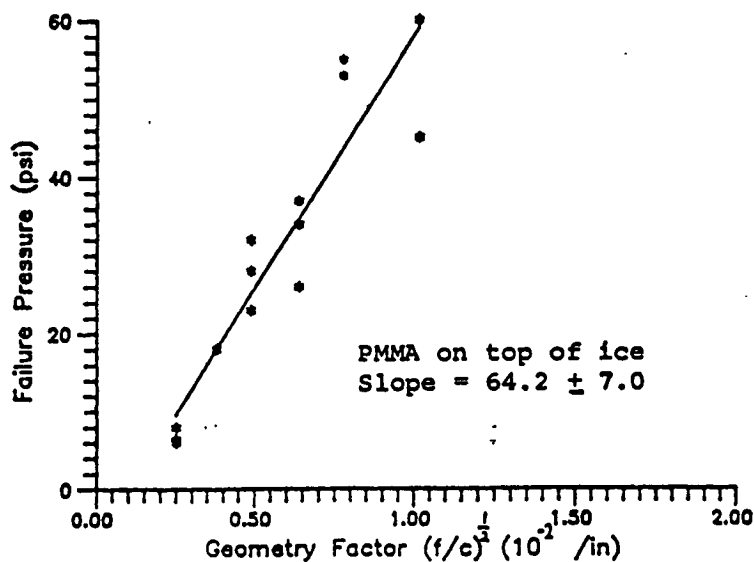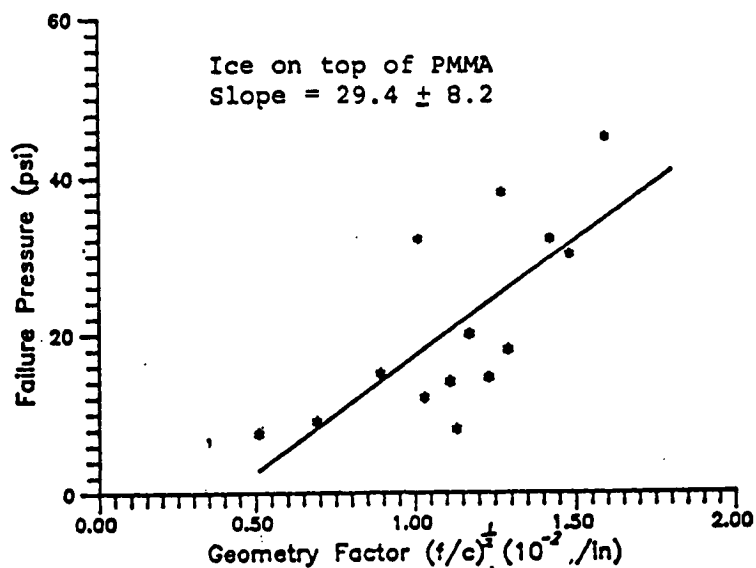
Figure 10-6 Comparison of Results form Standard Blister Test (Top) with Those from Inverted Blister Test (Bottom). Results are in the form of failure pressure Pc versus geometry factor. Fracture energy is determined from slope. Scatter for the inverted test is much lower, allowing a slope to be determined form the plot with confidence.

present as a thin stiff layer that, in the inverted geometry as opposed to the standard geometry, does not store energy. It is the substrate, and not the ice, that is deformed during the test and therefore contributes the energy for the crack propagation. The modulus values necessary for use in the equation for substrates were obtained by separate experiments conducted at -20°C. Table 10-2 shows the results obtained for the debonding of various substrates from ice. All failures were interfacial, again in contrast to the results from the standard blister test configuration. The values for interfacial fracture energy for ice on smooth surfaces are all equal or larger that than the work of adhesion values; thus they are physically reasonable and confirm the validity of the inverted blister test.

Figure 10-7 shows a plot of the data, with the best fit curve drawn in. The curve shows that the interfacial fracture energy to separate ice and a given substrate is a strong nonlinear function of the work of adhesion of the substrate with water. We feel that this finding is one of the most important of this entire research program.

The notion illustrated by Figure 10-7, that the irreversible contribution to interfacial adhesion is a function of the reversible contribution, and that they are not strictly complementary has been suggested by Andrews and Kinloch (20) but seems to have gone unnoticed.

Figure 10-7 also explains much of the difficulty experienced by past workers in achieving separation of ice from a substrate at the interface. Erroneous assumptions of a linear relation between work of adhesion (surface energy) and fracture energy always led to the erroneous expectation that separation of ice from high energy surfaces should require only a little more energy than separation from low energy surfaces. This obviously is not true, and along with the presence of flaws in bulk ice, explains the prevalence of cohesive failures in the ice.

For removal of ice from pavement surfaces, the results in Figure 10-7 are bad news. Because the surface energies of portland cement concrete and aged asphalt concrete are fairly high, the irreversible contribution to interfacial fracture energy would be high, corresponding to large amounts of mechanical energy required to remove ice.

80

Table 10-2 Inverted blister test results at -20°C.

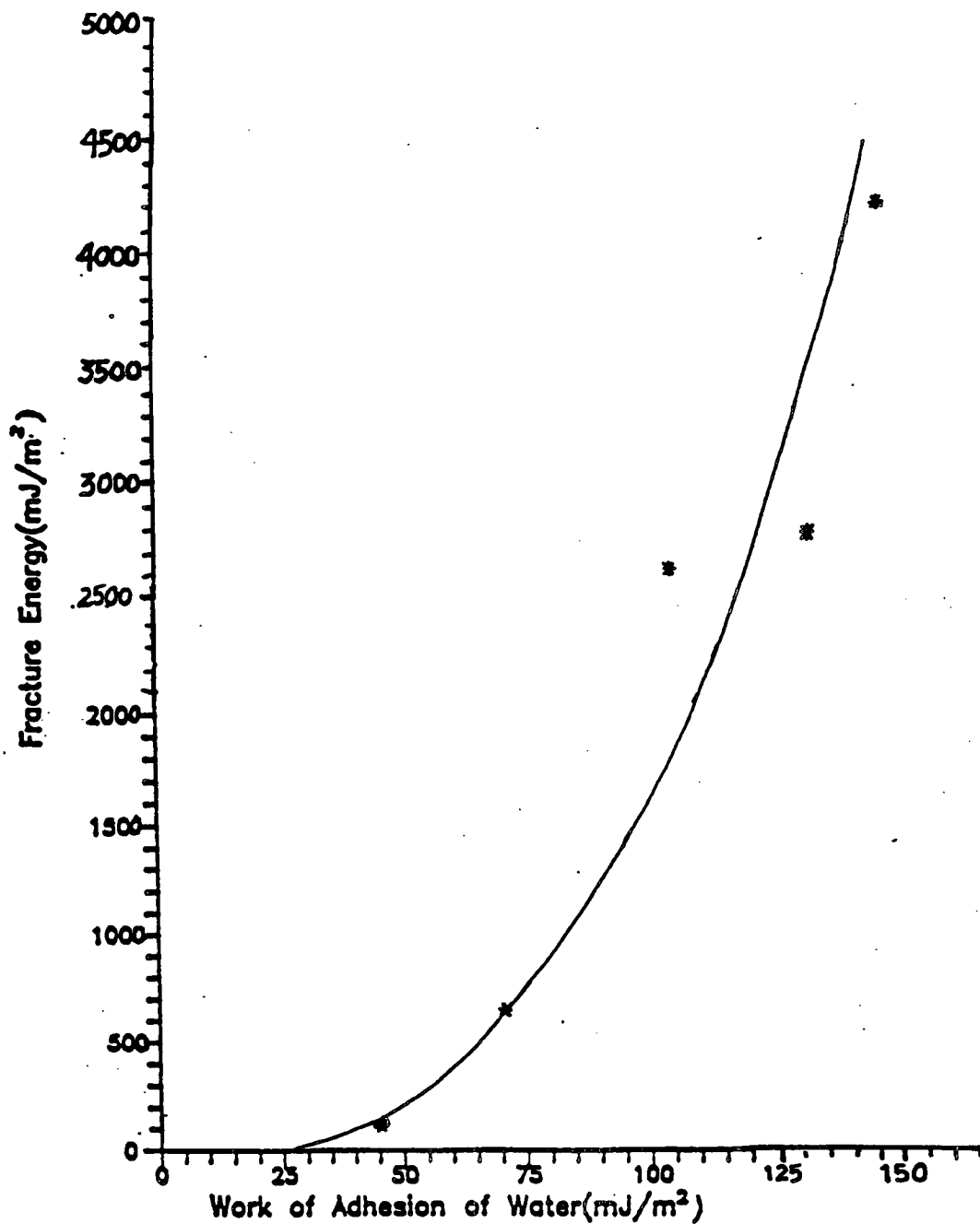| Substrate	Modulus, GPa	W_A with Water, mJ/m^2	Interfacial Fracture Energy, mJ/m^2
Teflon	1.32 ± 0.14	45.2	114
Polystyrene	1.30 ± 0.07	70.6	683
Polycarb.	1.43 ± 0.12	103	2640
PMMA	1.77 ± 0.24	132	2810
Stainless	33.4 ± 4.0	144	4220

Figure 10-7 Interfacial Fracture Energy as a Function of Work of Adhesion of Water on Substrate. The plot shows that the interfacial fracture energy F, determined from the blister test, increases nonlinearly with work of adhesion. Substrates used were Teflon, polystyrene, polycarbonate and stainless steel, all smooth.

11

Strength Tests on Adhesive Joints

The inverted blister test described in the previous section made it possible to determine the interfacial fracture energy for ice adhered to a variety of different substrates. In this section, results from traditional adhesive joint tests are described. Traditional tests have the advantage of simple geometry and relatively small size; both are important features when large numbers of test specimens must be prepared. While traditional tests do not give a materials parameter and thus cannot be used to compare one ice-substrate interface with another, they can be used to evaluate a single ice-substrate interface under different conditions. The conditions, or variables, of interest in this study were substrate surface roughness, conditioning temperature, test temperature, and testing rate. It is reasonable to expect that any or all of these variables could affect both joint strength and failure mode.

In a traditional joint strength test, the applied load at which the specimen breaks into two pieces is noted. This load, P, is normalized by dividing it by the cross-sectional area, A, of the interface in order to express joint strength in terms of failure stress. Tensile loading produces normal stress, which is accompanied by volumetric expansion of the materials as they deform, while shear loading produces isovolumetric deformation. In the work described in this report, two types of joint strength configurations were used: one to load the ice-substrate interface in tension, and the other to load the interface in shear.

For an investigation of joint strength as a function of multiple variables, each varying widely, it is essential to prepare numerous specimens that are exact replicates of one another. Small specimens of asphalt or portland cement concrete are not only difficult to form in reproducible fashion, but exhibit high individual variation. This makes them completely unsuitable for a detailed laboratory investigation of the effect of test rate, test and conditioning temperatures, and surface roughness.

Therefore polystyrene and steel were used instead of pavement as substrate materials for the tensile and shear strength studies. Not only can replicate specimens be easily machined from these materials, but they readily survive handling and repeated testing. The surface energies of these two reference materials are not exactly equal, but are close enough, to those of asphalt and portland cement concrete to be highly relevant.

Tensile Testing

The tensile specimen used for the ice-steel joint is shown in Figure 11-1. Simple in concept, it was easy to assemble during specimen preparation. The plastic ring was
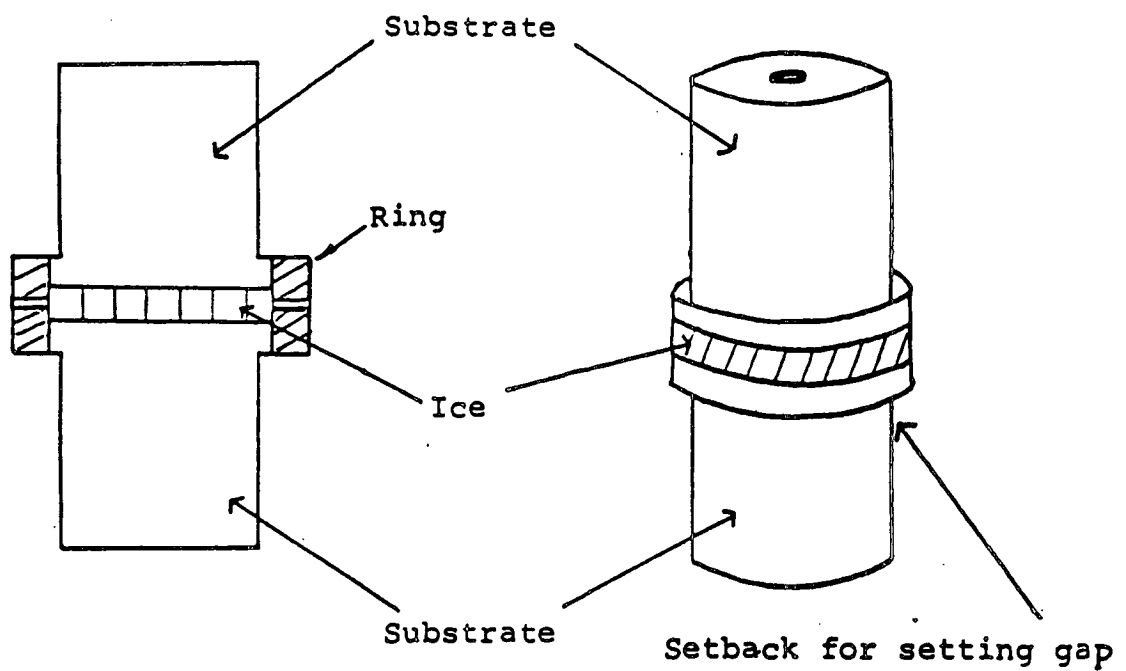
Figure 11-1 Tensile adhesive joint specimen for steel substrate. Water is injected (through hole in ring) into gap between the two steel cylinders. The ring seals water in during freezing (left) and is removed before testing (right).

removed from the frozen specimen just prior to test. This specimen could not be used for the ice-polystyrene joint because of the uneven freezing of the ice attached to polystyrene (discussed later). The specimen developed for ice-polystyrene after considerable experimentation is shown in Figure 11-2. The extreme ends of all specimens contained threaded holes into which eyelets could be screwed to apply external load.

Test temperature was varied between -10° and -40°C, the upper limit set to be near but below the freezing temperature of water and the lower limit set by the capability of the laboratory cooling equipment. Test rate was varied between 1.02 mm/min and 10.2 mm/min, as per the limits of the test equipment.

Surface roughness of the substrate was varied in a controlled way by machining a sawtooth groove in a helical pattern into the cross-sectional faces of the substrate cylinders. Three different amplitude and frequency combinations (Table 11-1) as well as a mirror polished surface were used to give a total of four levels of roughness. Interestingly, the surface area difference from mirror smooth to most rough was only about 17%. All specimens were assembled using cylinders of matching roughness; no mixed pairs were tested.

The variable defined by us as conditioning temperature was used to replace the "freezing temperature" requested by the sponsor. Originally the sponsor asked that "freezing temperature" be made to take values in the range 0°C to -40°C. As discussed in a previous section of this report, freezing of water always takes place very close to 0°C, usually within 1°C of zero, no matter what the temperature of the surrounding environment. Colder surroundings simply facilitate heat removal from the water and enable it to reach zero sooner. Hence we have not used freezing temperature as one of the controllable variables in this study.

We have instead defined "conditioning temperature," the temperature at which a frozen specimen was held for several hours after freezing and before testing. This temperature could be controlled as well as selected. We found that some residence time at a temperature below zero was absolutely necessary; both polystyrene and steel specimens handled immediately after freezing broke readily and could not even be tested. Therefore specimens were held at the selected conditioning temperature for 12 hours prior to test.

Testing itself was conducted on an Instron universal test machine whose throat was fitted with an insulated, temperature-controlled test chamber. Specimens were held inside the test chamber long enough prior to load application to reach thermal equilibrium with the chamber. This was usually under an hour.

The tensile test data were analyzed using a multi-variable linear regression program. The four basic independent variables were conditioning temperature (x_1), testing temperature (x_2), test rate (x_3), and substrate roughness (x_4); the dependent variable was failure stress (y). Each of the independent variables was tried in both linear and
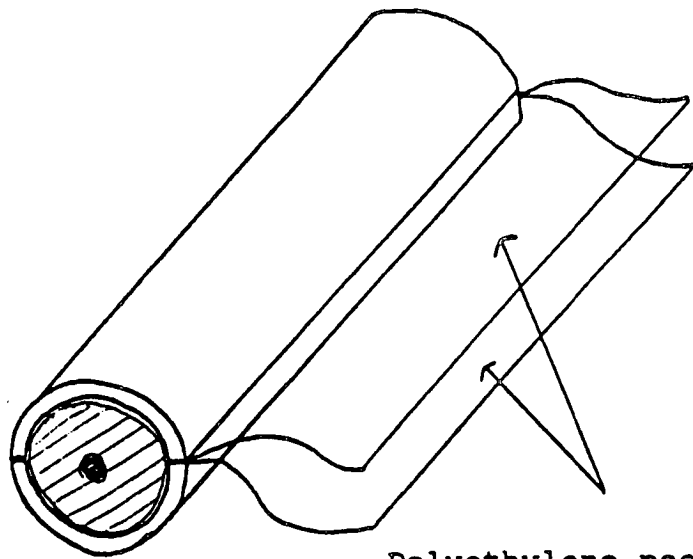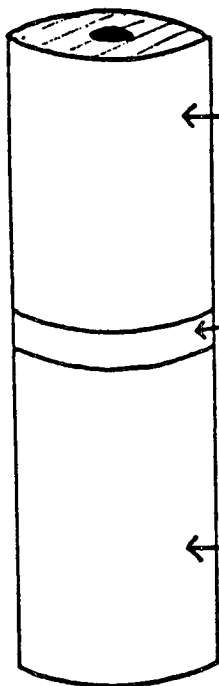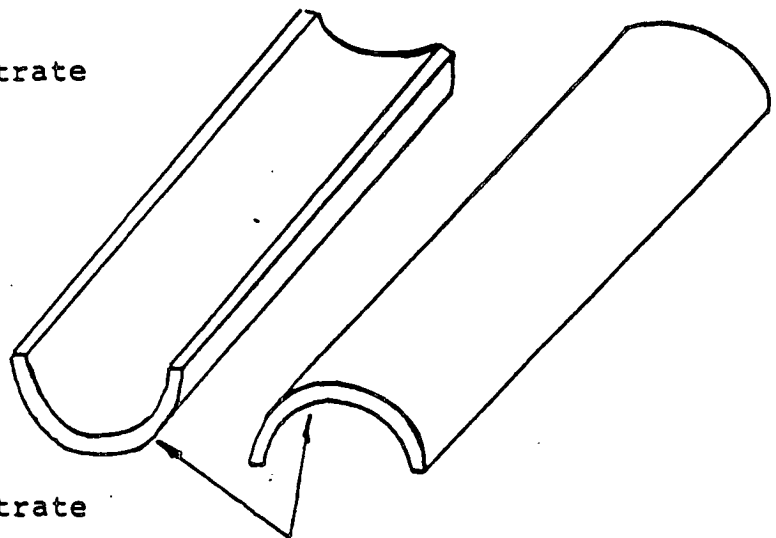
Figure 11-2 Tensile adhesive joint specimen for polystyrene substrate. Polystyrene cylinders are surrounded by a single sheet of release film and are placed in a split tube alignment fixture. Water is injected into gap between two polystyrene cylinders and is allowed to freeze. Before testing, split tube alignment fixture and release film are removed.

Table 11-1 Roughness characteristics for tensile specimen surfaces.

Substrate	Amplitude (μm)	Freq. (cm^{-1})
Steel (polished)	< 1	0
Steel	11	123
Steel	20	77
Steel	29	50
Polystyrene (polished)	< 1	0
Polystyrene	17	129
Polystyrene	27	90
Polystyrene	46	57

nonlinear forms (squares, logarithms, reciprocals, products) in exhaustive linear regression. The best equation for y in terms of x_i was selected using the 95% value of R^2 (squared multiple correlation coefficient) as a criterion. We chose the simplest equation at or above 95% for each material system and loading mode, since we saw no increase in clarity with more complex equations at higher R^2 values.

The tensile test results for ice-polystyrene adhesive joints are summarized in Tables 11-2 and 11-3. Where the polystyrene (PS) substrate was not chilled prior to application of the water, the bond formed was apparently very weak and was usually unable to survive gentle handling (Table 11-2). These specimens failed cleanly at the interface.

We propose an explanation for this apparent poor interface based on the freezing pattern of the water in these specimens. Freezing occurred first at the specimen perimeter and then moved radially inward, with the last water to freeze located in the center of the specimen. Because of the prior solidification at the perimeter, volumetric expansion acompanying freezing of the remaining water was constrained to take place parallel to the specimen axis, pushing the two substrate cylinders apart and weakening or breaking the bond between the ice and polystyrene.

The radial freezing from perimeter to center can be assumed due to the low thermal conductivity of the polystyrene substrate. This assumption was verified when we found that prior chilling of the substrate to the selected conditioning temperature promoted a more simultaneous freezing of the water, and resulted in formation of a stronger adhesive bond. The discovery that the bond strength can be affected by the freezing pattern is very important. It suggests that the natural expansion behavior of freezing water can be used to promote a weak ice adhesion.

The ice-polystyrene joints where the substrate was previously chilled survived handling and were able to be tested. They exhibitedcohesive failures in the ice, adhesive failures (interfacial), and mixed failures where the crack path meandered from interface to ice and back. No particular failure mode was associated with either high or low strength values. Furthermore the crystal size within each specimen was not uniform, each specimen containing a wide range of sizes. These features were shown in Figure 9-6 and were discussed previously in the section on ice crystal characterization.

Data analysis for the set of ice-polystyrene tensile specimens whose substrates were chilled prior to specimen preparation revealed that conditioning temperature was the most important variable. The following equation was determined from the data:

$$y = 195x_1 - 1.8x_4 + (1.3 \times 10^7)/x_1 \qquad \text{at 96.5\% criterion}$$

In this equation, the term with the largest coefficient is the most important and it shows that adhesive joint strength increases with decreasing conditioning temperature. Substrate surface roughness is of minor importance and other variables are so unimportant that they do not appear in the equation.

Table 11-2 Tensile test results for ice on polystyrene, not chilled before application of water.

Condit'g. T, °C	Test T, °C	Test Rate mm/min	Roughness Amplit.,μm	Tensile Strength,MPa*
-10	-20	2.54	27	0.031 ± 0.034
-10	-10	1.02	< 1	0.262 ± 0.536
-10	-40	10.2	46	0.239 ± 0.316
-20	-		46	0
-20	-		< 1	0
-30	-		46	0
-20	-		27	0
-30	-		27	0
-20	-		27	0
-20	-		< 1	0

*Average ± 1 std. dev.

Table 11-3 Tensile test results for ice on polystyrene, chilled to conditioning temperature before application of water.

Condit'g. T, °C	Test T, °C	Test Rate mm/min	Roughness Amplit.,μm	Tensile Strength,MPa*
-10	-10	1.02	< 1	0.063 ± 0.029
-10	-20	2.54	27	0.029 ± 0.021
-10	-40	10.2	46	0.023 ± 0.021
-20	-10	2.54	46	0.031 ± 0.023
-20	-20	10.2	< 1	0.542 ± 0.777
-20	-40	1.02	27	0.074 ± 0.010
-30	-10	10.2	27	2.32 ± 0.325
-30	-20	1.02	46	1.62 ± 1.36
-30	-40	2.54	< 1	2.74 ± 1.74

*Average ± 1 std dev.

The tensile test results for the ice-steel joint are summarized in Table 11-4. In contrast to polystyrene, the high thermal conductivity of the stainless steel substrate led to simultaneous freezing of all the water in the gap, even without prior chilling. The ice layer itself was found to be bubble-free, and all the test specimens failed cohesively in the ice, irrespective of surface roughness.

The ice-steel joint strength showed no dependency on test temperature, test rate, conditioning temperature, or surface roughness, but was found to be related to ice crystal size. Although not a controlled variable in this investigation, crystal size was determined by inspection of the ice on each specimen after tensile testing. The fact that crystal size varied from specimen to specimen but was uniform within a specimen permitted an evaluation of joint strength as a function of crystal size. Figure 9-5 in the section on ice crystal characterization shows the strong inverse relation. We emphasize that this relation pertains to ice strength alone, as the cohesive failures did not test the interface.

Shear Testing

The shear test specimen we developed is shown in Figure 11-3. It was very convenient to assemble, align, and test. The substrates had different levels of machined roughness, similar to those described for the tensile tests. The roughness details are presented in Table 11-5. For shear, the same variables and substrates were used as for tensile tests. Shear test results, however, were not the same.

The shear strength data for ice on polystyrene and steel are shown in Tables 11-6 and 11-7, respectively. Unlike for the tensile tests, substrate surface roughness had a great effect on shear failure mode. All smooth-surfaced specimens failed adhesively while specimens with the machined roughness failed cohesively in the ice. Apparently, the introduction of substrate surface roughness diverts the locus of failure from the interface into the ice.

Careful examination of Tables 11-6 and 11-7 reveals that the shear strength values fell into two groups: low and high, corresponding to adhesive (interfacial) and cohesive failures, respectively. Within each group, the strength values were almost constant, and therefore totally insensitive to any of the independent variables. (Multivariate linear regression cannot be applied with meaning or validity to a joint strength distribution that is two-valued only.) The higher joint strengths found for cohesive failures apparently come from the fact that the shear strength of ice is higher than the shear strength of the ice-substrate interface.

It must be remembered that joint strength tests such as the butt tensile test or shear test carried out for polystyrene and for steel do not yield a materials system parameter. That is, the values obtained from the joint strength tests are determined in part by the bulk properties of the ice and the substrate. Joint strength expressed as load per unit area does not contain the bulk properties explicitly, with the consequence that joint strength is

Table 11-4 Tensile test results for ice on steel.

Condit'g. T, °C	Test T, °C	Test Rate mm/min	Roughness Amplit., μm	Tensile Strength, MPa*
-10	-10	2.54	0	3.61 ± 0.16
			10.9	4.35 ± 0.83
			20.3	5.11 ± 0.72
			28.7	4.06 ± 0.85
-10	-20	1.02	0	3.99 ± 0.41
			10.9	4.96 ± 0.84
			20.3	4.93 ± 0.80
			28.7	4.38 ± 1.23
-10	-20	10.2	0	5.02 ± 1.58
			10.9	5.16 ± 1.41
			20.3	5.99 ± 0.70
			28.7	4.83 ± 1.65
-10	-40	2.54	0	7.09 ± 0.54
			10.9	4.75 ± 1.05
			20.3	6.03 ± 0.79
			28.7	6.25 ± 0.41
-20	-10	1.02	0	4.59 ± 0.58
			10.9	5.53 ± 1.55
			20.3	6.10 ± 0.78
			28.7	6.58 ± 0.96
-20	-10	10.2	0	4.96 ± 1.51
			10.9	5.80 ± 1.79
			20.3	5.98 ± 1.86
			28.7	5.69 ± 1.87
-20	-20	2.54	0	3.03 ± 0.87
			10.9	4.34 ± 1.96
			20.3	2.48 ± 0.17
			28.7	3.45 ± 1.45
-20	-40	1.02	0	2.87 ± 1.01
			10.9	5.16 ± 2.28
			20.3	5.62 ± 1.97
			28.7	5.96 ± 2.30

Table 11-4, continued.

-20	-40	10.2	0	3.84 ± 0.94
			10.9	3.84 ± 1.22
			20.3	2.51 ± 1.12
			28.7	2.84 ± 1.69
-30	-10	2.54	0	3.48 ± 0.67
			10.9	2.96 ± 2.41
			20.3	3.01 ± 0.97
			28.7	4.52 ± 1.69
-30	-20	1.02	0	3.23 ± 8.82
			10.9	3.71 ± 1.37
			20.3	3.49 ± 1.09
			28.7	3.12 ± 1.13
-30	-20	10.2	0	3.73 ± 2.23
			10.9	-
			20.3	3.67 ± 1.49
			28.7	3.78 ± 2.24
-30	-40	2.54	0	2.80 ± 2.23
			10.9	1.95 ± 4.48
			20.3	2.00 ± 5.79
			28.7	2.74 ± 2.02

* Ave. ± 1 std. dev.
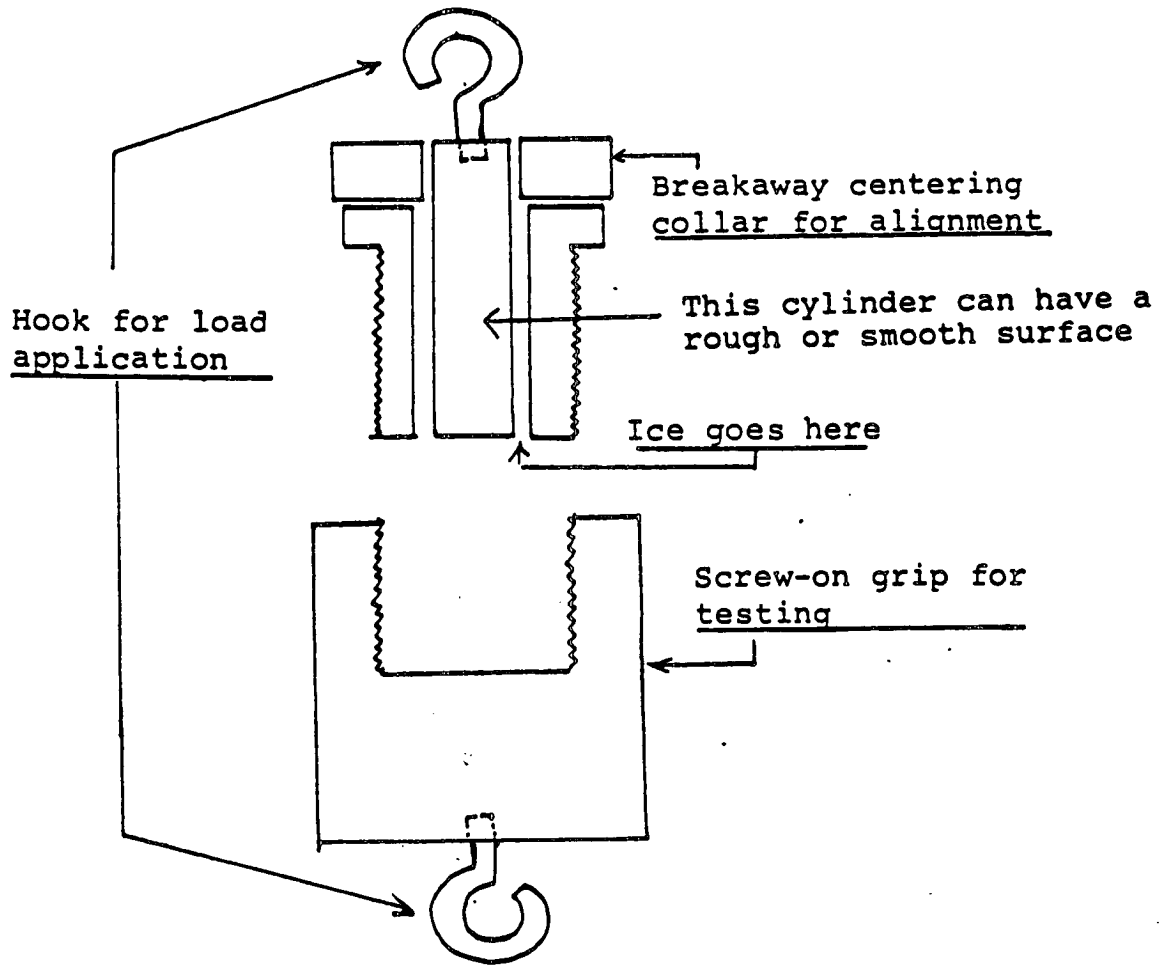
Figure 11-3 Shear Test Specimen. This assembly allows proper centering of the inner cylinder with respect to the outer cylinder. Screw-on grip and screw-in hooks enable experimenter to prepare for testing without undue disruption of the test specimen.

Table 11-5 Roughness characteristics for shear specimen surfaces.

Substrate	Amplitude (μm)	Freq. (cm^{-1})
Steel (polished)	< 1	0
Steel	13	153
Steel	35	76
Polystyrene (polished)	< 1	0
Polystyrene	22	153
Polystyrene	40	76

Table 11-6 Shear test results for ice on polystyrene (both water and PS at room temperature upon initial contact).

Condit'g. T, °C	Test T, °C	Test Rate mm/min	Roughness Amplit.,μm	Shear Strength,MPa[*]
-10	-10	1.02	< 1	0.680 ± 0.286 (a)
-10	-20	2.54	22	4.13 ± 0.567 (c)
-10	-30	10.2	40	3.86 ± 0.681 (c)
-20	-10	2.54	40	3.86 ± 0.397 (c)
-20	-20	10.2	< 1	0.516 ± 0.124 (a)
-20	-30	1.02	22	4.18 ± 0.571 (c)
-30	-10	10.2	22	3.25 ± 0.582 (c)
-30	-20	1.02	40	3.99 ± 0.762 (c)
-30	-30	2.54	< 1	1.03 ± 0.453 (a)

[*]Average ± 1 std. dev.
(a) All specimens in sample failed at interface.
(c) All specimens in sample failed cohesively within ice.

Table 11-7 Shear test results for ice on steel (both steel and water at room temperature upon initial contact).

Condit'g. T, °C	Test T, °C	Test Rate mm/min	Roughness Amplit.,μm	Shear Strength,MPa*
-10	-10	1.02	< 1	1.27 ± 0.086 (a)
-10	-20	2.54	13	4.73 ± 0.476 (c)
-10	-30	10.2	35	4.45 ± 0.075 (c)
-20	-10	2.54	35	4.88 ± 0.724 (c)
-20	-20	10.2	< 1	1.36 ± 0.315 (a)
-20	-30	1.02	13	5.40 ± 0.232 (c)
-30	-10	10.2	13	4.17 ± 0.302 (c)
-30	-20	1.02	35	4.77 ± 0.629 (c)
-30	-30	2.54	< 1	1.56 ± 0.212 (a)

*Average ± 1 std. dev.
(a) All specimens in sample failed at interface.
(c) All specimens in sample failed cohesively within ice.

not a property inherent to the interface between the two materials being considered. A joint strength test such as that used here is for comparing preparation and test conditions within a given bimaterials system. While it is tempting to compare the joint strength values of the ice-polystyrene system to those of the ice-steel system, this is not the proper comparison to make and no insight is gained by making it.

Summary of Joint Strength Findings

The important findings from the strength tests described in this section are summarized below.

1. A residence time (or conditioning time) at low temperature
   is required for joint strength to develop.
2. Some substrates nucleate uniform-sized ice crystals, while
   others nucleate crystals having a broad distribution of
   sizes.
3. Substrate surface roughness appears to have no systematic
   effect on ice crystal size.
4. Ice crystal size, which was not one of the controlled
   variables used in this study, is germane to joint strength
   only when failure occurs within the ice.
5. The thermal conductivity of the substrate influences the
   freezing pattern of water in a gap.
6. Certain freezing patterns can generate sufficient internal
   stress to break the ice-substrate bond.

In practical terms, the first finding suggests that ice removal attempts conducted immediately after freezing would be more successful than those conducted several hours later, when bond strength has developed under low temperature conditioning. Furthermore, the last two findings, pertaining to freezing pattern, suggest a means to control or reduce ice-pavement bonding. Attempts to generate internal stress during the freezing process itself should be made; this could be done by manipulating the pavement's thermal conductivity. The remaining findings are interesting but have no practical implications.

12

Conclusions and Recommendations

Studies of ice on the pavement substrates are complicated by uncontrollable and unidentifiable variables, making it difficult to interpret experimental results in a way that lends understanding to the phenomenon of ice adhesion. However, studies on model and reference substrates in addition to those on pavement provided insight into ice bonding behavior.

The important conclusions reached in this work are reiterated below, along with recommendations on how some of the findings can be exploited for control of ice on pavement.

One important finding was that a layer of small, bubble-free ice crystals nucleates on the pavement surface once it goes just below 0°C, regardless of the conditions in the bulk water and atmosphere above. This layer, strong and well-adhered, is difficult to remove because of preferential failure of the flaw-filled ice beyond. Obviously, if early nucleation at the pavement surface could be prevented, the ice directly contacting the pavement would probably be weaker and less well-adhered due to entrapped bubbles or larger crystallite size as found in the bulk ice. We briefly investigated the nucleation prevention idea by mixing small amounts of salt into the concrete itself. It seemed to make ice removal easier, but we did not have time to expand upon the idea.

Our evaluation of the consequences of the well-known expansion of ice near the freezing point led to discovery of considerable pressure build-up in trapped water, not yet frozen. In pavement, with its network of interconnected fissures, this pressure is relieved by the migration of the pressurized water farther into the pavement itself. However, trapped water that is prevented from migrating can experience pressures high enough to be exploited. Experiments on flat slabs of transparent substrate material with pores drilled into its surface showed that trapped water, when it finally freezes, builds up enough pressure to spontaneously debond the whole body of ice as a unit from the substrate. This was adapted to pavement by embedding small plastic cups into the surface to serve as impermeable pores. This worked quite well; the ice within and immediately around the pores debonded from the pavement. However there were areas of pavement surface between pores where ice remained adhered.

Related to this was the finding that thermal properties of the substrate influence the freezing pattern. A thermal insulator results in slow-to-freeze regions on a surface, which can become trapped water regions. When these regions finally freeze, they exert so much internal pressure that the whole ice-substrate bond fails with very low applied load. This suggests the construction of pavement containing slabs of material having poor conductivity (e.g. polyethylene).

Another key finding was that the work of adhesion between water and substrate, a quantity related to substrate surface energy, is not linearly related to the fracture energy of the ice-substrate bond. The fracture energy (i.e., the work to separate the ice-substrate interface) follows a power law. Thus, for all but the lowest energy surfaces, the adhesion is inherently very high, and separation of ice from the substrate requires increasingly more energy. Unfortunately portland cement concrete and aged asphalt concrete are relatively high energy materials, making ice removal an inherently energy-consuming process.

The obvious recommendation to coat the pavement surface with a fluorocarbon or with a completely unoxidized hydrocarbon, is not a practical one for existing pavement. However, low energy materials could be incorporated into novel highway surface designs in the far future.

Another finding was that, for attempted removal of ice by applied shear load, even a minimal substrate surface roughness acts to divert the crack locus from the ice-substrate interface into the ice itself, leaving a layer of ice on the substrate. This merely points out how inherently difficult it is for traditional mechanical methods to remove ice completely from rough pavement.

Finally, local heating of the ice-substrate interface (without heating the bulk ice) coupled with an extremely small shear load easily debonds ice, even from a rough substrate. If an economical means to heat only the interface to near the melting temperature, ice could be removed mechanically with very little effort.

References

1. J.S. Gadzuk, "Interactions of Atoms and Molecules with Surfaces," in Surface Physics of Materials, vol. 2, J.M. Blakely, Ed., Academic Press, New York, 1975, p. 339.

2. W. Moore, Physical Chemistry, Prentice-Hall, Englewood Cliffs, New Jersey, 1966, pp. 713-718.

3. F.M. Fowkes, "Attractive Forces at Interfaces," Ind. Eng. Chem., 56, 40-52 (1964).

4. A.S. Myerson, "Impurity Capture During Crystal Growth," Ph.D. Dissertation, University of Virginia, Charlottesville, 1977.

5. A.S. Myerson and D.J. Kirwan, "Impurity Capture During Crystal Growth: Part I, Computer Simulation," Ind. Eng. Chem. Fundam., 16, 414-419 (1977).

6. A.S. Myerson and D.J. Kirwan, "Impurity Capture During Crystal Growth: Part II, Correlation of Experimental Data," Ind. Eng. Chem. Fundam., 16, 420-425 (1977).

7. J.R. Dyer, Applications of Absorption Spectroscopy of Organic Compounds, Prentice Hall, Englewood Cliffs, NJ, 1965, pp. 33-38.

8. B.W. Cherry, Polymer Surfaces, Cambridge University Press, Cambridge, 1981, pp. 68-94.

9. B. Miller, L.S. Penn, and S. Hedvat, "Wetting Force Measurements on Single Fibers," Colloids and Surfaces, 6, 49-61 (1983).

10. D.K. Owens and R.C. Wendt, "Estimation of the Surface Free Energy of Polymers," J. Appl. Polym. Sci., 13, 1741-1747 (1969).

11. L.S. Penn, F.A. Bystry, and H.J. Marchionni, "Relation of Interfacial Adhesion in Kevlar/Epoxy Systems to Surface Characterization and Composite Performance," Polym. Compos., 4, 26-31 (1983).

12. D.H. Kaelble, "Dispersion-Polar Surface Tension Properties of Organic Solids," J. Adhesion., 2, 66-81 (1970).

13. C.D. Wagner et al., Handbook of X-Ray Photoelectron Spectroscopy, Perkin-Elmer Corporation, Norwalk, Connecticut, 1979.

14. Charles E. Knox, "Fiberglass Reinforcement," in Handbook of Composites, George Lubin, Editor, Van Nostrand Rineholt, New York, 1982, pp. 136-159.

15. J.J. Mecholsky, and D.E. Passoja, "Fractals and Brittle Fracture," in Fractal Aspects of Materials, R.B. Laibowitz, B.B. Mandelbrot, and D.E. Passoja, Eds., Proceedings of the Materials Research Society, Pittsburgh, Pennsylvania, 1985, pp. 117-119.

16. J.J. Mecholsky, T.J. Mackin, and D.E. Passoja, "Self-Similar Crack Propagation in Brittle Materials," in Advances in Ceramics, vol. 22: Fractography of Glasses and Ceramics, American Ceramic Society, 1988, pp. 127-134.

17. S.A. Bari and J. Hallett, "Nucleation and Growth of Bubbles at an Ice-Water Interface," J. Glaciology, 13, 489-512 (1974).

18. A.E. Carte, "Air Bubbles in Ice," Proc. Phys. Soc., 73, 757-768 (1960).

19. D.M. Cole, "Preparation of Polycrystalline Ice Specimens for Laboratory Experiments," Cold Regions Science and Technology 1, 153-159 (1977).

20. E.H. Andrews and A.J. Kinloch, "Mechanics of Adhesives I," Proc. Royal Soc. London, A332, 385-399 (1973).